

PREDICTION OF THE AERO-ELASTIC FORCE
IN A LABYRINTH TYPE SEAL
AND ITS IMPACT ON TURBOMACHINERY
STABILITY

by
Bruce E. Gans

Submitted in Partial Fulfillment
of the Requirements for the
Degree of
Mechanical Engineer
at the
Massachusetts Institute of Technology

January 13, 1983

The author hereby grants M.I.T. permission to reproduce and to distribute
copies of this thesis document in whole or in part.

Signature of Author


Department of Mechanical Engineering
January 13, 1983

Certified by


Thesis Supervisor

Accepted by


Chairman, Departmental Graduate Committee

Archives

MASSACHUSETTS INSTITUTE
OF TECHNOLOGY

APR 20 1983

LIBRARIES

PREDICTION OF THE AERO-ELASTIC FORCE IN A
LABYRINTH TYPE SEAL AND ITS IMPACT ON
TURBOMACHINERY STABILITY

by

BRUCE EDWARD GANS

Submitted to the Department of Mechanical Engineering
on January 13, 1983 in partial fulfillment of the
requirements for the Degree of Mechanical Engineer.

ABSTRACT

Load dependent rotor dynamic instabilities have caused vibration in turbomachinery at a frequency corresponding to the first flexural mode. A potential source of a destabilizing force is the labyrinth seal. To evaluate the effect on rotor stability, the stiffness and damping coefficients are derived for arbitrary seal geometry and leakage flow conditions using a one-dimensional flow model.

Displacement related forces are calculated for several configurations and compared to actual test measurements. Excellent agreement for the cross-coupling stiffness was obtained for both half and full labyrinth seal designs.

In order to better understand the effect of various seal parameters, closed form expressions approximating the stiffness and damping coefficients are obtained for a single chamber seal and a long, multichamber seal. Both the closed form expressions and the complete theory are used to demonstrate how geometric factors influence the magnitude and direction of the out-of-phase force and are used to give physical insight to the destabilizing mechanism. Seal forces can increase the stability of a rotor system as well as decrease it.

Several examples are given to demonstrate how variation in operation can affect the magnitude of destabilizing seal forces. With changes to the seal geometry, the stable region for operation can be increased.

Thesis Supervisor: S. H. Crandall

Title: Professor of Mechanical Engineering

ACKNOWLEDGEMENTS

The author would like to pay tribute to the following:

The General Electric Company, whose financial backing made graduate study at M.I.T. possible.

Bill Caruso, who provided helpful comments on the content and organization of this document.

Professor S. H. Crandall, who made my years at M.I.T. very rewarding.

My wife, Shelley, who provided the encouragement needed to finish this phase of my education.

TABLE OF CONTENTS

	<u>PAGE</u>
ABSTRACT	ii
ACKNOWLEDGEMENTS	iii
LIST OF ILLUSTRATIONS	v
LIST OF TABLES	viii
NOMENCLATURE	ix
I. INTRODUCTION	1
II. DERIVATION OF SEAL FORCE EQUATIONS	8
2.1 Seal Model	8
2.2 Conservation of Mass	12
2.3 Conservation of Momentum	13
2.4 Thermodynamic Considerations	15
2.5 Fluid Mechanic Considerations	19
2.6 Steady-State Requirements	25
2.7 Dynamic Requirements	28
III. AERO-ELASTIC FORCES	38
3.1 Stiffness and Damping Coefficients	38
3.2 Comparison with Test Results	43
3.3 Influence of Seal Geometry, Preswirl and Rotor Angular Velocity	58
3.4 Closed Form Expressions	74
IV. IMPACT ON TURBOMACHINERY DESIGN AND OPERATION ON STABILITY	95
4.1 Operation at Variable Design Conditions	98
4.2 Stability Contour Mapping	106
V. CONCLUSIONS	122
VI. REFERENCES	124
VII. APPENDIX	126
Determination of Chamber Pressure Variation	

LIST OF ILLUSTRATIONS

<u>FIGURE</u>		<u>PAGE</u>
1.	Common types of labyrinth seals used in turbomachinery.	2
2.	Schematic representation of velocity distributions and flow patterns in a straight labyrinth seal.	9
3.	Dynamic orbit of the rotor center in a seal.	11
4.	Geometry and fluid properties for conservation of mass control volume of the ith seal chamber.	14
5.	Control volume for conservation of momentum in tangential direction.	16
6.	Enthalpy - entropy chart for fluid passing through a labyrinth seal.	18
7.	Friction factor chart for fully developed laminar and turbulent flow through rough pipes.	22
8.	Average friction factor for developing flow in pipes.	26
9.	Geometry and flow conditions for Benckert and Wachter three chamber test seal.	46
10.	Comparison of predicted and calculated pressure distributions in each chamber for Figure 9. Predicted values are based on identical flow coefficients for each strip. Preswirl value - 367 ft/sec.	48
11.	Comparison of predicted and calculated pressure distributions for Figure 9 with optimized seal strip flow coefficients. Preswirl value - 367 ft/sec.	53
12.	Comparison of predicted and calculated pressure distributions with optimized flow coefficients and zero preswirl.	54
13.	Calculated tangential velocity distribution for Figure 11.	57
14.	Comparison of calculated cross-coupling force gradients with Benckert and Wachter measurements on straight labyrinths.	59
15.	Comparison of calculated cross-coupling force gradients with Benckert and Wachter measurements on full labyrinths.	60
16.	Comparison of calculated cross-coupling stiffness using the Benckert and Wachter method and using equations (46) and (49).	62

LIST OF ILLUSTRATIONS (Continued)

<u>FIGURE</u>		<u>PAGE</u>
17.	Displacement and whirl force gradients as a function of speed for Figure 16. Thirty chamber seal with preswirl equal to 80% of the rotor surface velocity.	67
18.	Displacement and whirl force gradients as a function of speed for Figure 16. Thirty chamber seal with preswirl equal to 36% of the rotor surface velocity.	68
19.	Displacement and whirl force gradients as a function of speed for Figure 16. Thirty seal with no preswirl.	69
20.	Displacement and whirl force gradients as a function of speed for Figure 16. Three chamber seal with preswirl equal to 80% of the rotor surface velocity.	70
21.	Displacement and whirl force gradients as a function of speed for Figure 16. Three chamber seal with preswirl equal to 36% of the rotor surface velocity.	71
22.	Displacement and whirl force gradients as a function of speed for Figure 16. Three chamber seal with no preswirl.	72
23.	Schematic of pressure and velocity distribution for a very long, multichamber seal.	78
24.	Demonstration of destabilizing force with rotating damping model.	84
25.	Configuration for single chamber seal with shaft whirl.	86
26.	Pressure and leakage flow variation for a single chamber seal.	87
27.	Tangential velocity distribution in a single chamber seal.	89
28.	Steam path and first stage steam admission for high speed compressor drive turbine.	99
29.	Steam flow and first stage shell pressure for compressor drive turbine.	101
30.	Schematic diagram of steam velocities entering and leaving turbine blade.	102
31.	Velocity diagrams of steam flow for 3rd and 5th valve points.	104

LIST OF ILLUSTRATIONS (Continued)

<u>FIGURE</u>		<u>PAGE</u>
32.	Modeling of leakage flow path for determination of seal preswirl value.	105
33.	Comparison of destabilizing force gradient for stage (2) seal. Preswirls from equation (92) and one-half of the rotor surface velocity.	108
34.	Single stage rotor model with two labyrinth seals.	111
35.	Damped critical speeds and mode shapes below 12,000 RPM for Figure 34. Rotor speed 9000 RPM.	112
36.	Log decrement for single stage rotor model without seal forces.	113
37.	Dimensionless bearing coefficients versus Sommerfeld number for plain cylindrical bearing.	114
38.	Stability contour map for single stage rotor with original seal design.	117
39.	Stability contour map for single stage rotor with deep chamber, reduced clearance design.	120
40.	Comparison of leakage flow rates for original and reduced clearance seal designs.	121
A.1	Matrix formation of equations (A.1) and (A.2) for solution of a four strip labyrinth.	128

LIST OF TABLES

<u>TABLE</u>		<u>PAGE</u>
1.	COMPARISON OF CALCULATED AND MEASURED FORCES FOR FIGURE 9	49
2.	DISTRIBUTION OF FLOW COEFFICIENTS FOR FIGURES 10, 11 AND 12	51
3.	COMPARISON OF CALCULATED AND MEASURED FORCES FOR FIGURES 11 AND 12	55
4.	INFLUENCE OF GEOMETRIC CHANGES ON K_{12} AND C_{11} FOR A THIRTY CHAMBER HALF LABYRINTH	64
5.	INFLUENCE OF GEOMETRIC CHANGES ON K_{12} AND C_{11} FOR A THREE CHAMBER HALF LABYRINTH	66
6.	EFFECT OF ROTOR SPEED AND INLET SWIRL VELOCITY ON HALF LABYRINTHS	73
7.	CONVERGING AND DIVERGING SEAL COEFFICIENTS FOR A THIRTY CHAMBER HALF LABYRINTH	75
8.	CONVERGING AND DIVERGING SEAL COEFFICIENTS FOR A THREE CHAMBER HALF LABYRINTH	76
9.	TANGENTIAL VELOCITY DISTRIBUTIONS FOR DIFFERENT VALVE POINTS	107
10.	FIRST CRITICAL LOG DECREMENT FOR ROTOR WITH ORIGINAL SEAL AND WITH DEEP CHAMBER SEALS	116

NOMENCLATURE

<u>SYMBOL</u>	<u>UNITS</u>	<u>DEFINITION</u>
C_{ij}	lbf-sec/in	Equivalent seal damping coefficient
c	ft/sec	Fluid average tangential velocity
C_D	dimensionless	Overall flow coefficient for a multi-tooth seal
C_B	ft/sec	Tangential velocity component of gas leaving turbine blade
cm	ft/sec	Zero-to-peak chamber tangential velocity variation
e	in	Rotor eccentricity
F	lbf	Force on rotor from seal
f	in ²	Chamber area
h	in	Chamber height
i	dimensionless	Chamber or seal strip number
j	dimensionless	$\sqrt{-1}$
K_{ij}	lbf/in	Equivalent seal stiffness coefficient
k_s	in	Equivalent surface roughness
L	in	Average distance travelled in tangential direction by fluid in chamber
l	in	Distance between adjacent seal strips
M	dimensionless	Total number of seal chambers
N	dimensionless	Total number of seal strips
P	lbf/in ²	Pressure
P_m	lbf/in ²	Zero-to-peak chamber pressure variation
Q	lbm/sec	Total leakage flow rate
q	lbm/sec-in	Leakage flow rate per unit circumferential length
R	in	Radius to seal

NOMENCLATURE (Continued)

<u>SYMBOL</u>	<u>UNITS</u>	<u>DEFINITION</u>
r	in	Circular position of rotor center in seal
r _i	in	Radial location between stationary and rotating surfaces
Re	dimensionless	Reynolds number
R _h	in	Hydraulic radius
r _o	in	Magnitude of circular orbit of rotor center
RT	lbf-in/lbm	Product of fluid gas constant and absolute temperature of fluid
S _j	in	Wetted perimeter of surface j
S	dimensionless	Sommerfeld number
t	sec	Time
u	ft/sec	Rotor surface velocity
V	ft/sec	Velocity
V _{ax}	ft/sec	Average axial velocity of fluid in chamber
W	lbf	Journal static loading
x	in	Circumferential location in seal

<u>GREEK LETTER</u>	<u>UNITS</u>	<u>DEFINITION</u>
α_B	rad	Blade exit angle
α_N	rad	Nozzle exit angle
γ	dimensionless	Specific heat ratio
δ	in	Radial clearance between seal strip and rotor
ϵ	dimensionless	Ratio of rotor eccentricity to radial clearance
θ	rad	Angular location
λ	dimensionless	Friction factor
μ	dimensionless	Flow coefficient for single seal strip
ν	in ² /sec	Kinematic viscosity of fluid
ζ	dimensionless	Change in effective clearance from variation in flow coefficients
ρ	lbm/in ³	Fluid density
τ	lbf/in ²	Surface shear stress
ϕ	rad	Phase angle
Ω	rad/sec	Rotor spin angular velocity
ω	rad/sec	Rotor whirl angular velocity

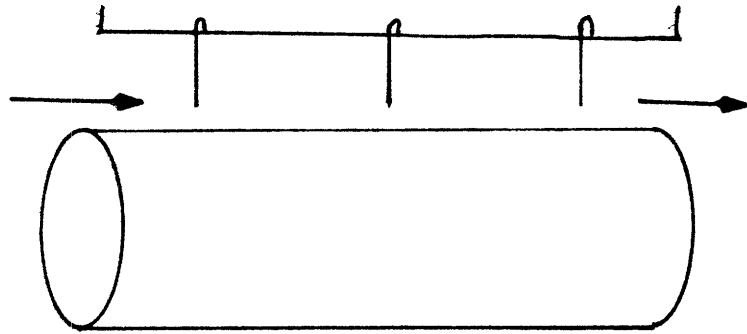
<u>SUBSCRIPT</u>	<u>IMPLICATION</u>
a	Exit value
B	Backward traveling wave
c	Tangential velocity
eq	Equilibrium value
F	Forward traveling wave
i	Chamber or tooth number
m	Maximum value
o	Entrance value
R	Rotating component
S	Stationary component
<u>X</u>	Horizontal direction
<u>Y</u>	Vertical direction
1	Horizontal component
2	Vertical component

I. INTRODUCTION

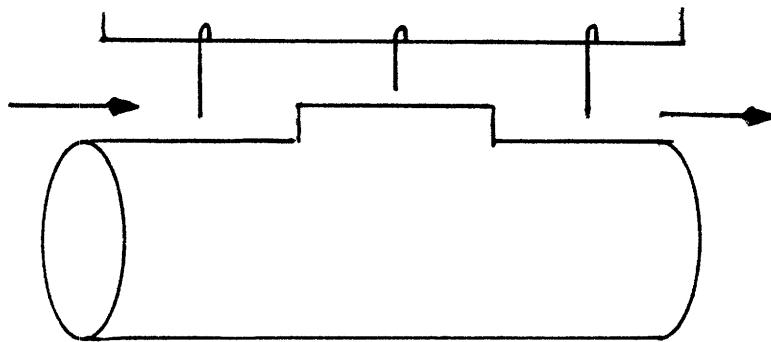
Both turbines and compressors are judged on their ability to operate efficiently and reliably. With today's trend toward higher power density machines, internal leakage control is crucial for minimizing losses and thereby maintaining overall efficiency. A common element used to control leakage is the non-contacting labyrinth seal. This element (Figure 1) is a series of throttling points or orifices which control the leakage flow rate by the radial tooth clearance, seal chamber geometry and the number of sealing strips present. The selection of a particular type of labyrinth from those shown in Figure 1 is made by considering the required axial thermal growth capability and operating pressures as well as leakage control effectiveness. H. Martin⁽¹⁾ described the governing equation predicting the leakage flow rate in terms of the thermodynamic state of the gas and the seal geometry. More recent studies were made by G. Vermes⁽²⁾ and C.A. Meyer⁽³⁾ to determine how the seal strip configuration influences the overall flow coefficient used in Martin's formula. This combined theoretical and empirical effort has resulted in an accurate prediction of leakage losses with labyrinth seals.

In 1965, J.S. Alford⁽⁴⁾ published the first paper on a negative aspect of labyrinth seals. He observed self-excited forward whirl in aircraft engines and concluded that destabilizing forces were generated by circumferential pressure variations in the seal chambers. He noted that the onset of the self-excited whirl occurred at high

STRAIGHT OR HALF LABYRINTH



HIGH - LOW LABYRINTH



FULL LABYRINTH

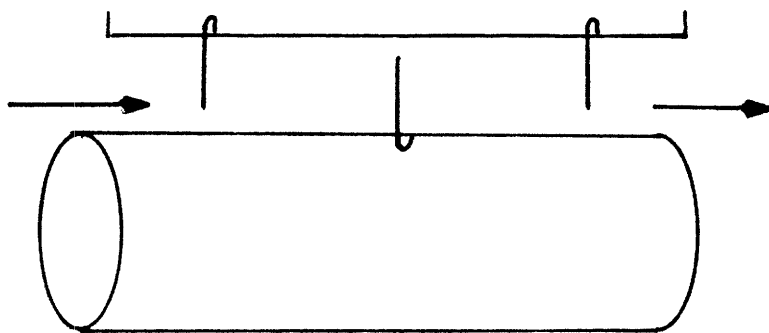


FIGURE 1 Common types of labyrinth seals used in turbomachinery.

pressure and power levels and the mode excited was the fundamental flexural frequency of the rotor system. His analysis to predict the magnitude of the destabilizing seal forces required an axially varying seal strip clearance. A seal with uniform tooth clearance produced no destabilizing forces. A converging seal produced destabilizing forces in the positive whirl direction, while a diverging clearance seal would induce negative whirl. This initial analysis influenced subsequent work by Ehrich⁽⁵⁾, Vance and Murphy⁽⁶⁾. Arguments were given to demonstrate the existence of axially varying clearances in machines with self excited whirl either by design, non-uniform thermal growth or uneven wearing of seal strips. The effects of shaft rotation, surface friction and preswirl of the gas entering the seal were neglected in the above papers.

Improvements on the Alford's theoretical model for predicting the magnitude of the seal forces were published by A. Kostyuk⁽⁷⁾ in 1972 and T. Iwatsubo⁽⁸⁾ in 1980. Kostyuk added significant refinements which included the effects of fluid preswirl, shaft rotation and surface friction into the analysis. His work fell short by predicting no destabilizing force for the uniform clearance seal with parallel displacement of the rotor shaft. His erroneous assumption of constant chamber area circumferentially around the eccentric rotor was partially corrected by T. Iwatsubo. Iwatsubo also allowed the shaft to whirl in the seal in an elliptical orbit. With these refinements, destabilizing forces were now calculated for the uniform clearance seal with parallel rotor displacement.

Concurrently in this period, actual force measurements were being made on labyrinth seal models for various geometries and inlet conditions. The most noteworthy investigations were those conducted by D.V. Wright⁽²¹⁾ and Benckert and Wachter⁽¹¹⁾⁽¹²⁾. Wright's tests, published in 1978, were made on a single chamber seal in which a rotor was rotating and whirling eccentrically. His investigation included uniform, converging and diverging clearance seals. The measurements indicated that negative whirl was induced by the seal in all three cases. This result seemed to contradict actual field observations of positive whirl induced by seal forces as well as the test results of Benckert and Wachter.

A more extensive test program was undertaken by Benckert and Wachter. While their published tests were restricted to constant clearance seals and non-whirling shafts, the measurements made agree with observed whirl in the field. From the measurements made on different geometries, empirical factors were derived which enabled the out-of-phase force to be predicted. In addition to seal geometry, the out-of-phase force was found to be a function of the pre-swirl velocity entering the seal, rotor speed, pressure and density of the gas in the seal. These effects were predicted by the theoretical seal models.

While the work in the area has been extensive, a number of questions remain. These questions are:

1. What are the required geometric, fluid mechanic, and thermodynamic parameters for prediction of labyrinth forces?
2. How well do comprehensive, theoretical calculations agree with test measurements?
3. How should seals be designed to minimize destabilizing forces and also minimize any negative impact on efficiency?
4. How are the labyrinth forces related to the rotor spin and whirl angular velocities?
5. How significant are the seal destabilizing forces relative to other stabilizing forces present in turbomachinery?

Many of these areas have been addressed by different investigators with the conclusions drawn by some in conflict with others. One example would be the effect of radial clearance on the magnitude of labyrinth forces. Theoretical results from R. Jenney⁽¹³⁾ show a weak relationship between clearance and the cross-coupling force, while Iwatsubo predicts a strong inverse relationship between clearance and force. Answers to these questions are key to efficient and reliable operation of turbomachinery.

To resolve these discrepancies, the theoretical models used to calculate seal forces will be re-examined. All currently known effects will be included in the relationships governing leakage flow and the

momentum change of leakage flow to arrive at a more accurate seal force prediction method. The general relationships will then be simplified into two types of seals: a single chamber seal with two sealing strips and a very long multichambered seal. These expressions will reveal the important parameters which govern the cross-coupling force. The mechanism which generates the destabilizing characteristic of very long seals will be explained with S. H. Crandall's⁽⁹⁾⁽¹⁰⁾ heuristic rotating wave model. These functional relationships will be compared to the more complete theory to demonstrate their inadequacies. Force gradients predicted by the complete theory will be compared to actual test measurements for different types of seals to demonstrate the current state-of-art for seal force prediction.

True assessment of the destabilizing forces from seals on rotor stability can only be accomplished by combining the seal forces for a specific rotor system. This has been theoretically investigated on an elementary basis by R. Jenny⁽¹³⁾. In his analysis only the cross-coupling stiffness coefficient was used and was applied at the rotor midspan location. The change in the system's logarithmic decrement for the rotor's first critical was plotted as a function of seal cross-coupling stiffness. This analysis, which neglected the influence of seal location, seal damping and direct stiffness, and variable speed operation did demonstrate that seal forces can significantly reduce turbomachinery stability. As will be shown, the influence of both rotor speed and whirl related forces are also critical in establishing how stably a machine will operate. A high

speed, high power density turbine will be examined to demonstrate these effects. The results are presented in the form of stability contour maps where the logarithmic decrement is plotted as a function of both speed and seal pressure. Since seal pressure is directly related to machine output, the contour can be extended to relate log decrement to speed and machine load. This new approach to judging a rotor system's stability margin allows one to immediately know which combinations of speed and pressure should be avoided. Changes in seal geometry are then made to reshape the stability contour map to achieve a higher operating pressure condition. At the same time the overall efficiency will be improved by changing the seal design to reduce seal leakage. This procedure is easily extended to more complex designs. The design engineer can more effectively evaluate the design of various components to achieve both an efficient machine as well as one that operates reliably.

II. DERIVATION OF SEAL FORCE EQUATIONS

2.1 Seal Model

Early investigators, such as Alford, regarded the steady-state leakage flow through a seal as one-dimensional. As both experimental and theoretical work continued in this area, it became apparent that the flow was quite complex. In general, the flow through the seal is both turbulent and three-dimensional. The pressure distribution in a seal's chamber is non-uniform in both the circumferential and radial directions. Regions of high localized velocity exist adjacent to the shaft. Figure 2 depicts the velocity of distributions which dominate the flow pattern in a typical straight labyrinth seal. In the axial direction, there are two distinct velocity regions. One near the rotor has a high velocity. This induces a vortex in the low velocity region bracketed by the stationary seal teeth. In the circumferential direction there is a turbulent, flat velocity distribution. The channel has three sides stationary and the fourth moving at a velocity, u . With both velocity distributions coexisting, an infinitesimal fluid element might take a three-dimensional spiral path while passing through a chamber. This type of spiral flow pattern was observed experimentally by Iwatsubo⁽⁸⁾ with water as the fluid passing through a straight labyrinth.

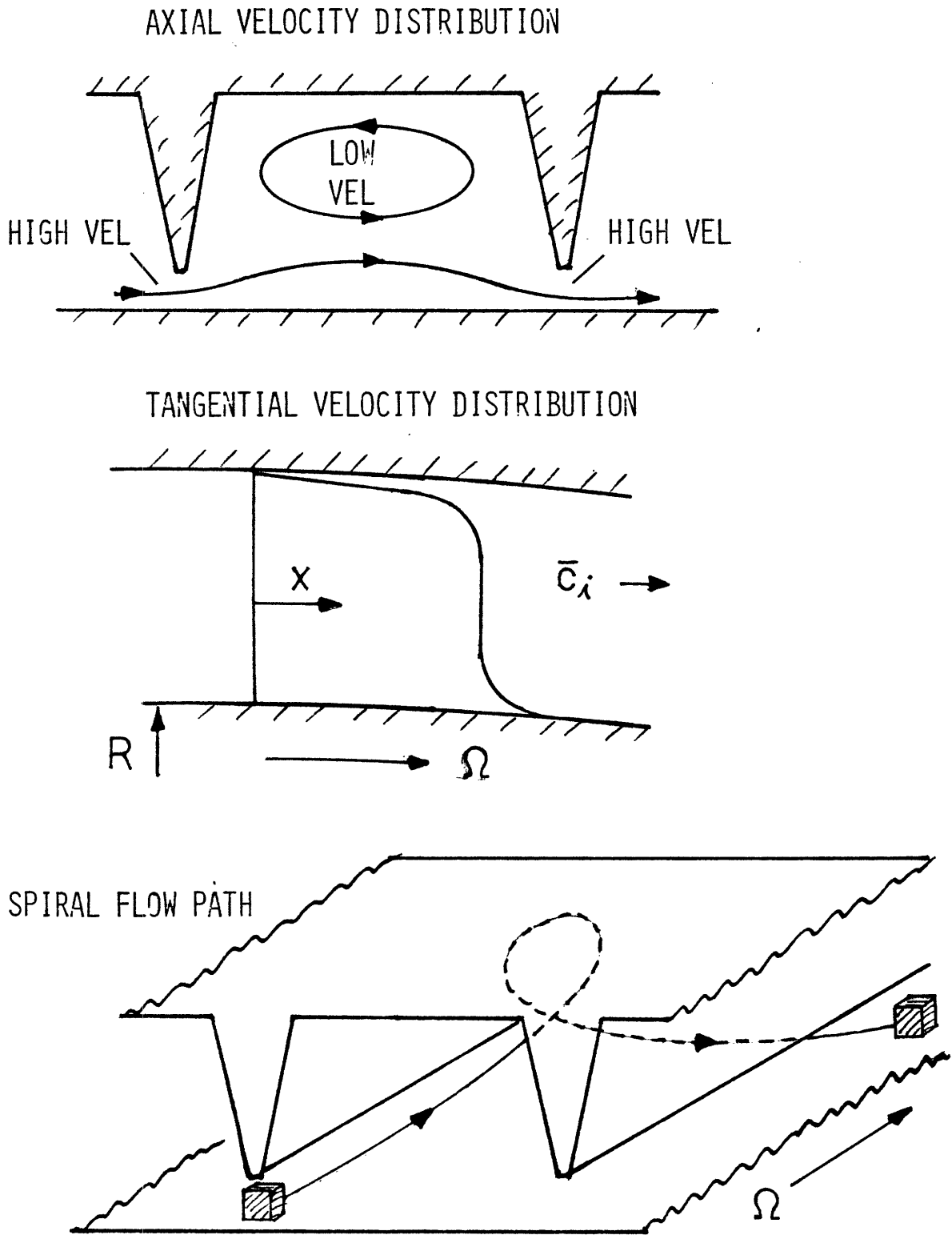


FIGURE 2 Schematic representation of velocity distributions and flow patterns in a straight labyrinth seal.

Around its steady state position, the rotor center precesses with an arbitrary orbit. (See Figure 3). The general direction of the orbit may be either forward or backward whirl and may be of any size. For very large orbits, the distribution of both mean pressure and velocity will vary in a highly non-linear fashion. The net effect of shaft motion is to induce a circumferential pressure variation which results in both an in-phase and out-of-phase force on the rotor. Quite simply, the in-phase force tends to change the natural frequency of the system but the out-of-phase force influences the stability of the rotor system.

To analytically determine the impact of seal forces on turbomachinery stability, this complex flow pattern must be simplified. Analysis of three-dimensional flow problems is generally beyond the scope of practical analytical techniques. The following simplifying assumptions are made:

1. Only circumferential changes in pressure and velocity are considered.
2. The pressure in each chamber is uniform radially and axially and obeys Martin's flow formula.
3. The tangential velocity distribution is uniform across each chamber.

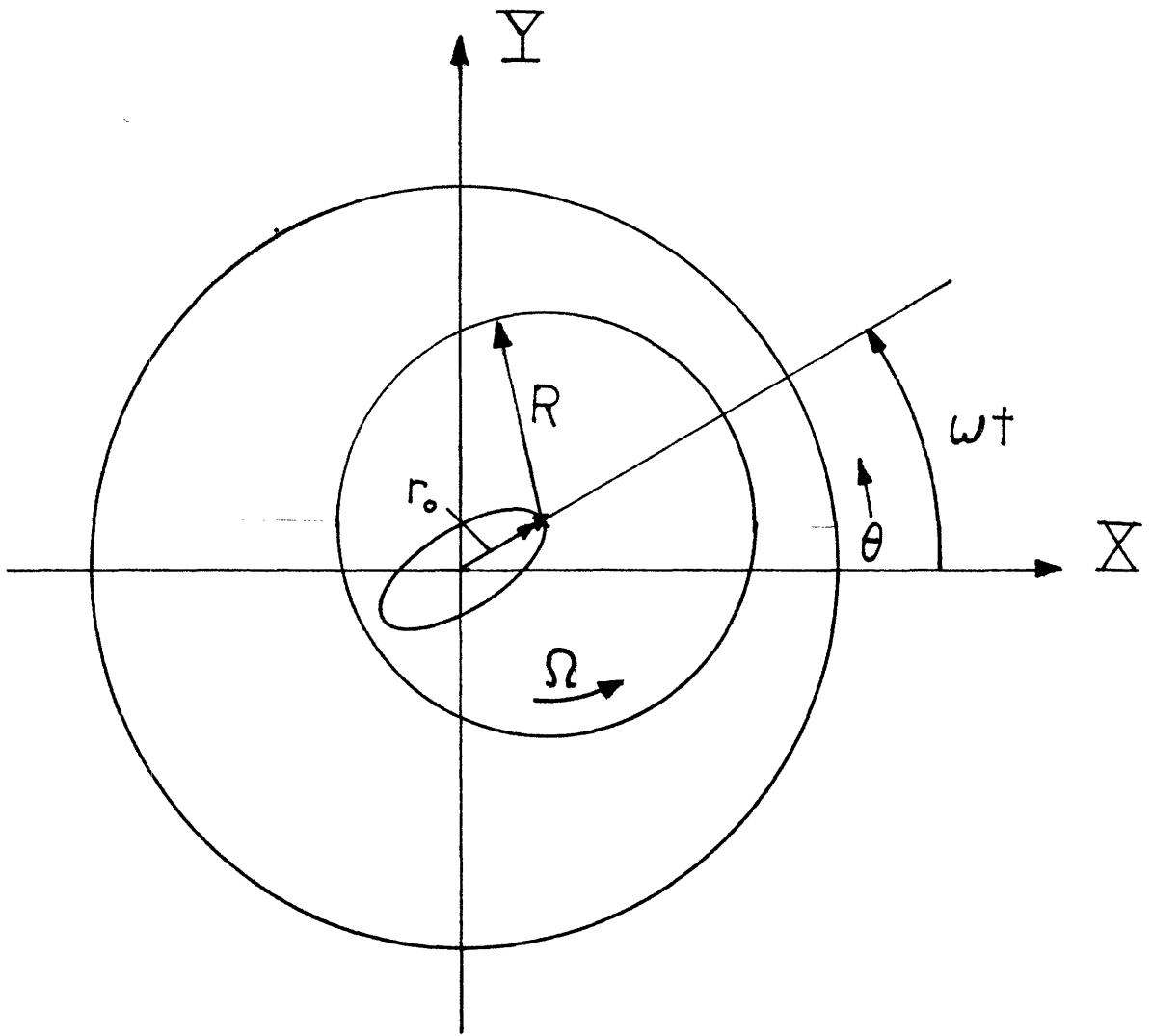


FIGURE 3 Dynamic orbit of the rotor center in a seal.

4. The orbit of the shaft is small compared to the radial tooth clearance. It is elliptical in shape with constant angular velocity.
5. The rotor is perturbed from the seal's geometric center in a parallel fashion. No skewing of the rotor is permitted.
6. The fluid obeys the perfect gas law.

These assumptions are applied to the principles of continuity and momentum in each chamber to determine the spatial and temporal variation of chamber pressure. The effects of each chamber are combined to establish the total force generated by the labyrinth seal.

2.2 Conservation of Mass

The principle of mass conservation is applied to a control volume shown in Figure 4 for the i th chamber. The dimensions of the chamber are assumed to be small compared to the radius, R , of the rotor. The equation for the conservation of mass can be written as

$$\text{Net mass into control vol.} = \frac{\partial}{\partial t} [\rho d(\text{Volume})] \quad (1)$$

Expanding equation (1) in differential terms gives

$$q_i dx - q_{i+1} dx + (\rho_i c_i f_i)$$

$$\begin{aligned}
& - (\rho_i + \rho_i' dx) (c_i + c_i' dx) (f_i + f_i' dx) \\
& = \frac{\partial}{\partial t} (\rho_i f_i dx) \tag{2}
\end{aligned}$$

where

x - distance measured in circumferential direction

q - mass flow rate per unit length

ρ - fluid density

c - mean tangential velocity of fluid in chamber

f - chamber cross-sectional area

$()'$ - partial derivative with respect to x .

Combining terms and neglecting higher order effects yields

$$\frac{\partial}{\partial t} (\rho_i f_i) + \frac{\partial}{\partial x} (\rho_i c_i f_i) + q_{i+1} - q_i = 0. \tag{3}$$

This is a more general form of the equation derived by T. Iwatsubo⁽⁸⁾. In his formulation, Iwatsubo assumed that the spatial variation in area was negligible compared to variations in density and velocity. While both clearance and area were expressed in terms of x and t , partial derivatives with respect to x were neglected.

2.3 Conservation of Momentum

Again the Iwatsubo approach will be taken in deriving the momentum equation. Only the momentum change in the tangential

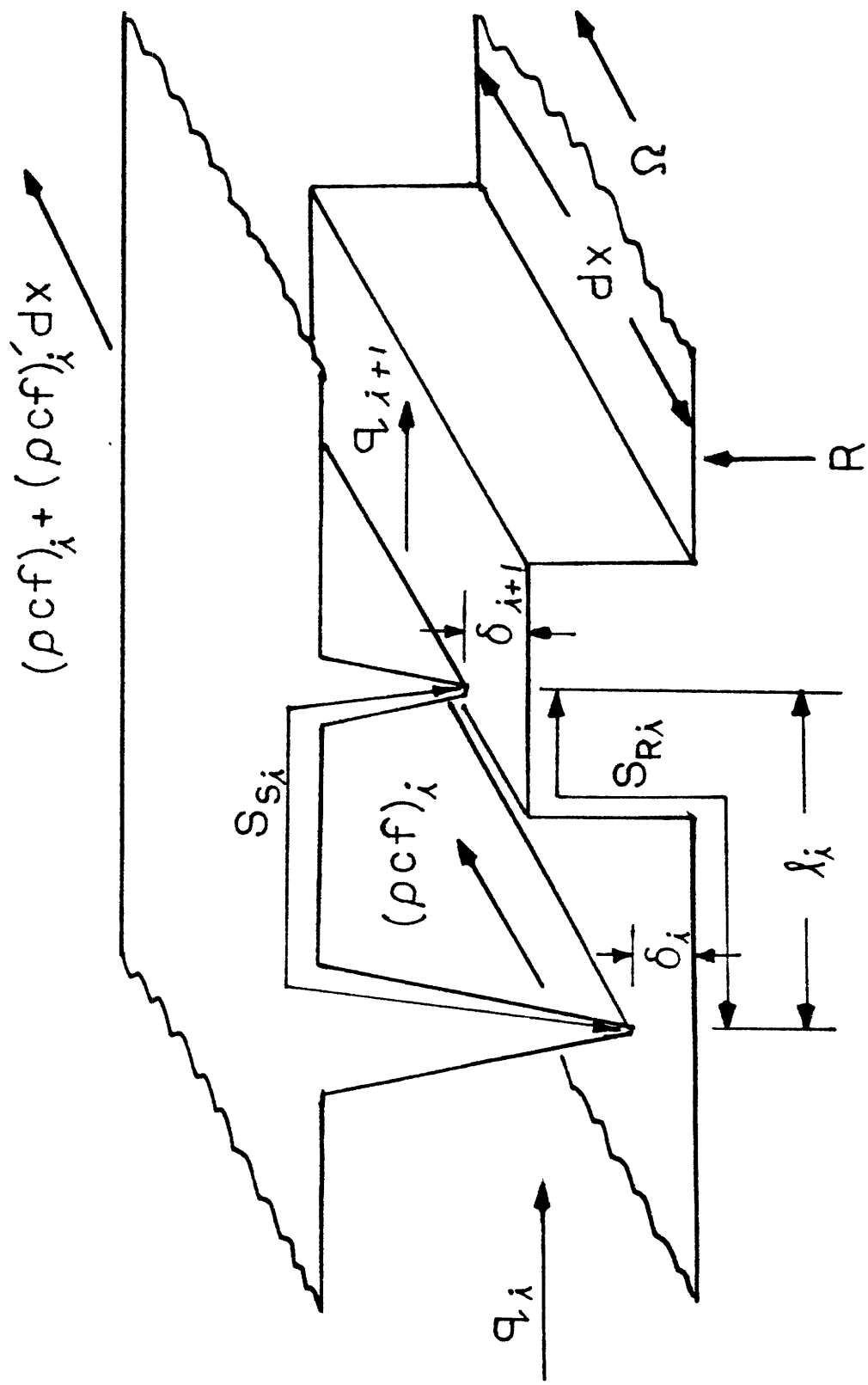


FIGURE 4 Geometry and fluid properties for conservation of mass control volume of the i th seal chamber.

direction is considered. The conservation of momentum equation can be written as

$$\int \text{Flux} = \frac{d}{dt} (\text{Momentum}) \quad (4)$$

Figure 5 shows the i th chamber with the influencing forces and momentum fluxes. The momentum equation in the x direction is

$$\begin{aligned} & P_i f_i - (P_i + P_i' dx) (f_i + f_i' dx) + P_i f_i' dx \\ & - \tau_{Si} S_{Si} dx + \tau_{Ri} S_{Ri} dx \\ & + q_i c_{i-1} dx - q_{i+1} c_i dx \\ & + (\rho_i c_i f_i) c_i - (c_i + c_i' dx)^2 (\rho_i + \rho_i' dx) \cdot \\ & (f_i + f_i' dx) = \frac{\partial}{\partial t} (\rho_i c_i f_i dx). \end{aligned} \quad (5)$$

By combining terms equation (5) becomes

$$\begin{aligned} & \frac{\partial}{\partial t} (\rho_i c_i f_i) + \frac{\partial}{\partial x} (\rho_i c_i^2 f_i) + f_i \frac{\partial}{\partial x} P_i \\ & + \tau_{Si} S_{Si} - \tau_{Ri} S_{Ri} + q_{i+1} c_i - q_i c_{i-1} = 0. \end{aligned} \quad (6)$$

2.4 Thermodynamic Considerations

The fluid in the seal is assumed to behave as an ideal gas. As the fluid passes from sealing strip to sealing strip, the state of pressure reduces by throttling. Figure 6 shows how the pressure and axial velocity change as the fluid passes through

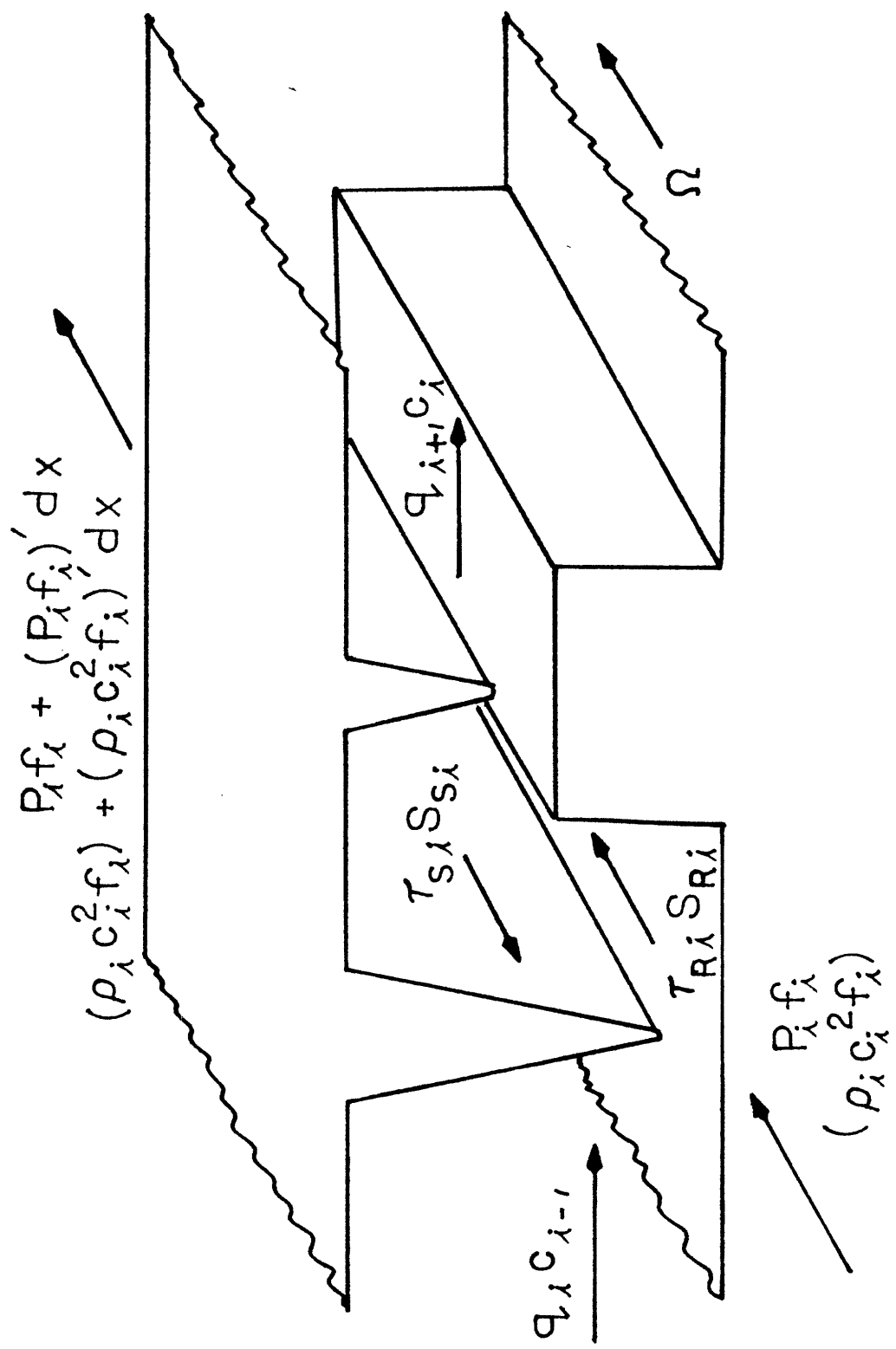


FIGURE 5 Control volume for conservation of momentum in tangential direction.

the seal on an enthalpy-entropy chart. A more detailed description of how the thermodynamic state changes in a labyrinth seal is given by Vermes⁽²⁾ and Meyer⁽³⁾. In the area of the sealing strip the fluid has a high axial velocity. Within the chamber the axial velocity is reduced and the impact pressure is assumed to be zero. As both Meyer and Vermes indicate, this is not entirely true. There is residual axial velocity in the chamber which is referred to as carry-over. This reduces the static pressure felt by the rotor. Stepped seal configurations have less carry-over than straight tooth seals. This difference will be neglected. It arises from the more homogeneous velocity distribution in a stepped seal design as a result of its better mixing quality. The straight seal requires less mixing of the leakage flow to get through the seal.

While in the chamber, the fluid is assumed to change isentropically in the tangential direction^{(6) (7) (8) (14)}. This means that both pressure, P , and density, ρ , obey the following relationship:

$$\frac{P}{\rho^\gamma} = \text{const.} \quad (7)$$

The specific heat ratio, γ , is approximately equal to 1.3 for superheated steam and 1.4 for a diatomic gas. Taking the time and spatial derivatives of equation (7) gives

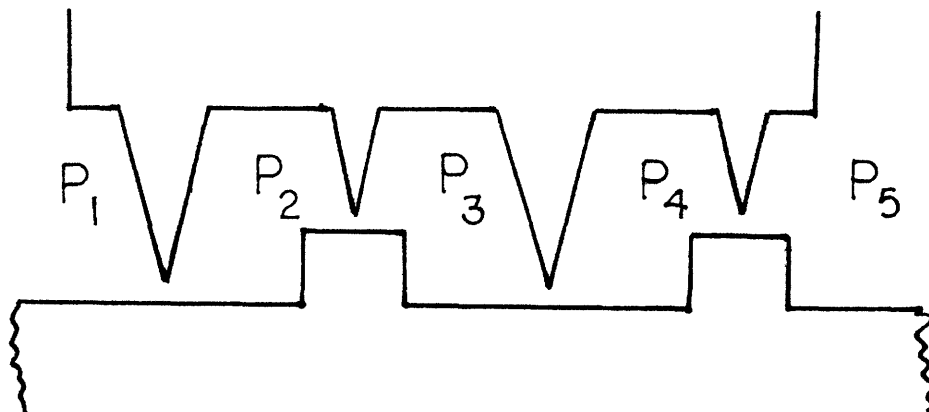
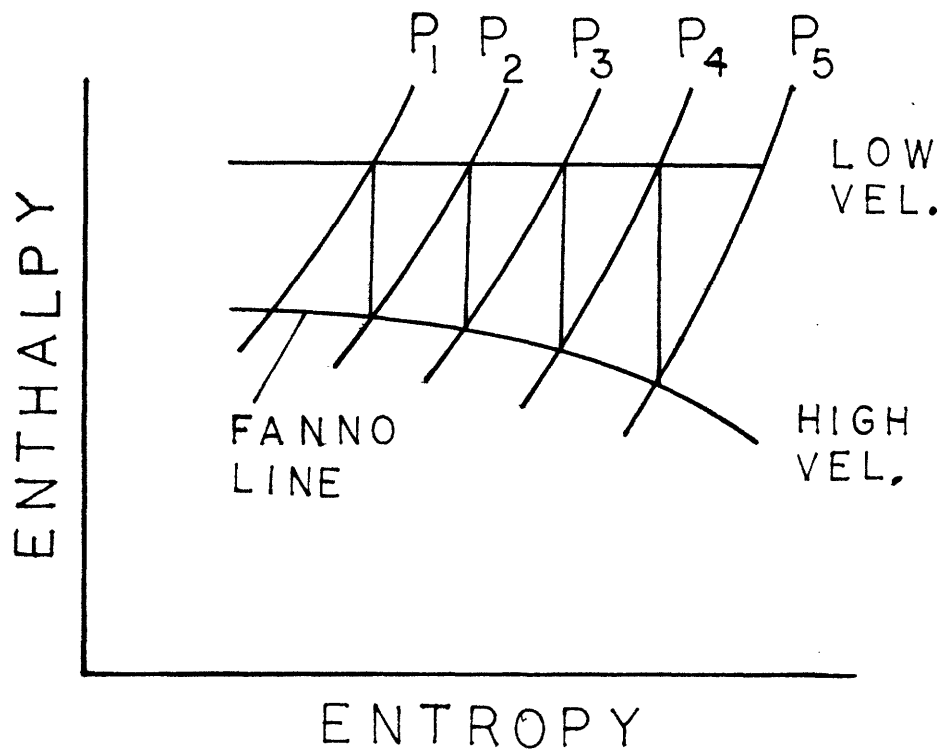


FIGURE 6 Enthalpy-entropy chart for fluid passing through a labyrinth seal.

$$\frac{\partial}{\partial t} \rho = \frac{1}{\gamma} \frac{\rho}{P} \frac{\partial P}{\partial t} \quad (8)$$

and

$$\frac{\partial \rho}{\partial x} = \frac{1}{\gamma} \frac{\rho}{P} \frac{\partial P}{\partial x} \quad (9)$$

Since the fluid is assumed to be ideal, the perfect gas state equation,

$$P = \rho RT, \quad (10)$$

can be applied to equations (8) and (9) to give

$$\frac{\partial \rho}{\partial t} = \frac{1}{\gamma} \frac{1}{RT} \frac{\partial P}{\partial t} \quad (11)$$

and

$$\frac{\partial \rho}{\partial x} = \frac{1}{\gamma} \frac{1}{RT} \frac{\partial P}{\partial x} \quad (12)$$

2.5 Fluid Mechanical Considerations

Martin's formula relates the leakage flow to the state of the gas at each end of the seal and seal geometry. The fluid is assumed to remain at constant temperature as it passes through the seal. One form of Martin's formula is

$$q = C_D \delta \frac{1}{RT} \left[\frac{P_1^2 - P_n^2}{n - \ln \frac{P_n}{P_1}} \right]^{1/2} \quad (13)$$

The leakage flow per inch of circumference, q , is related to the uniform radial clearance, entrance and exit pressures, the number of sealing strips and the overall flow coefficients, C_D . In general, the flow coefficient is a function of tooth configuration, clearance and pressure ratio across the seal. Strictly speaking, the above relationship can only be used for seals with four or more teeth. For less teeth the overall flow coefficient will vary for the same clearance and pressure ratio.

Since the equations for mass and momentum conservation are written on a per chamber basis, equation (13) must be in a compatible form. Martin's equation has been written on a per seal strip basis in references (7), (8), (13) and (14) as

$$P_{i-1}^2 - P_i^2 = \frac{q_i^2 RT}{\mu_i^2 \delta_i^2} \quad (14)$$

where μ is the local flow coefficient replacing C_D . The limitations made on equation (13) are removed by specifying μ for each seal strip in the labyrinth. As with the overall flow coefficient, μ is also a function of radial clearance and pressure ratio across the seal strip. Equation (14) relates the flow into and out of each chamber by local variables.

Equally important is the value for mean tangential velocity, c , of the fluid in each chamber. Knowledge of the drag forces from both rotating and stationary surfaces is key in establish-

ing c. A friction factor approach will be taken since the channels are non-circular with turbulent flow. As suggested in references (7), (8), (13) and (14), the drag force per unit circumferential length is

$$\tau s = F_{\text{drag}}/\text{unit length}$$

where τ is the shear stress and s is the wetted perimeter of the channel. For the stationary part of the seal chamber, the force per unit length is

$$\tau_{Si} S_{Si} = \frac{1}{2} \lambda_{Si} \rho_i c_i^2 S_{Si} \quad (15)$$

and for the rotating surface

$$\tau_{Ri} S_{Ri} = 1/2 \lambda_{Ri} \rho_i (u - c_i) \cdot |u - c_i| S_{Ri}. \quad (16)$$

The friction factor*, λ , shown in Figure 7 for turbulent flow in rough non-circular channels with a fully developed velocity distribution is given in Schlichting⁽¹⁵⁾ as

$$\frac{1}{\sqrt{\lambda}_o} = .87 - \log \left(\frac{ks}{R_h} + \frac{37.4}{\text{Re} \sqrt{\lambda}_o} \right) \quad (17)$$

* The more commonly used expression for λ in the turbulent regime is the Blasius approximation:

$$\lambda_o = .0791 \text{Re}^{-1/4} .$$

This approximation starts to deviate from test data at Reynolds numbers greater than 10^5 . Typical applications of seals in compressors have Reynolds numbers in excess of 10^7 .

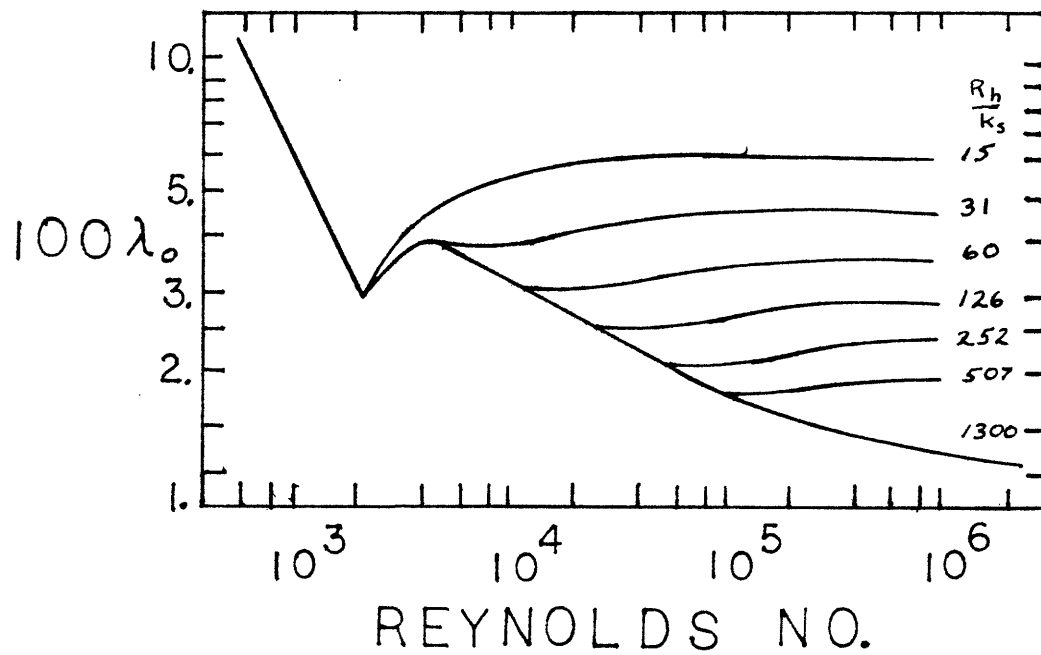


FIGURE 7 Friction factor chart for fully developed laminar and turbulent flow through rough pipes.

and

$$\lambda_o = Re/16. \quad (18)$$

for laminar flow.

The Reynolds number, Re, is given by

$$(Re)_{Si} = \frac{2 c_i R_{hi}}{v_i} \quad (19)$$

for the stationary surface and

$$(Re)_{Ri} = \frac{2 |u-c_i| R_{hi}}{v_i} \quad (20)$$

for the rotating surface. The hydraulic radius, R_h , is defined as

$$R_h = \frac{2f}{S_S + S_R} = \frac{2 \cdot X - \text{Area}}{\text{Wetted Perimeter}} \quad (21)$$

The equivalent roughness, k_s , for a channel can be shown to be related to the RMS surface finish by

$$k_s = 2. (\text{RMS surface roughness}). \quad (22)$$

The effect of surface roughness has been neglected by many investigators.

Equation (17) would apply with Reynolds numbers from 2300 to 10^8 .

The Reynolds number of the chamber flow relative to the rotating surface may, under certain instances be laminar and turbulent relative to the stationary surfaces. Therefore, accurate friction factor representation in both regimes is required.

Other effects which can significantly modify the friction factor are channel curvature and entrance effects. The curvature effect⁽¹⁵⁾ can be approximated for turbulent flow by

$$\frac{\lambda}{\lambda_0} = 1 + .075 \text{ Re}^{1/4} \left(\frac{R_h}{R} \right)^{1/2} \quad (23)$$

and for laminar flow by

$$\frac{\lambda}{\lambda_0} = .1064 \left[\text{Re} \sqrt{\frac{R_h}{R}} \right]^{1/2} . \quad (24)$$

Strictly speaking, equations (23) and (24) apply only to a channel where all sides are stationary. It will be assumed that the effect on λ is the same when rotating surfaces are involved.

An increase in surface friction also occurs when the flow in the tangential direction has not fully developed. For turbulent flow in pipes, the local friction factor does not reach its equilibrium value until after the fluid has traveled at least 10 hydraulic diameters⁽¹⁷⁾⁽¹⁸⁾⁽²³⁾. For laminar flow at least 50 diameters are required. Figure 8 shows how the average friction factor over a channel length, L , changes with

Reynolds number for turbulent flow. The ratio $L/(2 \cdot R_h)$ used in Figure 8 can be approximated by ratioing the mean tangential velocity to the average axial velocity in the chamber,

$$\frac{L}{2 \cdot R_h} \sim \frac{c_i}{(Vax)_i} \quad (25)$$

where

$$(Vax)_i = \frac{q_i}{2 \rho_i R_{hi}} \quad (26)$$

The effective friction factor can be written in terms of multipliers for the various effects as

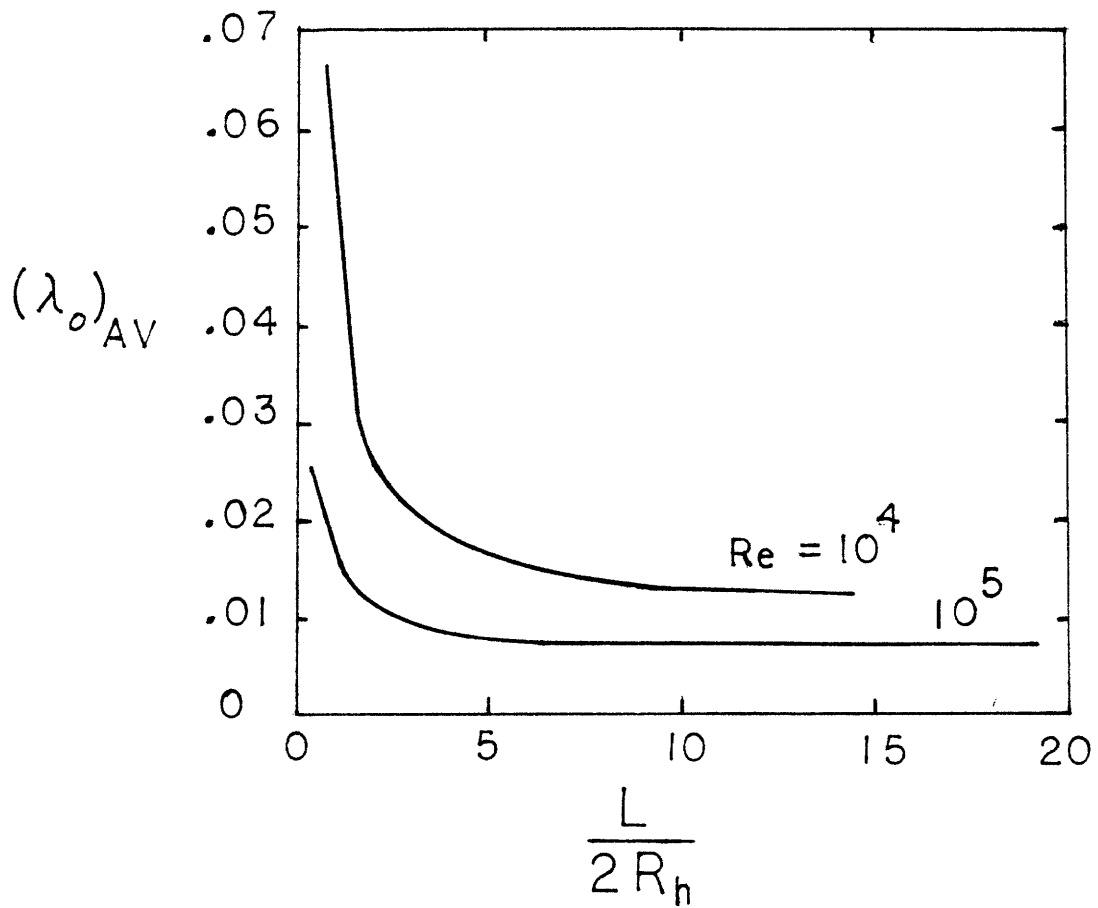
$$\lambda = \lambda_o \cdot \text{curvature factor} \cdot \text{entrance factor} \quad (27)$$

where λ_o includes the effects of surface roughness and Reynolds number.

An accurate representation of the friction factor is required. This will permit matching of calculated values with test results at low Reynolds numbers and accurate prediction of seal forces at design conditions with high Re values.

2.6 Steady-State Requirements

The method of solution as described by Iwatsubo will be to first consider the rotating shaft centered in the labyrinth with the fluid in each chamber at its steady-state value. The



$$\frac{L}{2R_h} \approx \frac{\bar{c}_\lambda}{(V_{ax})_\lambda}$$

FIGURE 8 Average friction factor for developing flow in pipes.

steady-state conditions are found by removing terms depending on time and spatial variation from the mass and momentum equations. Equations (3) and (6) reduce to

$$q_{i+1} - q_i = 0 \quad (28)$$

and

$$\tau_{Si} S_{Si} - \tau_{Ri} S_{Ri} + q_{i+1} c_i - q_i c_{i+1} = 0. \quad (29)$$

Equation (28) says that the flow is circularly uniform and constant through each seal strip. Equation (29) determines how the tangential velocity, c_i , of the fluid in each chamber must change to remain in equilibrium with the surface drag forces.

The procedure for establishing the steady-state values is straightforward. First the leakage flow rate is obtained from equation (13). Then the steady pressure, P_i , can be determined using equation (14) by starting with the first chamber and proceeding to the last. Since the gas is ideal and at constant temperature, the density distribution is also determined. The tangential velocity, c_i , for each chamber is found in a similar fashion. The inlet velocity, c_1 is either known or estimated and used in equation (29) to calculate c_2 in the first chamber. An iteration procedure is required to satisfy (29) since λ is also a function of c . Once c_2 sat-

isfies (29) for the first chamber, it is then used as the inlet condition for the second chamber. The process continues until the tangential velocity in each chamber is determined.

2.7 Dynamic Requirements

The rotor is now allowed to precess with an angular velocity, ω , in a small circular orbit of radius r_0 . The magnitude of r_0 is small compared to the mean clearance, $\bar{\delta}_i$, of the seal strip. Because of the precession, the clearance between the rotor and the i th seal strip will vary as

$$\delta_i = \bar{\delta}_i - r_0 \cos \left(\frac{\chi}{R} - \omega t \right) \quad (30)$$

The cross-sectional area also varies. For the i th chamber the area can be described by

$$f_i = \bar{f}_i - l_i r_0 \cos \left(\frac{\chi}{R} - \omega t \right) \quad (31)$$

where l is the distance between adjacent seal strips.

Since the disturbance is assumed to be small, variations in pressure, velocity, leakage rate and density will also be small and will be represented by perturbations superposed on the steady-state value:

$$\begin{aligned}
P_i &= \bar{P}_i + \hat{P}_i \\
c_i &= \bar{c}_i + \hat{c}_i \\
q_i &= \bar{q} + \hat{q}_i \\
\rho_i &= \bar{\rho}_i + \hat{\rho}_i
\end{aligned}
\tag{32}$$

Since both the clearance and chamber area variations can be thought of as a traveling wave, the other parameters can also be represented as a wave moving with the same velocity but with a relative phase angle, ϕ , associated with each. The pressure and tangential velocity can be described by

$$P_i = \bar{P}_i + \hat{P}_i = \bar{P}_i + P_{mi} \cos \phi_{pi} \tag{33}$$

$$c_i = \bar{c}_i + \hat{c}_i = \bar{c}_i + c_{mi} \cos \phi_{ci} \tag{34}$$

where

$$\phi = \frac{x}{R} - \omega t + \phi_i. \tag{35}$$

Since the fluid behaves as an ideal gas, the fluid density can be written as

$$\rho_i = \frac{1}{RT} \left(\bar{P}_i + P_{mi} \cos \phi_{pi} \right). \tag{36}$$

Changes in density with respect to location and time must also follow equations (11) and (12).

The equations for mass and momentum will be written in terms of (33) and (34). To accomplish this, the leakage flow rate will be written in terms of clearance and pressure variations. Equation (14) is rewritten as

$$q_i = \frac{\mu_i \delta_i}{\sqrt{RT}} \left(P_{i-1}^2 - P_i^2 \right)^{1/2} \quad (37)$$

Expanding the flow equations in terms perturbation variables gives

$$q_i = \frac{(\bar{\mu} + \hat{\mu})}{\sqrt{RT}} \left(\bar{\delta}_i + \hat{\delta}_i \right) \cdot \left[\left(\bar{P}_{i-1} + \hat{P}_{i-1} \right)^2 - \left(\bar{P}_i + \hat{P}_i \right)^2 \right]^{1/2} \quad (38)$$

Rearranging equation (38) and neglecting second order terms gives

$$q_i = q \left[\left(1 + \left(\frac{\partial \mu}{\partial \delta} \right) \frac{\bar{\delta}_i}{\mu_i} \right) \frac{\hat{\delta}_i}{\bar{\delta}_i} + \left(\frac{1}{1 - \left(\frac{\bar{P}_i}{\bar{P}_{i-1}} \right)^2} - \left(\frac{\partial \mu}{\partial \left(\frac{\bar{P}_i}{\bar{P}_{i-1}} \right)} \right)_i \frac{1}{\mu_i} \frac{\bar{P}_i}{\bar{P}_{i-1}} \right) \frac{\hat{P}_{i-1}}{\bar{P}_{i-1}} \right]$$

$$+ \left(\frac{-1}{\left(\frac{\bar{P}_{i-1}}{\bar{P}_i}\right)^2} + \left(\frac{\partial \mu}{\partial \left(\frac{P_i}{P_{i-1}}\right)} \right)_i \frac{1}{\mu_i} \frac{\bar{P}_i}{\bar{P}_{i-1}} \right) \frac{\hat{P}_i}{P_i} \right]. \quad (39)$$

The terms $\frac{\partial \mu}{\partial \delta} \frac{\delta}{\mu}$ and $\frac{\partial \mu}{\partial \left(\frac{P_i}{P_{i-1}}\right)} \frac{1}{\mu} \frac{P_i}{P_{i-1}}$ represent the percentage

change in flow coefficient with percentage changes in clearance and seal strip pressure ratio respectively.

There is also a variation in the drag force because of variations in the tangential velocity and density. Although the friction factor is affected by these variations, it will be assumed to be constant. Allowing P_i and c_i to vary in equation (15) gives

$$\tau_{Si} S_{Si} = 1/2 \lambda_{Si} S_{Si} \left(\bar{\rho}_i + \hat{\rho}_i \right) \left(\bar{c}_i + \hat{c}_i \right)^2. \quad (40)$$

Using the ideal gas law, equation (40) can be rewritten as

$$\tau_{Si} S_{Si} = 1/2 \lambda_i S_i \frac{\bar{P}_i u^2}{RT} \left[\left(\frac{\bar{c}_i}{u} \right)^2 + \left(\frac{\hat{c}_i}{u} \right)^2 \frac{\hat{P}_i}{\bar{P}_i} + 2 \frac{\bar{c}_i}{u} \frac{\hat{c}_i}{u} \right]. \quad (41)$$

The corresponding drag force on the rotating surface is

$$\tau_{Ri} S_{Ri} = 1/2 \lambda_{Ri} S_{Ri} \left(\bar{\rho}_i + \hat{\rho}_i \right) \left[u - \left(\bar{c}_i + \hat{c}_i \right) \right]^2 \quad (42)$$

or

$$\begin{aligned} \tau_{Ri} S_{Ri} = 1/2 \lambda_{Ri} S_{Ri} \frac{\bar{P}_i u^2}{RT} & \left[\left(1 - \frac{\bar{c}_i^2}{u^2} \right) \right. \\ & \left. + \left(1 - \frac{c_i}{u} \right)^2 \frac{\hat{P}_i}{P_i} - 2 \left(1 - \frac{\bar{c}_i}{u} \right) \frac{\hat{c}_i}{u} \right]. \end{aligned} \quad (43)$$

Each term in the mass and momentum equations can now be represented by constants and variations in pressure and tangential velocity. First, the conservation of mass equation, (3), is expanded as

$$\begin{aligned} \dot{\rho}_i f_i + \rho \dot{f}_i + \rho_i' c_i f_i + \rho_i c_i f_i' + \rho_i c_i' f_i \\ + q_{i+1} - q_i = 0. \end{aligned} \quad (44)$$

In dimensionless form (44) becomes

$$\begin{aligned} \frac{\bar{P}_i \bar{f}_i}{RT \bar{q}} \left[\frac{1}{\gamma} \frac{\dot{P}_i}{\bar{P}_i} + \frac{\dot{f}_i}{\bar{f}_i} \right] \\ + \frac{\bar{P}_i \bar{f}_i u}{RT \bar{q}} \left[\frac{1}{\gamma} \frac{P_i'}{\bar{P}_i} \frac{c_i}{u} + \frac{c_i'}{u} + \frac{c_i}{u} \frac{f_i'}{\bar{f}_i} \right] \\ + \frac{\hat{q}_{i+1}}{\bar{q}} - \frac{\hat{q}_i}{\bar{q}} = 0. \end{aligned} \quad (45)$$

Substituting equations (33) through (36) and (39) into equation (45) gives

$$\begin{aligned}
& \left[\frac{-1}{1 - \left(\frac{\bar{P}_i}{\bar{P}_{i-1}}\right)^2} + \frac{\partial \mu}{\partial \left(\bar{P}_i/\bar{P}_{i-1}\right)} \frac{1}{\bar{\mu}} \frac{\bar{P}_i}{\bar{P}_{i-1}} \right] \frac{P_{mi-1}}{\bar{P}_{i-1}} \cos \phi_{P_{i-1}} \\
& + \left[\frac{\bar{P}_i \bar{f}_i \Omega}{RT \bar{q}} - \frac{1}{\gamma} \left(\frac{\omega}{\Omega} - \frac{c_i}{u} \right) \right] \frac{P_{mi}}{\bar{P}_i} \sin \phi_{P_i} \\
& + \left[\frac{1}{1 - \left(\frac{\bar{P}_{i+1}}{\bar{P}_i}\right)^2} + \frac{1}{\left(\frac{\bar{P}_{i-1}}{\bar{P}_i}\right)^2 - 1} - \frac{\partial \mu_{i+1}}{\partial \left(\frac{\bar{P}_{i+1}}{\bar{P}_i}\right)} \frac{1}{\bar{\mu}_{i+1}} \frac{\bar{P}_{i+1}}{\bar{P}_i} \right. \\
& \quad \left. - \frac{\partial \mu_i}{\partial \left(\frac{\bar{P}_{i-1}}{\bar{P}_i}\right)} \frac{1}{\bar{\mu}_i} \frac{\bar{P}_i}{\bar{P}_{i-1}} \right] \frac{P_{mi}}{\bar{P}_i} \cos \phi_{P_i} \\
& + \left[-\frac{1}{\left(\frac{\bar{P}_i}{\bar{P}_{i+1}}\right)^2 - 1} + \frac{\partial \mu_i}{\partial \left(\bar{P}_{i+1}/\bar{P}_i\right)} \frac{1}{\bar{\mu}_i} \frac{\bar{P}_{i+1}}{\bar{P}_i} \right] \frac{P_{mi+1}}{\bar{P}_{i+1}} \cos \phi_{P_{i+1}} \\
& + \left[-\frac{\bar{P}_i \bar{f}_i \Omega}{RT \bar{q}} \right] \frac{c_{mi}}{u} \sin \phi_{ci} \\
& = \left[\frac{\bar{P}_i \bar{f}_i \Omega}{RT \bar{q}} - \frac{l_i r_o}{\bar{f}_i} \left(\frac{\omega}{\Omega} - \frac{c_i}{u} \right) \right] \sin \left(\frac{x}{R} - \omega t \right) \\
& + \left[\frac{1}{\bar{\delta}_{i+1}} \left(1 + \frac{\partial \mu}{\partial \delta} \frac{\delta}{\bar{\mu}} \right)_{i+1} - \frac{1}{\bar{\delta}_i} \left(1 + \frac{\partial \mu}{\partial \delta} \frac{\delta}{\bar{\mu}} \right)_i \right] \cdot
\end{aligned}$$

$$r_0 \cos \left(\frac{x}{R} - \omega t \right). \quad (46)$$

A similar procedure is used for the momentum equation. Expanding equation (6) gives

$$\begin{aligned} & \dot{\rho}_i c_i f_i + \rho_i \dot{c}_i f_i + \rho_i c_i \dot{f}_i + \rho_i c_i^2 f_i \\ & + 2 \rho_i c_i c_i' f_i + \rho_i c_i^2 f_i' + P_i' f_i + \tau_{Si} S_{Si} \\ & - \tau_{Ri} S_{Ri} + q_{i+1} c_i - q_i c_{i-1} = 0. \end{aligned} \quad (47)$$

Using equations (11) and (12), equation (47) can be written in dimensionless form as

$$\begin{aligned} & \frac{\bar{P}_i \bar{f}_i \Omega}{RT \bar{q}} \left[\frac{1}{\Omega} \frac{1}{\gamma} \frac{\bar{P}_i}{P_i} \frac{c_i}{u} + \frac{1}{\Omega} \frac{\dot{c}_i}{u} + \frac{1}{\Omega} \frac{c_i}{u} \frac{\dot{f}_i}{\bar{f}_i} \right. \\ & \left. + \frac{1}{\Omega} \frac{u}{\gamma} \frac{P_i'}{P_i} \left(\frac{c_i}{u} \right)^2 + 2 u \frac{\bar{c}_i}{u} \frac{c_i'}{u} + \frac{u}{\Omega} \left(\frac{\bar{c}_i}{u} \right)^2 \frac{f_i'}{\bar{f}_i} \right] \\ & + \frac{\bar{P}_i \bar{f}_i}{\bar{q} u} \frac{P_i'}{P_i} + \frac{\tau_{Si} S_{Si}}{\bar{q} u} - \frac{\tau_{Ri} S_{Ri}}{\bar{q} u} \\ & + \frac{q_{i+1}}{\bar{q}} \frac{c_i}{u} - \frac{q_i c_{i-1}}{\bar{q} u} = 0. \end{aligned} \quad (48)$$

Substituting equations (33) - (36), (39) (41) and (43) into (48) gives

$$\begin{aligned}
& \left[\frac{\bar{P}_i \bar{f}_i \Omega}{RT \bar{q}} \frac{1}{\gamma} \frac{\bar{C}_i}{u} \left(\frac{\omega}{\Omega} - \frac{\bar{C}_i}{u} \right) - \frac{\bar{P}_i \bar{f}_i}{\bar{q} \Omega R^2} \right] \frac{P_{mi}}{\bar{P}_i} \sin \phi_{P_i} \\
& + \left[\frac{\lambda_{Si} S_{Si} \bar{P}_i u}{2 \bar{q} RT} \left(\frac{\bar{C}_i}{u} \right)^2 - \frac{\lambda_{Ri} S_{Ri} \bar{P}_i u}{2 \bar{q} RT} \left(1 - \frac{\bar{C}_i}{u} \right)^2 \right. \\
& + \left. \left[\frac{1}{1 - \left(\frac{\bar{P}_{i+1}}{\bar{P}_i} \right)^2} - \left(\frac{\partial \mu}{\partial \left(\bar{P}_{i+1}/\bar{P}_i \right)} \frac{1}{\bar{\mu}} \frac{\bar{P}_{i+1}}{\bar{P}_i} \right)_{i+1} \right] \frac{\bar{C}_i}{u} \right. \\
& + \left. \left[\frac{1}{\left(\frac{\bar{P}_{i-1}}{\bar{P}_i} \right)^2} - \left(\frac{\partial \mu}{\partial \left(\bar{P}_i/\bar{P}_{i-1} \right)} \frac{1}{\bar{\mu}} \frac{\bar{P}_i}{\bar{P}_{i-1}} \right)_i \frac{\bar{C}_{i-1}}{u} \right] \right] \frac{P_{mi}}{\bar{P}_i} \cos \phi_{P_i} \\
& + \left[- \frac{1}{1 - \left(\frac{\bar{P}_i}{\bar{P}_{i-1}} \right)^2} + \left(\frac{\partial \mu}{\partial \left(\bar{P}_i/\bar{P}_{i-1} \right)} \frac{1}{\bar{\mu}} \frac{\bar{P}_i}{\bar{P}_{i-1}} \right)_i \frac{\bar{C}_{i-1}}{u} \right] \frac{P_{mi-1}}{\bar{P}_{i-1}} \cos \phi_{P_{i-1}} \\
& + \left[\frac{\bar{P}_i \bar{f}_i \Omega}{\bar{q} RT} \left(\frac{\omega}{\Omega} - \frac{2\bar{C}_i}{u} \right) \right] \frac{C_{mi}}{u} \sin \phi_{C_i}
\end{aligned}$$

$$\begin{aligned}
& + \{-1\} \frac{C_{mi-1}}{u} \cos \phi_{C_{i-1}} \\
& + \left[\frac{\lambda_{Si} S_{Si} \bar{P}_i u}{\bar{q} RT} \left(\frac{\bar{C}_i}{u} \right) + \frac{\lambda_{Ri} S_{Ri} \bar{P}_i u}{\bar{q} RT} \left(1 - \frac{\bar{C}_i}{u} \right) \right. \\
& \left. + 1 \right] \frac{C_{mi}}{u} \cos \phi_{C_i} \\
& = \left[\frac{\bar{P}_i \bar{f}_i \Omega}{\bar{q} RT} \frac{r_i r_o}{\bar{f}_i} \frac{\bar{C}_i}{u} \left(\frac{\bar{C}_i}{R} - \frac{\bar{C}_i}{u} \right) \right. \\
& \quad \left. \sin \left(\frac{x}{R} - \omega t \right) \right. \\
& \quad \left. + \left[\frac{1}{\bar{\delta}_{i+1}} \left(1 + \frac{\partial \mu}{\partial \delta} \frac{\delta}{\mu} \right) \right]_{i+1} \frac{C_i}{u} \right. \\
& \quad \left. - \frac{1}{\bar{\delta}_i} \left(1 + \frac{\partial \mu}{\partial \delta} \frac{\delta}{\mu} \right) \right]_i \frac{C_{i-1}}{u} \Big]_{r_o} \cos \frac{x}{R} - \omega t. \tag{49}
\end{aligned}$$

The dynamic equations, (46) and (49), are in the form of forward traveling waves for pressure and velocity. These results are easily extended to the backward rotor whirl case for the same inlet swirl velocity and rotor spin. The time and spatial description for clearance, area, pressure and velocity for the i th chamber are

$$\delta_{iB} = \bar{\delta}_i - r_o \cos \left(\frac{x}{R} + \omega t \right)$$

$$f_{iB} = \bar{f}_i - l_i r_o \cos \left(\frac{x}{R} + \omega t \right)$$

$$P_{iB} = \bar{P}_i + P_{mi_B} \cos \left(\frac{x}{R} + \omega t + \phi_i \right)_B$$

$$c_{iB} = \bar{c}_i + c_{mi_B} \cos \left(\frac{x}{R} + \omega t + \phi_{ci} \right)_B \quad (50)$$

When the above equations are used, the resulting mass and momentum equations are identical to equations (46) and (49) except for a sign change on all terms with ω .

III. AERO-ELASTIC FORCES

3.1 Stiffness and Damping Coefficients

To evaluate the impact of seal forces on turbomachinery stability, the seal will be modeled with eight stiffness and damping coefficients. The logarithmic decrement will be calculated for each flexural mode of the rotor system. The rotor system includes all journal bearings, rotor shaft, bearing supports and labyrinth seals. Other sources of aerodynamic forces include circumferential variation in blade or impeller efficiency, annular seals, and fluid forces on wheel surfaces. These will be neglected in this analysis. The lumped mass, transfer matrix approach as described by Lund⁽¹⁶⁾ will be used to establish the damped natural frequencies and mode shapes of the system.

The coefficients required to represent a labyrinth seal are obtained by determining how the pressure in each chamber varies with shaft motion. Two methods are described in the Appendix for determining the circular variation in pressure in each chamber.

With the pressure variation in each chamber determined, the resulting force on the rotor can be found by integrating the pressure in each seal chamber and summing all chambers. For

the forward whirl case, the force in the \bar{X} direction is

$$\overline{F_X}_F = \sum_0^n \int_0^{2\pi} \ell_i \overline{P_i} \frac{P_{mi}}{\overline{P_i}} \cos(\theta - \omega t + \phi_{Pi}) F \cdot \cos(\theta) R d\theta \quad (51)$$

and in the \overline{Y} direction

$$\overline{F_Y}_F = \sum_0^n \int_0^{2\pi} \ell_i \overline{P_i} \frac{P_{mi}}{\overline{P_i}} \cos(\theta - \omega t + \phi_{Pi}) F \cdot \sin(\theta) R d\theta \quad (52)$$

Equations (51) and (52) are integrated to give

$$\overline{F_X}_F = -R \pi \sum \ell_i \overline{P_i} \frac{P_{mi} F}{\overline{P_i}} \cos(-\omega t + \phi_{Pi}) \quad (53)$$

$$\overline{F_Y}_F = -R \pi \sum \ell_i \overline{P_i} \frac{P_{mi} F}{\overline{P_i}} \cos(-\omega t + \phi_{Pi}) \quad (54)$$

The reaction forces for the backward whirl case are of similar form and are

$$\overline{F_X}_B = -R \pi \sum \ell_i \overline{P_i} \frac{P_{mi} B}{\overline{P_i}} \cos(\omega t + \phi_{Pi}) \quad (55)$$

and

$$\overline{F_Y}_B = -R \pi \sum \ell_i \overline{P_i} \frac{P_{mi} B}{\overline{P_i}} \sin(\omega t + \phi_{Pi}) \quad (56)$$

The two force components acting on the rotor can also be written in the form

$$- \underline{F}_{\underline{X}} = K_{11} \underline{\bar{X}} + K_{12} \underline{\bar{Y}} + C_{11} \dot{\underline{\bar{X}}} + C_{12} \dot{\underline{\bar{Y}}} \quad (57)$$

$$- \underline{F}_{\underline{Y}} = K_{21} \underline{\bar{X}} + K_{22} \underline{\bar{Y}} + C_{21} \dot{\underline{\bar{X}}} + C_{22} \dot{\underline{\bar{Y}}} \quad (58)$$

These two equations relate the displacement and velocity of the rotor center to horizontal and vertical forces with eight coefficients. If motion in only one direction is permitted then only four are required. With the rotor moving only in the $\underline{\bar{X}}$ direction, the two force components become

$$- \underline{F}_{\underline{X}} = K_{11} \underline{\bar{X}} + C_{11} \dot{\underline{\bar{X}}} \quad (59)$$

$$- \underline{F}_{\underline{Y}} = K_{11} \underline{\bar{X}} + C_{11} \dot{\underline{\bar{X}}} \quad (60)$$

Unidirectional motion in the $\underline{\bar{X}}$ direction can be obtained by combining the circular orbits of both forward and backward whirls. If for the forward whirl the displacement of the shaft is written as

$$r_F = r_o e^{j\omega t} \quad (61)$$

and the backward whirl condition

$$r_B = r_O e^{-j\omega t} \quad (62)$$

then

$$\bar{x} = \frac{r_F + r_B}{2} = r_O \cos \omega t \quad (63)$$

and

$$\dot{\bar{x}} = \frac{\dot{r}_F + \dot{r}_B}{2} = -\omega r_O \sin \omega t \quad (64)$$

By combining the horizontal and vertical force components for both whirl directions, the stiffness and damping coefficients can be written as

$$K_{11} = \frac{R \pi}{2 r_O} \sum_{i=1}^n l_i \left(P_{mi} \cos \phi_{Pi_F} + P_{mi} \cos \phi_{Pi_B} \right) \quad (65)$$

$$K_{21} = \frac{R \pi}{2 r_O} \sum_{i=1}^n l_i \left(P_{mi} \sin \phi_{Pi_F} + P_{mi} \sin \phi_{Pi_B} \right) \quad (66)$$

$$C_{11} = \frac{R \pi}{2 \omega r_O} \sum_{i=1}^n l_i \left(-P_{mi} \sin \phi_{Pi_F} + P_{mi} \sin \phi_{Pi_B} \right) \quad (67)$$

$$C_{21} = \frac{R \pi}{2 \omega r_O} \sum_{i=1}^n l_i \left(-P_{mi} \cos \phi_{Pi_F} + P_{mi} \cos \phi_{Pi_B} \right) \quad (68)$$

Since the rotor is disturbed from a central position in the seal, from symmetry the remaining four coefficients are

$$\begin{aligned} K_{22} &= K_{11} \\ K_{12} &= -K_{21} \\ C_{22} &= C_{11} \end{aligned} \quad (69)$$

$$C_{12} = -C_{21} .$$

With the linearized stiffness and damping coefficients, some general statements can be made on the impact of seals on stability. If the rotor is precessing in a circular orbit and for simplicity, the rotor center at $t = 0$ is at $\bar{x} = r_0$ and $\bar{y} = 0$,

the out-of-phase (destabilizing) force acting on the rotor is

$$\frac{F_{\bar{y}}}{t = 0} = -K_{21} r_0 - C_{22} r_0 \omega \quad (70)$$

From the symmetry of the system, the out-of-phase force is always equal to (70). Three possibilities exist. They are: destabilization in the forward whirl direction, destabilization in the backward whirl direction or stabilization for both. If

$$|K_{21}| > C_{22} \omega$$

and

$$K_{21} < 0$$

then the out of phase force tends to destabilize in the forward whirl direction. If

$$|K_{21}| > C_{22} \omega$$

and

$$K_{21} > 0$$

then the seal tends to destabilize the rotor in the backward whirl direction. When

$$|K_{21}| < \omega C_{22}$$

then the seal will remove energy from the rotor and stabilize in both whirl directions.

Because the rotor support system is generally asymmetrical with respect to stiffness and damping characteristics, a circular orbit may not exist in a seal. System asymmetry may change the energy absorption/dissipation nature of seals. The simple rules proposed for stabilizing/destabilizing cross-over point may not apply. This effect from asymmetry is discussed by D. Smith⁽¹⁹⁾. An example of this will be discussed in Section 4.

3.2 Comparison with Test Results

A valid calculation system must ultimately be compared to and agree with test data. Many times the data are difficult to obtain at actual design conditions because of either high temperatures and pressures or high leakage flow rates. Investigators such as Wright⁽²¹⁾, Spurk and Keiper⁽²⁰⁾, Kurobashi⁽¹⁴⁾, Benckert and Wachter⁽¹¹⁾⁽¹²⁾, all resorted to modeling the problem at modest leakage flow rates with smooth surfaces. Pressure drops across seals were on the order of

several atmospheres. Not all parameters are matched while testing under scaled conditions. One such parameter is the Reynolds number of the chamber swirl flow. Laboratory tests are generally conducted at Reynolds numbers in the neighborhood of 10^4 to 10^5 . At these low values, the chamber surfaces can be considered hydraulically smooth even though the flow is turbulent. For actual operating conditions the same location would have a Re value of 10^7 . For such values, surface roughness of the seal is critical in establishing the effective friction factor experienced by the leakage flow. Testing at low Reynolds numbers may tend to distort the role of friction in seal forces. This would lead to a less than adequate extrapolation to actual field conditions.

Despite this drawback and the fact that all measurements were taken on a non-whirling rotor, the Benckert and Wachter data do provide experimental results with which the proposed method can be compared. Such detailed chamber pressure for a four tooth, straight seal are found in Figure 2 of reference 11. The test conditions and configuration are shown in Figure 9. Each of the three chambers is instrumented with twelve static pressure taps to measure circumferential pressure variation. Data were recorded for preswirl velocities of 0 and 367 ft/sec with the rotor .014 inches eccentric from the seal center. The data are shown in Figures 10 and 12.

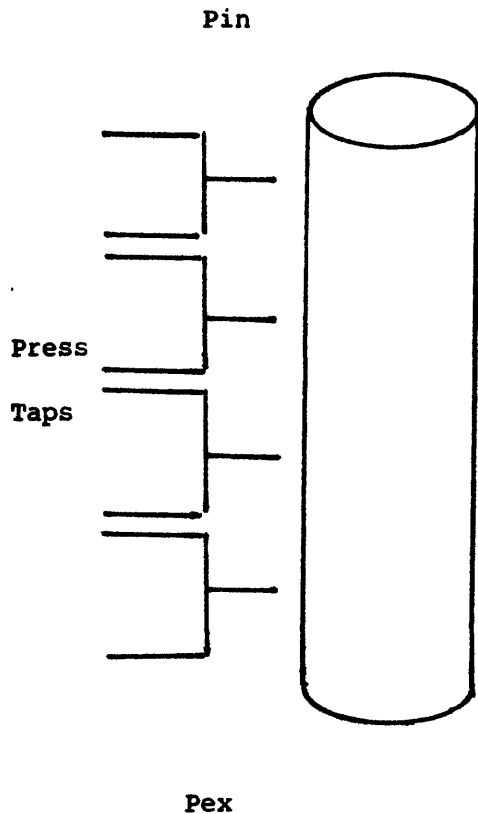
The criteria used to evaluate the predicted results with test data are the following:

1. Agreement on the mean pressure in each chamber.
2. Agreement on circumferential zero to peak pressure variation in each chamber.
3. Agreement on the phase of the pressure variation in each chamber.

Two sets of calculations were made to compare with the data. In the first calculation it was assumed that the flow coefficient for each seal strip was equal to the overall flow coefficient as described in Martin's formula. Also, it was assumed that each seal strip experiences the same percentage change in flow coefficient for changes in clearance and pressure ratio. These values were derived from test data published by Meyer⁽³⁾. The predicted pressure variation is compared with test data in Figure 10 and summarized in Table 1 for the 367 ft/sec preswirl case.

From the results shown, several discrepancies exist. The average pressure calculated is higher than that measured. The largest error occurred in the first chamber with the calculation predicting 1.89 PSIA higher than actually measured. The predicted values for the second and third chambers were high by

Benckert & Wachter



Fluid - Air

Rotor RPM - 0

P_{in} - 20.68 PSIA

P_{ex} - 13.83 PSIA

T - 75° °F

ρ - .104 lb/ft³

C_{in} - 367 ft/sec

- 0. ft/sec

R - 5.907 in

δ - .020 in

N - 4 teeth

Avg. Flow Coeff - 1.01

l - .316 in

h - .236 in

e - .014 in

l - pitch

h - chamber hgt

e - eccentricity

FIGURE 9 Geometry and flow conditions for Benckert and Wachter three chamber test seal.

.92 and .72 PSIA respectively. Measured zero-to-peak pressure variation in the first chamber was 3 times higher than predicted. Agreement on the second and third chambers was better but the calculation was still low by 17% and 24% for the two respective chambers. Measured phase relationships differ from the predicted value by -22.4° , 8.7° and -6.5° in each chamber respectively. These differences combine to give a predicted cross-coupling stiffness 53% of the measured value and a predicted direct stiffness 17% of the measured value.

When the predicted values are compared to measured data for the zero preswirl case, the discrepancies are more apparent. No pressure variation was predicted for this condition. Measured data showed a significant direct force in each of the chambers with the force decreasing chamber to chamber. The same trend in the direct force can be seen in the data taken with a preswirled 367 ft/sec.

The differences between the calculated and measured chamber pressures, both mean and zero-to-peak, can be reduced by examining the assumptions initially made. It was assumed that each seal strip had the same flow coefficient. In his testing, Meyer found a variation in flow coefficient from tooth to tooth for uniform clearance configurations. The value used in Martin's equation represents an average value for all seal strips. For a comparable configuration Meyer found the flow coefficient for the first strip to be between .6 and .8. This

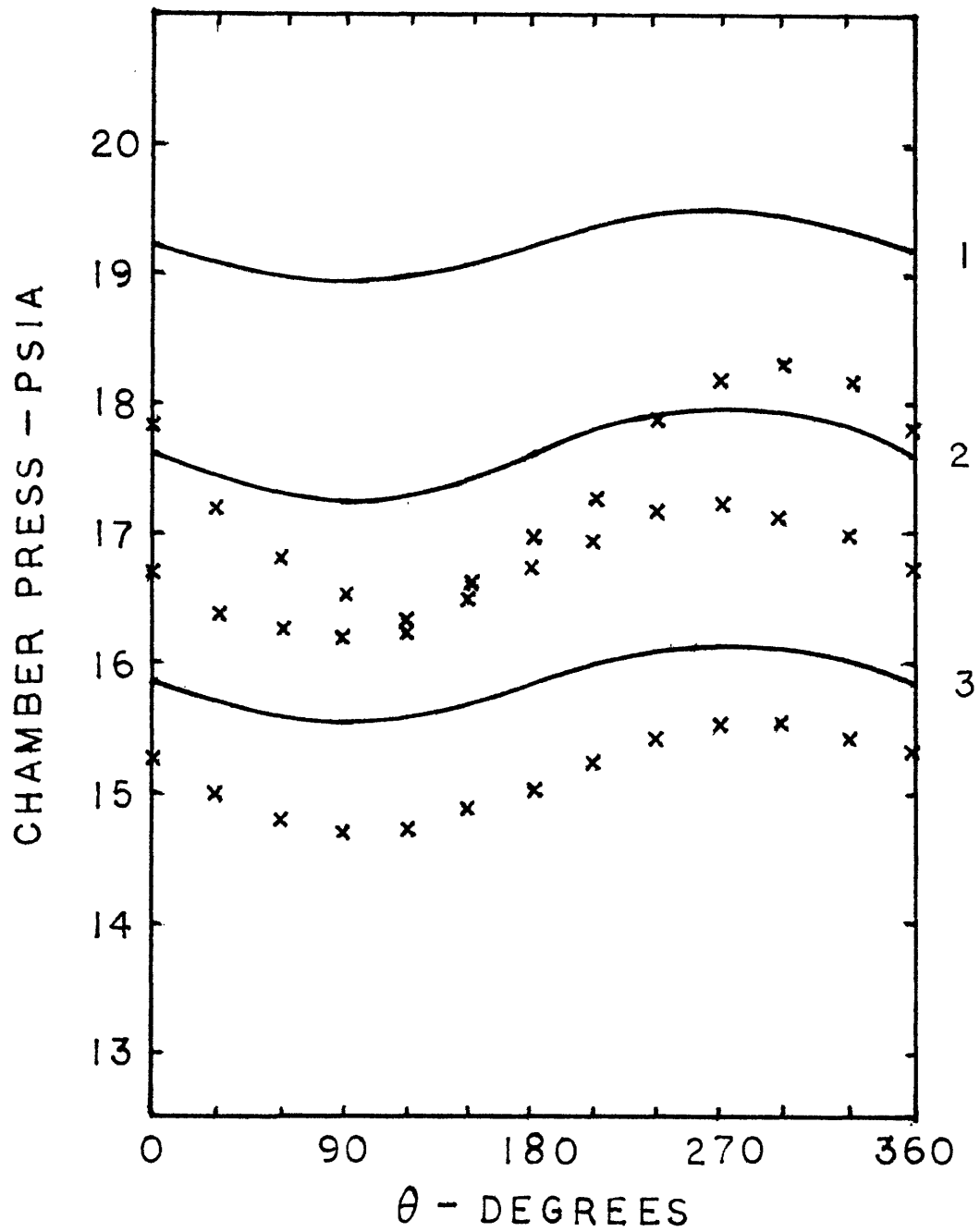


FIGURE 10 Comparison of predicted and calculated pressure distributions in each chamber for Figure 9. Predicted values are based on identical flow coefficients for each seal strip. Preswirl value - 367 ft/sec.

TABLE 1

COMPARISON OF CALCULATED AND
MEASURED FORCES FOR FIGURE 9

Measured Data

Preswirl ft/sec	Gradient lbf/in	Cham. No.	\overline{F}_X lbf	\overline{F}_Y lbf	\hat{P}_{o-p} PSI	ϕ deg.	\overline{P} PSIA
0.	$K_{11} = 106.$	1	-1.80	0.	.308	0.	17.02
	$K_{21} = 0.$	2	.45	0.	.077	180.	16.84
		3	-.11	0.	.019	0.	15.16
367.	$K_{11} = 212.$	1	-2.47	4.92	.943	63.	17.31
	$K_{21} = -758.$	2	.13	3.02	.516	93.	16.67
		3	-.58	2.45	.431	77.	15.10

Calculated Data

Preswirl ft/sec	Gradient lbf/in	Cham. No.	\overline{F}_X lbf	\overline{F}_Y lbf	\hat{P}_{o-p} PSI	ϕ deg.	\overline{P} PSIA
0.	$K_{11} = 0.$	1	0	0	0	0	19.20
	$K_{21} = 0.$	2	0	0	0	0	17.59
		3	0	0	0	0	15.82
367.	$K_{11} = 37.$	1	-.15	1.85	.318	85.	19.20
	$K_{12} = 403.$	2	-.25	2.50	.430	84.	17.59
		3	-.22	1.91	.329	84.	15.82

low value compared to the seal average value of 1.01 would produce a greater pressure drop across the first tooth. Based on Meyer's results, a flow coefficient distribution as shown in Table 2 was assumed next.

Since the flow coefficients are not identical in the seal, it is reasonable to assume that the percentage change in μ for a given change in clearance will also be different for each strip. Data in this area are very limited. The results published by Meyer show how the overall flow coefficient changes with clearance. Kurohashi represents the effect in terms of an equivalent clearance change.

$$\delta'_i = (1 + \xi_i) \delta_i \quad (71)$$

The constant ξ_i is inversely related to $\partial\mu/\partial\delta$. Data by Meyer suggest that as clearance decreases, the flow coefficient also decreases. In terms of Kurohashi's equivalent clearance, the flow coefficient would increase with decreasing clearance. In light of the apparently conflicting data, the approach taken was to use a trial and error procedure to determine what distribution best fits the test results. The values obtained are then judged on their reasonability. The same set of values were used for both preswirl cases. The values arrived at are shown in Table 2.

TABLE 2

DISTRIBUTION OF FLOW COEFFICIENTS FOR
 FIGURES 10, 11 AND 12

Tooth No.	μ	Figure 11	Figures 12 and 13	
		$\frac{\partial \mu / \mu}{\partial \delta / \delta}$	μ	$\frac{\partial \mu / \mu}{\partial \delta / \delta}$
1	1.01	.15	.70	.20
2	1.01	.15	1.01	.50
3	1.01	.15	1.01	.30
4	1.01	.15	1.20	.40
Effective Value	1.01		.92	

Figures 11 and 12 show the agreement between predicted and measured chamber pressures. Since the values were optimized, agreement is obviously improved. This is particularly true in predicting the pressure distributions for the zero preswirl case. The greatest error still exists in predicting the cross-coupling force in the first chamber. This optimization does show that agreement was obtained by assigning individual values for flow coefficient characteristics to each sealing strip. The values shown in Table 2 are within the range of expected variation based on test measurements⁽³⁾.

The circumferential velocity distribution is shown in Figure 13 for the 367 ft/sec preswirl case. This predicted distribution corresponds to the pressure distribution shown in Figure 11. Actual measurements to verify the velocity distribution would be difficult to obtain because of the highly complex flow pattern in the chamber. If possible, however, such measurements would indicate the apparent friction factor for the flow in each of the channels. Also shown is the average axial velocity of the flow across the chamber. The ratios of circumferential to axial velocity are 7.4, 5.2 and 3.7 for each consecutive chamber. For the above ratios, the flow is clearly still developing. This requires the average friction factors to be higher than the corresponding fully developed values.

While agreement was obtainable on direct stiffness values when detailed flow coefficient characteristics were assumed for each

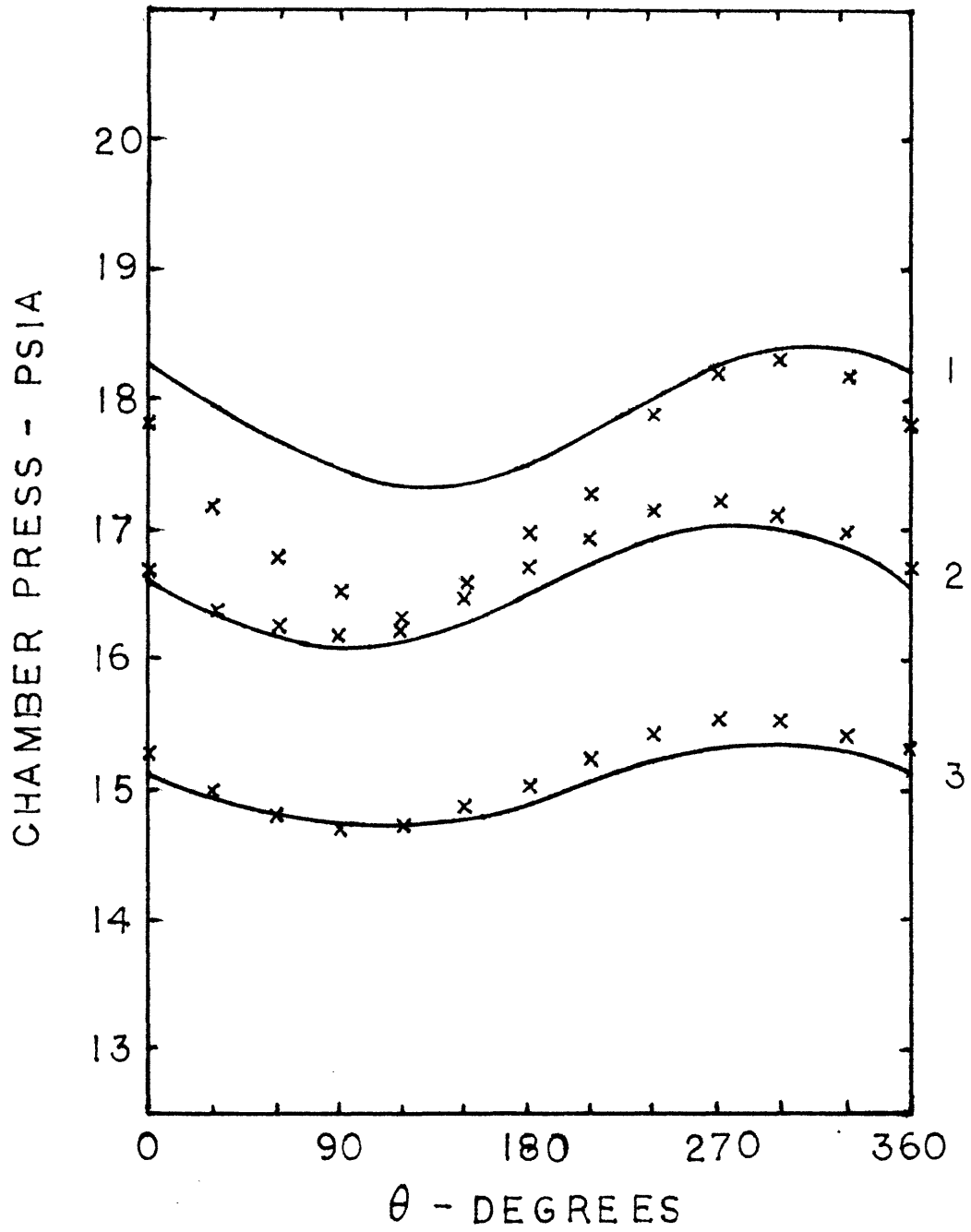


FIGURE 11 Comparison of predicted and calculated pressure distributions for Figure 9 with optimized seal strip flow coefficients. Preswirl value - 367 ft/sec.

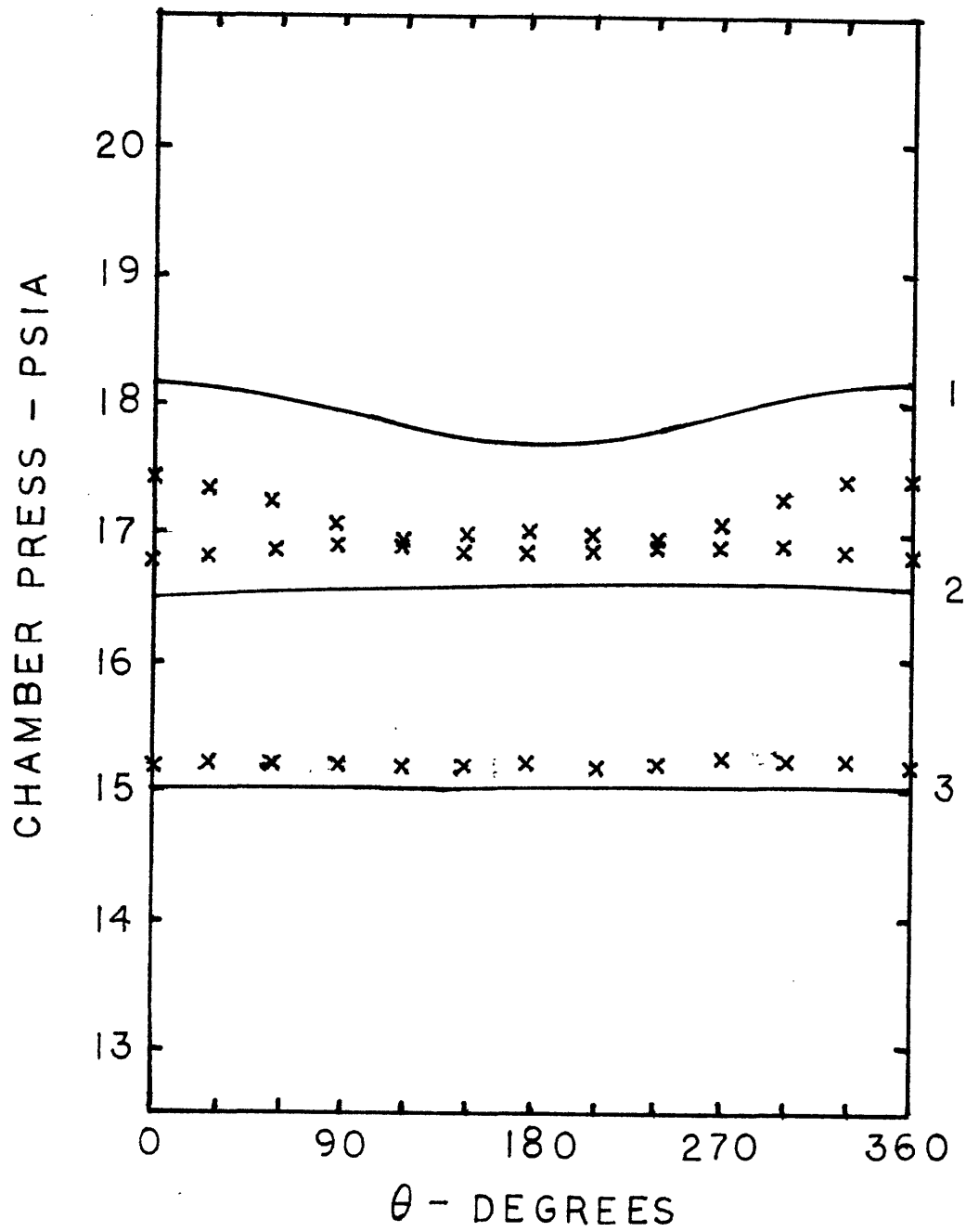


FIGURE 12 Comparison of predicted and calculated pressure distributions with optimized flow coefficients and zero preswirl.

TABLE 3

COMPARISON OF CALCULATED AND MEASURED FORCES FOR
FIGURES 11 AND 12Calculated Data

Preswirl ft/sec	Gradient lbf/in	Cham. No.	\bar{F}_X lbf	\bar{F}_Y lbf	\hat{P}_{o-p} PSI	ϕ deg.	\bar{P} PSIA
0		1	-1.51	0	.258	0	17.85
	$K_{11} = 98.$	2	.32	0	.055	180.	16.53
	$K_{21} = 0.$	3	-.19	0	.032	0	15.01
367		1	-2.12	2.45	.554	49.	17.85
	$K_{11} = 225.$	2	-.38	2.61	.452	82.	16.53
	$K_{21} = -477.$	3	-.66	1.61	.298	68.	15.01

tooth, the predicted cross-coupling stiffness was only improved by 10 percentage points to 63% of the measured value. In both Figures 10 and 11, the greatest discrepancies occurred in the first chamber. Since the seal had only three chambers, a large error in the first chamber would severely impact the overall agreement on stiffness values. The overall agreement might be improved for seals with more chambers. Figure 14 gives four additional cross-coupling stiffness comparisons of Benckert and Wachter data with calculated values. Straight seals with 8 and 17 chambers were compared for different tooth pitchings and inlet pressures. For these four cases, the error between test data and calculated values was at most 11%. This occurred for the 8 chamber case with the calculated value lower than the measured value. For the 17 chamber cases, the calculated values were within 3% of the measured values. The disagreement decreases as the number of chambers increases.

The test data so far compared to predicted values have only been for straight labyrinth seals. Figure 15 gives a comparison of test to predicted cross-coupling stiffnesses for a full labyrinth with 23 chambers. For the two cases shown, good agreement was obtained with the same prediction method. The calculated value was 13% higher than found from measurement at the higher speed. At the lower speed the two values agree within 1%.

	\bar{c}	\hat{c}_{o-p}	ϕ	V_{ax}	\bar{c}/V_{ax}
1	260.0	31.1	181.	35.4	7.4
2	197.4	29.6	176.	38.2	5.2
3	157.1	24.5	173.	42.1	3.7

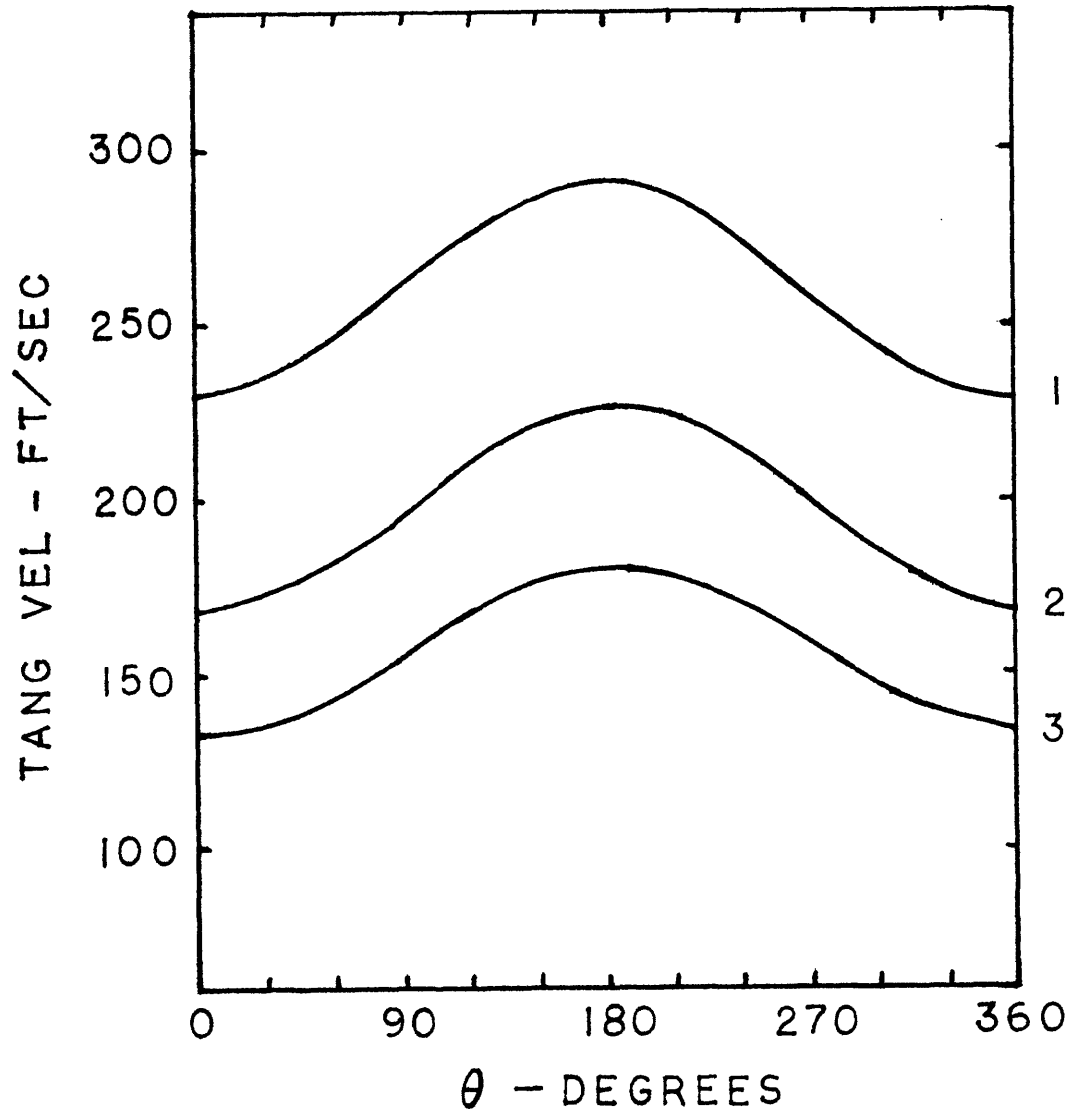


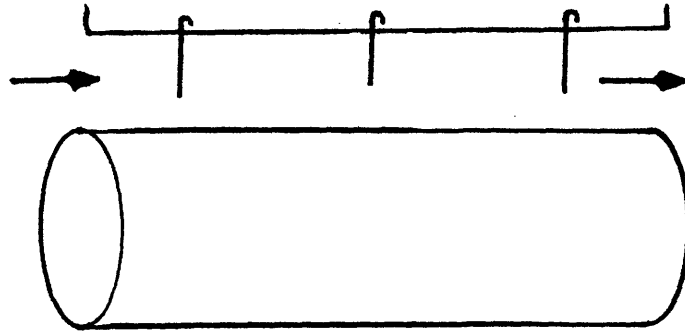
FIGURE 13. Calculated tangential velocity distributions for Figure 11.

Based on the last six cases, the suggested calculation method predicts the out-of-phase force level within 13% for a range of speeds from 0 to 9549 RPM and for both half and full labyrinth seal designs. These cases represent designs more commonly used in turbomachinery and would give a better indication of how predicted values agree with test data.

3.3 Influence of Seal Geometry, Preswirl and Rotor Angular Velocity

Section 3.2 demonstrated that reasonable agreement between the proposed calculation method and actual test data occurred when detailed flow coefficient characteristics were known. Agreement on the cross-coupling force is still good without this detailed data. From a stability point of view, it is desirable to understand how geometric parameter changes influence the magnitude and direction of the cross-coupling force. The direct force, while comparable in magnitude to the out-of-phase force, primarily influences the rotor's damped natural frequencies. Based on the results of Jenny⁽¹³⁾ and measurements made by Benckert and Wachter, changes in rotor criticals would be on the order of three percent for typical turbomachinery designs.

Two seals, one with 30 chambers and another with 3 chambers will be used to demonstrate the effect of parameter changes. Figure 16 gives the geometry and pressure drop across both seals. The two examples were taken from a sample calculation



Geometry

$R = 5.906 \text{ in}$

$\delta = .023 \text{ in}$

$\mu = 1.20$

$h = .236 \text{ in}$

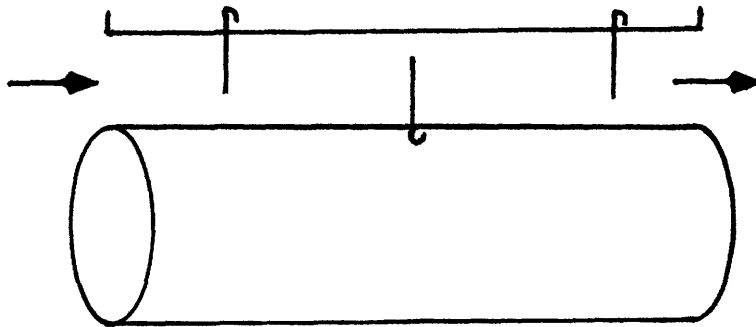
$u = 0$

$P_{ex} = 13.83 \text{ PSIA}$

$T = 75^\circ\text{F}$

Case	P_{in} PSIA	C_{in} ft/sec	M	l in	Calc. K_{12} lbf/in	Meas. K_{12} lbf/in
1	28.2	200	17	.194	162	166
2	35.5	200	17	.194	231	234
3	28.2	200	8	.394	150	166
4	35.5	200	8	.394	214	234

FIGURE 14 Comparison of calculated cross-coupling force gradients with Benckert and Wachter measurements on straight labyrinths.



Geometry

$R = 5.906$ in

$\delta = .020$ in

$\mu = .64$

$h = .236$ in

$l = .157$ in

$M = 23$

$P_{in} = 20.68$ PSIA

$P_{ex} = 13.83$ PSIA

$T = 75^\circ\text{F}$

Case	C_{in} ft/min	RPM	Calc. K_{12} lbf/in	Meas. K_{12} lbf/in
1	150	9549	285	251
2	95	7130	138	137

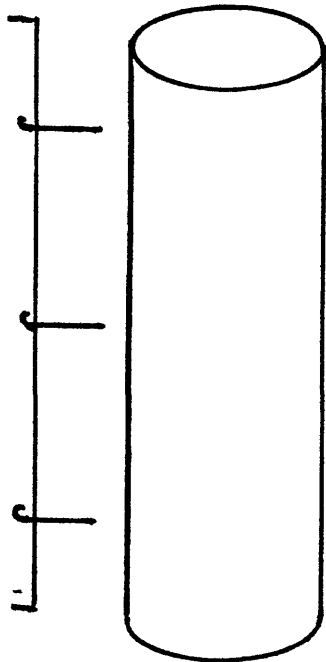
FIGURE 15 Comparison of calculated cross-coupling force gradients with Benckert and Wachter measurements on full labyrinths.

found in reference 12 by Benckert and Wachter. In addition to demonstrating how geometric changes to a seal alter the destabilizing force, two examples will also serve as additional checks on the proposed calculation method. Predicted values for both seals are given in Figure 16. Agreement between the Benckert and Wachter system and the comprehensive, theoretical method is very good. The 30 chamber seal force differs from the predicted value by 4% and the value for the 3 chamber seal differs by 8%. These values correspond to non-whirling shafts. Therefore, no whirl related forces are present. For illustration purposes, it will be assumed that the rotor has a natural frequency at 2500 RPM. The out-of-phase force will now include whirl related terms and will permit comparisons of calculated damping terms with cross-coupling stiffness terms.

Table 4 gives the values of the stiffness and damping coefficients for the base case of the 30 chamber seal and those for each geometric parameter change. Also shown are the corresponding values for three different preswirl speed fractions. The speed fraction corresponding to .36 has the fluid entering the seal at the equilibrium tangential velocity. As the preswirl velocity is increased to 80% of the surface velocity, u , there is a contribution to the destabilizing stiffness coefficient as a result of the reduction in tangential momentum of the fluid from frictional drag. The momentum reduction does not significantly affect the damping coefficient. When there is no preswirl in the fluid entering the seal, the tangential

BENCKERT & WACHTER EXAMPLE

NASA CP 2133 Pg 205



Geometry

R = 5.906 in
 δ = .010 in
 μ = .98
h = .236
l = .197
RPM = 12000
 C_{in} = 492 ft/sec
 P_{in} = 2900 PSIA
(N=4) P_{ex} = 2320 PSIA
(N=31) P_{ex} = 290 PSIA

Benckert & Wachter System

$$N = 4 \quad K_{12} = 5.14 \times 10^4 \text{ lb/in}$$

$$N = 31 \quad K_{12} = 1.43 \times 10^5 \text{ lb/in}$$

Predicted Cross-Coupling Stiffness

$$N = 4 \quad K_{12} = 4.95 \times 10^4 \text{ lb/in}$$

$$N = 31 \quad K_{12} = 1.56 \times 10^5 \text{ lb/in}$$

FIGURE 16 Comparison of calculated cross-coupling stiffness using the Benckert and Wachter method and using equations (46) and (49).

momentum of the fluid must increase through the seal. The impact is to reduce the value of K_{12} for the base configuration. Again the damping coefficient is not significantly affected.

The same geometric changes and preswirl speed fractions are applied to the seal with only 3 chambers. Table 5 gives the corresponding stiffness and damping coefficients for the different configurations. The same trend for changes in preswirl velocity can be seen in all cases. As the preswirl velocity is reduced, the cross-coupling stiffness, K_{12} , decreases. For the same conditions, K_{12} , can have a large negative value for zero preswirl.

Figures 17 through 22 show how the stiffness and damping coefficients change as a function of rotor speed. The whirl frequency was held constant at 2500 RPM. The damping coefficients are multiplied by the whirl frequency to allow direct comparison with the stiffness coefficients. The results are summarized in Table 6. For the case of the preswirl velocity equal to the equilibrium tangential velocity, the speed where the out-of-phase force goes to zero occurs at 7000 RPM. This corresponds to the ratio of $\Omega/\omega = 2.8$ and is true for both long and short seals. For speeds greater than 7000 RPM, the out-of-phase force is destabilizing. For lower speeds the force is stabilizing. As the incoming preswirl velocity is increased, the cross-over point occurs at a lower speed for the

TABLE 4

INFLUENCE OF GEOMETRIC CHANGES ON
 K_{12} AND C_{11} FOR A THIRTY
 CHAMBER HALF LABYRINTH

Parameters Changed	$C_{IN} = .8u$		$C_{IN} = .36u$		$C_{IN} = 0$	
	K_{12}	C_{11}	K_{12}	C_{11}	K_{12}	C_{11}
Base	13400	193	78200	194	28800	200
Clearance	152000	197	78900	196	10400	198
Chamber Hgt	56900	60	25100	61	-2600	64
Pitch	156000	173	72200	173	-8900	181
No. of Chambers	127000	134	53100	132	-13000	135
Radius	88100	94	44900	94	5920	97
Finish	115000	111	45200	112	-17700	111

$$\omega = 261.8 \text{ rad/sec}$$

<u>Parameter</u>	<u>Original</u>	<u>Modified</u>
Clearance	.010 in	.020 in
Height	.236 in	.334 in
Pitch	.197 in	.139 in
No. of Chambers	30	20
Radius	5.906 in	4.967 in
Finish	63×10^{-6} RMS in	0

long seal. With no preswirl, the long seal generally has a stabilizing effect over most of the speed range. Between 1300 and 3250 RPM, there is a slight destabilizing force in a negative whirl direction.

The short seal follows the same trend for preswirl velocities equal to .8u and .36u. With no preswirl, the out-of-phase force is destabilizing for negative whirl for speeds greater than 1300 RPM.

Another effect which was originally addressed by Alford was the influence of converging/diverging clearance on stability. From his initial analysis, he concluded that converging seals would destabilize the rotor system in a forward whirl direction. Diverging seals would destabilize in a negative whirl direction. To confirm this theory, clearance for both long and short seal configurations were varied along the seal in a linear fashion from .0073 to .0145 inches radially. For this change, both seals would pass the same leakage flow as passed for the constant clearance configurations. The results for both the 30 chamber case and 3 chamber case are shown in Tables 7 and 8 respectively. The trends predicted by Alford are confirmed in both tables but not the absolute direction. As mentioned earlier, Alford predicted no out-of-phase force for constant clearance seals. Since this configuration does have an out-of-phase force, the effect of converging/diverging clearance can be thought of as being superposed on the constant

TABLE 5

INFLUENCE OF GEOMETRIC CHANGES ON

 K_{12} AND C_{11} FOR A THREE

CHAMBER HALF LABYRINTH

Each parameter changed to same value as shown in Table 4 except for number of chambers. For this case the number of chambers was reduced from 3 to 2.

Parameters Changed	$C_{in} = .8u$		$C_{in} = .36u$		$C_{in} = 0$	
	K_{12}	C_{11}	K_{12}	C_{11}	K_{12}	C_{11}
Base	55100	5.9	7400	17.8	-34200	27.4
Clearance	24200	6.6	4560	10.4	-11900	11.8
Chamber Hgt	49400	4.5	6360	10.2	-29300	14.8
Pitch	31900	2.7	5030	7.7	-18300	10.6
No. of Chambers	31500	2.4	4040	9.5	-19600	13.5
Radius	51300	4.1	10500	11.7	-24000	16.2
Finish	48000	2.9	7560	16.6	-26000	19.6

$$\omega = 261.8 \text{ rad/sec}$$

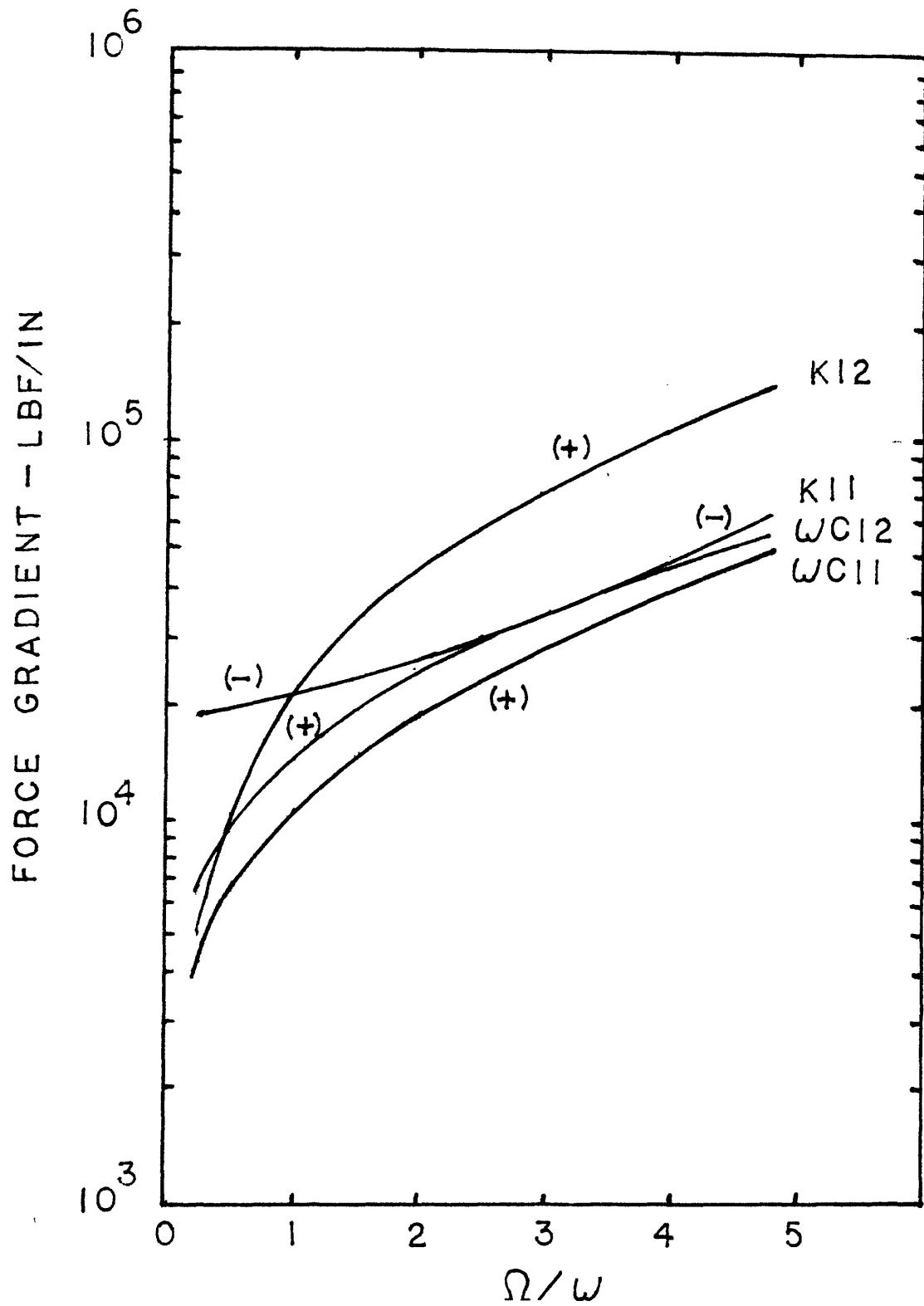


FIGURE 17 Displacement and whirl force gradients as a function of speed for Figure 16. Thirty chamber seal with preswirl equal to 80% of the rotor surface velocity.

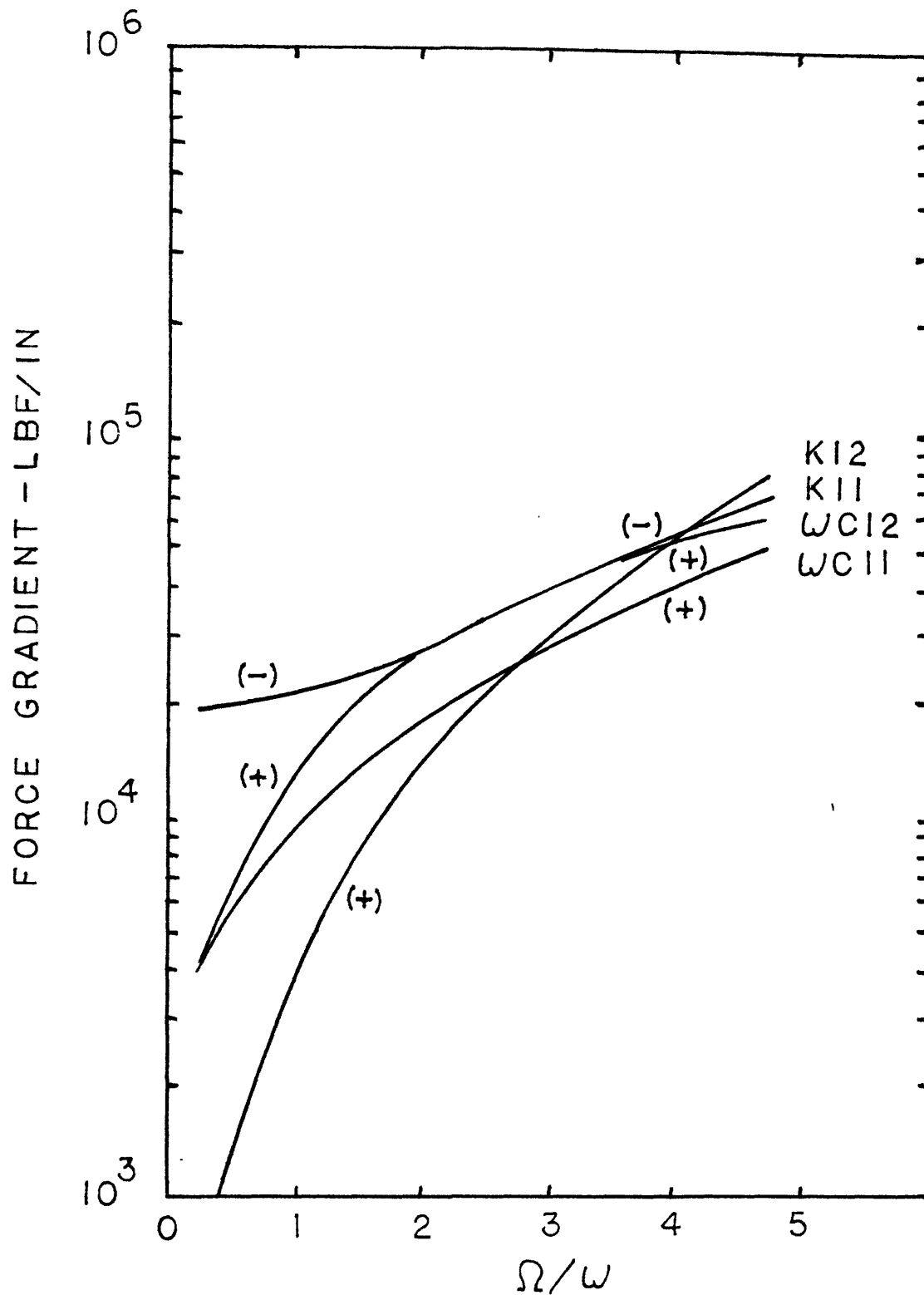


FIGURE 18 Displacement and whirl force gradients as a function of speed for Figure 16. Thirty chamber seal with preswirl equal to 36% of the rotor surface velocity.

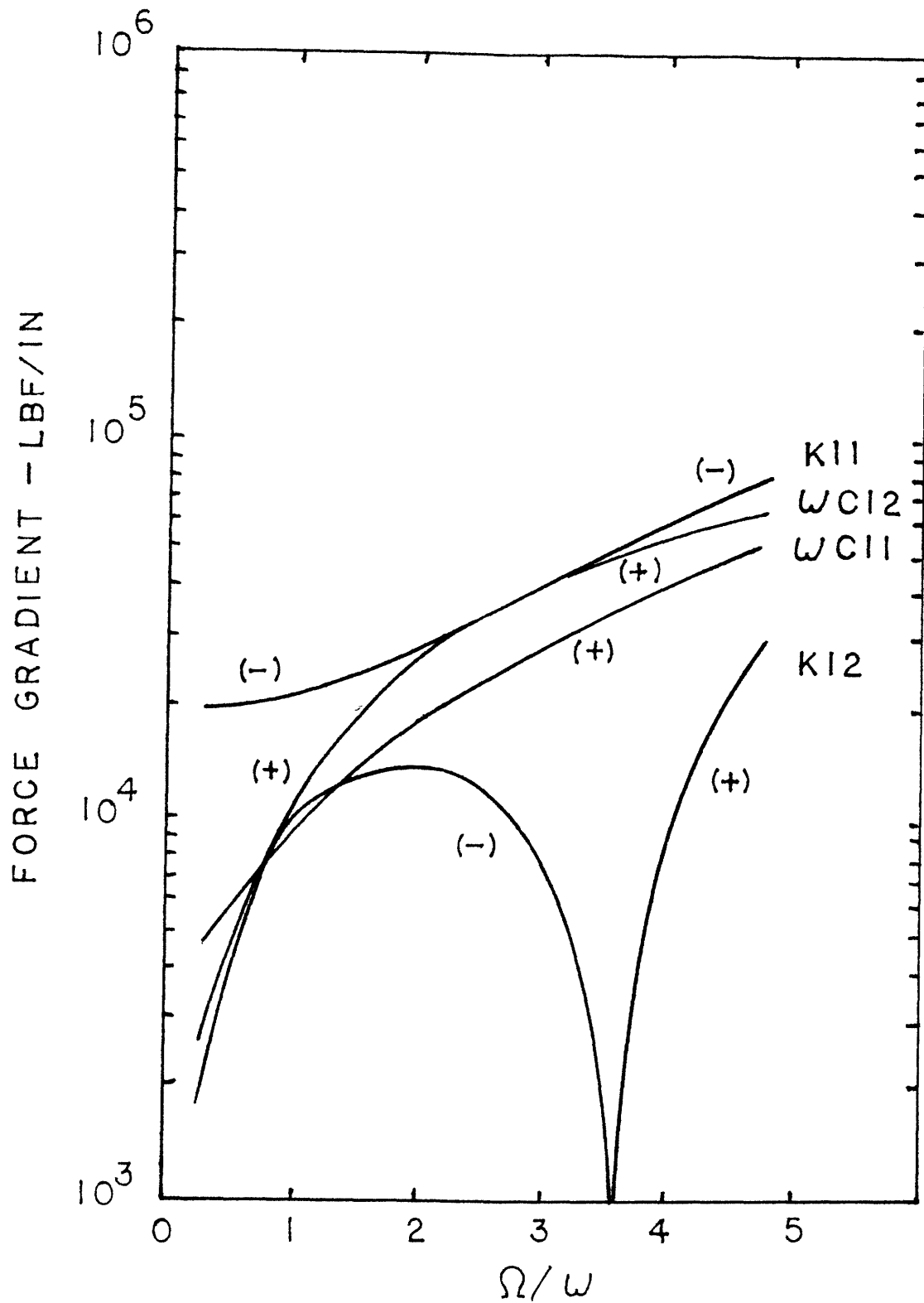


FIGURE 19 Displacement and whirl force gradients as a function of speed for Figure 16. Thirty chamber seal with no preswirl.

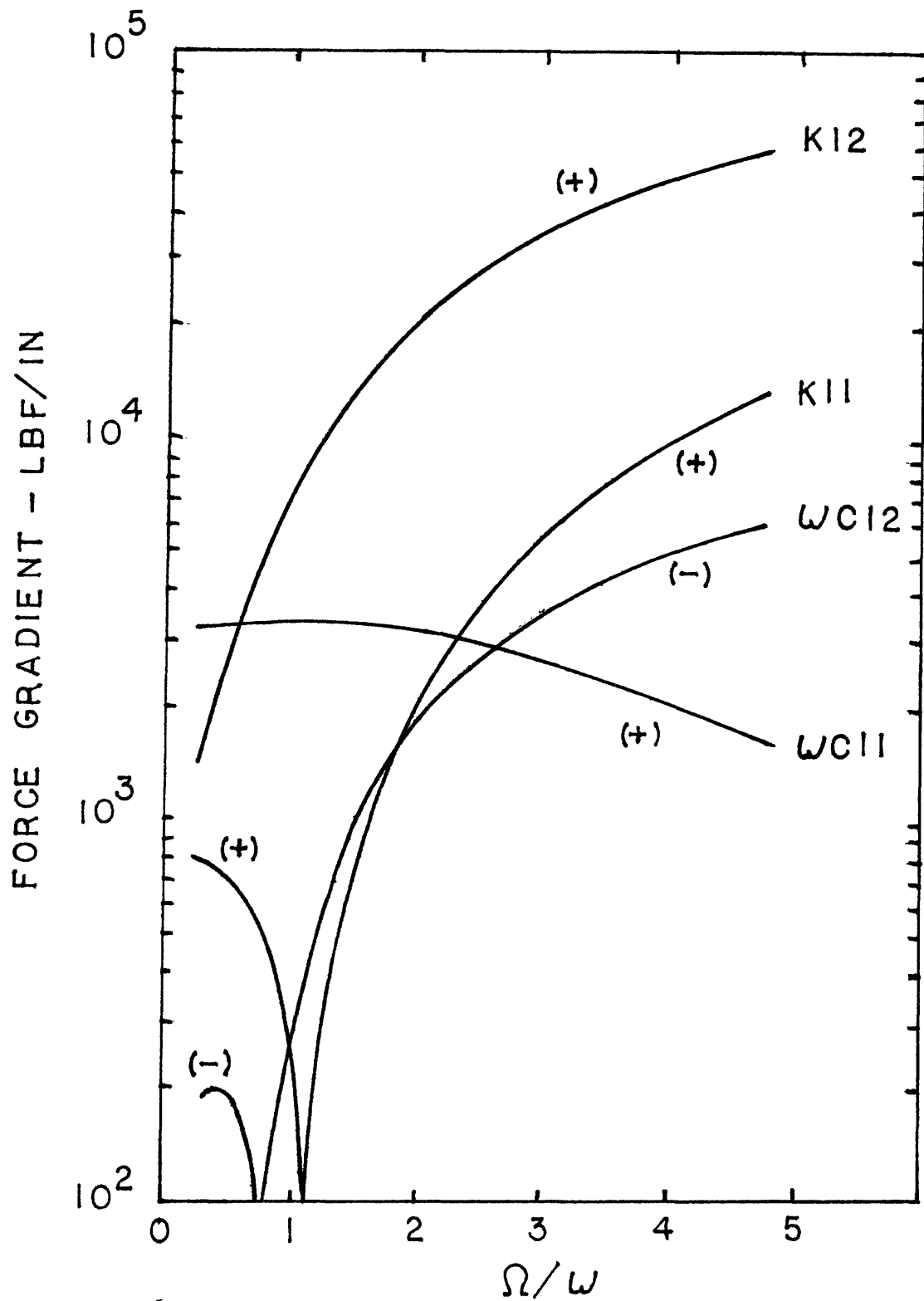


FIGURE 20 Displacement and whirl force gradients as a function of speed for Figure 16. Three chamber seal with preswirl equal to 80% of the rotor surface velocity.

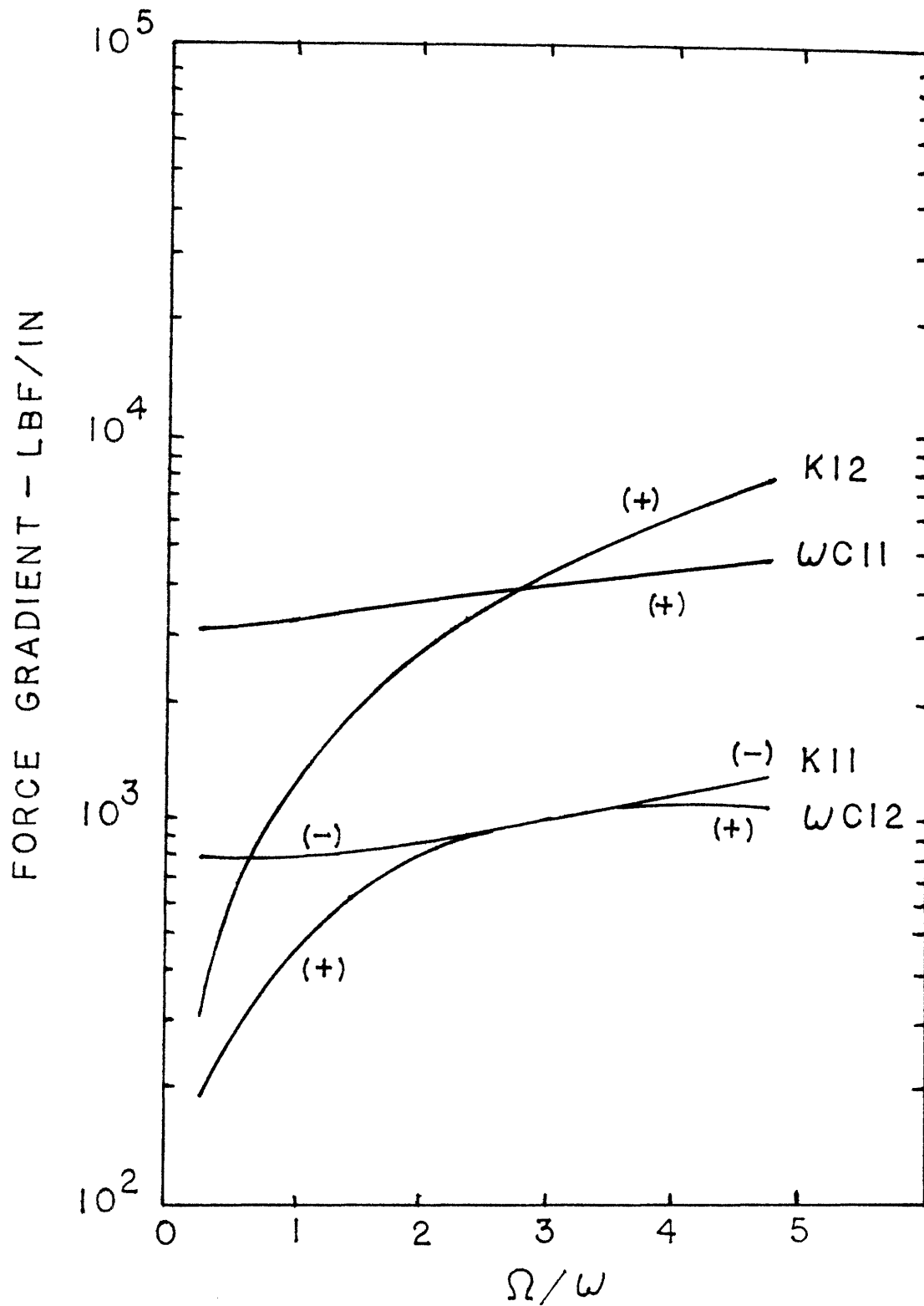


FIGURE 21 Displacement and whirl force gradients as a function of speed for Figure 16. Three chamber seal with preswirl equal to 36% of the rotor surface velocity.

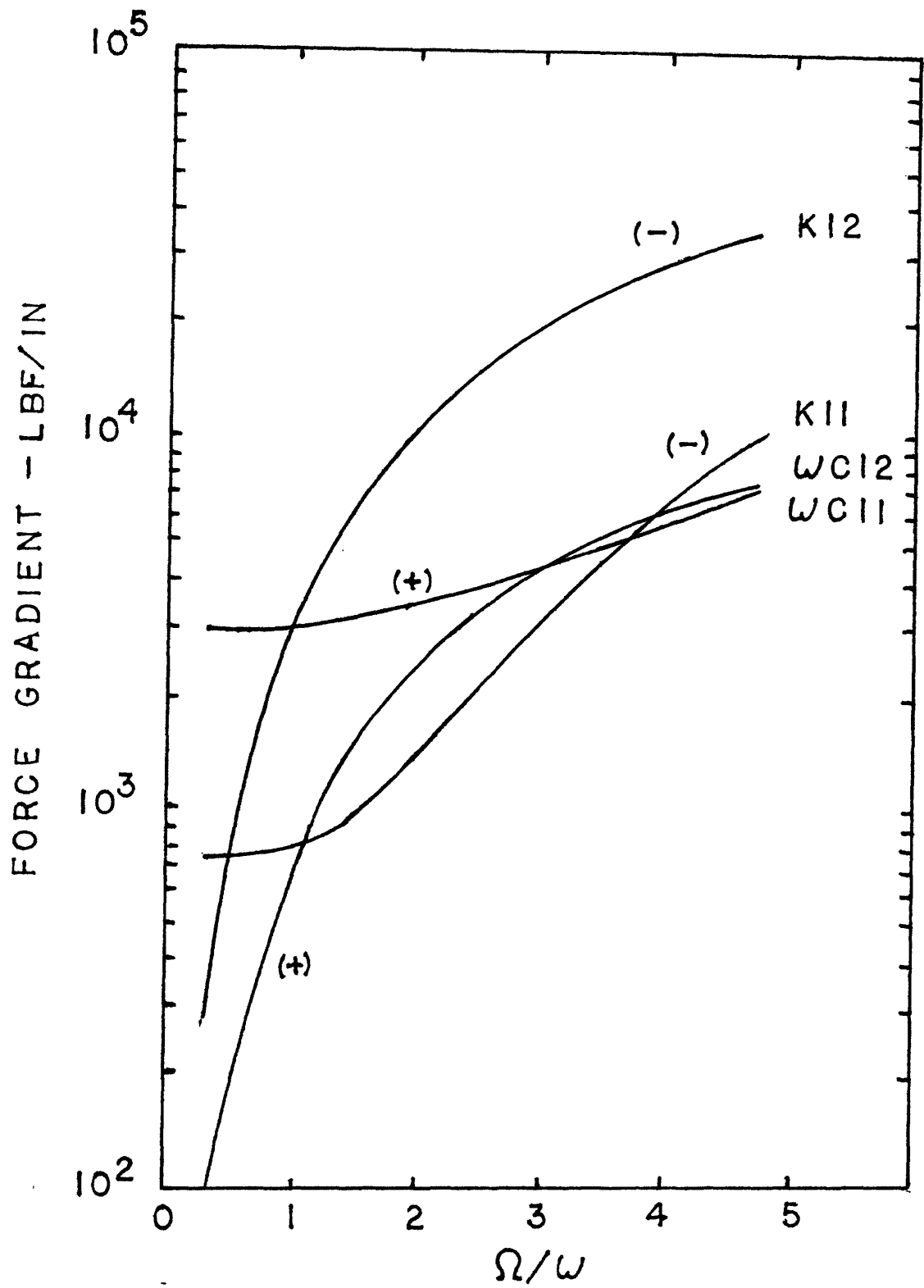


FIGURE 22 Displacement and whirl force gradients as a function of speed for Figure 16. Three chamber seal with no preswirl.

TABLE 6

EFFECT OF ROTOR SPEED AND
INLET SWIRL VELOCITY ON
HALF LABYRINTHS

<u>Thirty Chamber Seal Preswirl</u>	<u>Cross-Couple Force</u>
$c_{in} = .8u$	Always destabilizing (+) whirl
$c_{in} = .36u$	Above $\Omega/\omega = 2.80$ destabilizing (+) whirl
$c_{in} = 0$	Above $\Omega/\omega = 1.5$ stabilizing
<u>Three Chamber Seal Preswirl</u>	<u>Cross-Couple Force</u>
$c_{in} = .8u$	Above $\Omega/\omega = .6$ destabilizing (+) whirl
$c_{in} = .36u$	Above $\Omega/\omega = 2.8$ destabilizing (+) whirl
$c_{in} = 0$	Above $\Omega/\omega = 1.0$ stabilizing (-) whirl

clearance cross-coupling force. By subtracting the constant clearance values from the non-uniform clearance values, the change in out-of-phase force follows that predicted by Alford. The change in out-of-phase force levels for different preswirl velocities still follow the trend outlined for constant clearance configurations.

3.4 Closed Form Expressions

The effect of various parameters can be understood through closed form expressions. To obtain expressions for the cross-coupling force, two seal types will be examined. The first seal will be a very long, multichamber seal and the second a single chamber seal. These expressions will further be restricted to seals where each seal strip is identical with respect to flow characteristics and radial clearance.

To obtain a closed form expression for the out-of-phase force in long seals, the equations governing continuity and momentum given in Section 2 must be simplified. This can be accomplished by assuming the following:

1. $\phi_{pi} = \phi_{pi+1}$.
2. $\phi_{ci} = \phi_{ci+1}$.
3. $|\phi_{ci} - \phi_{pi}| = 90^\circ$.

TABLE 7
 CONVERGING AND DIVERGING SEAL
 COEFFICIENTS FOR A THIRTY CHAMBER SEAL

	K ₁₁	K ₁₂	C ₁₁	C ₁₂	Out-of-Phase Force Gradient-lbf/in
Converging δ					
c = .8u	-11800	161000	299	219	82722 (D) (+)
c = .36u	-13800	124000	302	229	44937 (D) (+)
c = 0	-19800	918000	310	233	10642 (D) (+)
Constant δ					
c = .8u	-63100	134000	193	214	83473 (D) (+)
c = .36	-68400	782000	194	230	27411 (D) (+)
c = 0	-76200	288000	200	242	-23560 (S) (+)
Diverging δ					
c = .8u	-107000	113000	83	199	91271 (D) (+)
c = .36u	-115000	29700	79	221	90186 (D) (+)
c = 0	-123000	-43800	81	240	22594 (D) (-)

δ_{\min} = .0073 in
 $\delta_{\text{const.}}$ = .010 in
 δ_{\max} = .0145 in
 (D) - Destabilizing
 (S) - Stabilizing
 (+) - Forward Whirl
 (-) - Negative Whirl

TABLE 8

CONVERGING AND DIVERGING SEAL
COEFFICIENTS FOR A THREE CHAMBER SEAL

	K_{11}	K_{12}	C_{11}	C_{12}	Out-of-Phase Force Force-lbs/in
Converging δ					
$c = .8u$	77500	59000	15	-38	55473 (D) (+)
$c = .36u$	62200	13800	30	- 9	5946 (D) (+)
$c = 0$	48500	-25900	47	15	-13595 (D) (-)
Constant δ					
$c = .8u$	12900	55300	6	-22	53729 (D) (+)
$c = .36u$	-1240	7400	18	4	2688 (D) (+)
$c = 0$	-9930	-34200	27	28	-27131 (S) (-)
Diverging δ					
$c = .8u$	-54500	46000	- 7	- 5	47833 (D) (+)
$c = .36u$	-65400	- 1520	0	18	-1520 (D) (-)
$c = 0$	-67700	-41800	1	39	-41538 (D) (-)

δ_{\min} = .0073 in
 $\delta_{\text{const.}}$ = .010 in
 δ_{\max} = .0145 in
(D) - Destabilizing
(S) - Stabilizing
(+) - Forward Whirl
(-) - Negative Whirl

$$4. \quad \bar{c}_i = c_{i+1} = \bar{c}_{eq}.$$

5. Incompressible flow.

The flow is assumed to have reached its equilibrium circumferential velocity. One would also expect very little phase shift between adjacent chambers for either pressure or tangential velocity. Intuitively, the point of maximum velocity should occur at the point of minimum chamber area. (See Figure 23.) This is different from what was shown in Figure 10 for the 3 chamber seal. This will be discussed for the single chamber seal. For the force to influence stability, it must either lead or lag the eccentricity of the rotor by 90°.

The continuity equation in its original form is

$$\frac{\partial}{\partial t} (\rho_i f_i) + \frac{\partial}{\partial x} (\rho_i c_i f_i) + q_{i+1} - q_i = 0. \quad (72)$$

Since it was assumed that no phase shift in pressure exists between adjacent chambers,

$$q_{i+1} = q_i = 0. \quad (73)$$

at all points around the seal. Using the other simplifications, equation (85) becomes

$$\frac{\dot{f}_i}{\bar{c}_i \bar{f}_i} + \frac{f_i'}{\bar{f}} + \frac{c_i'}{\bar{c}_i} = 0. \quad (74)$$

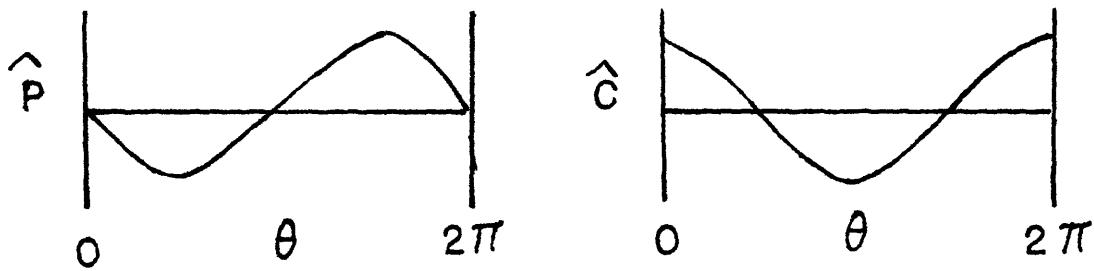
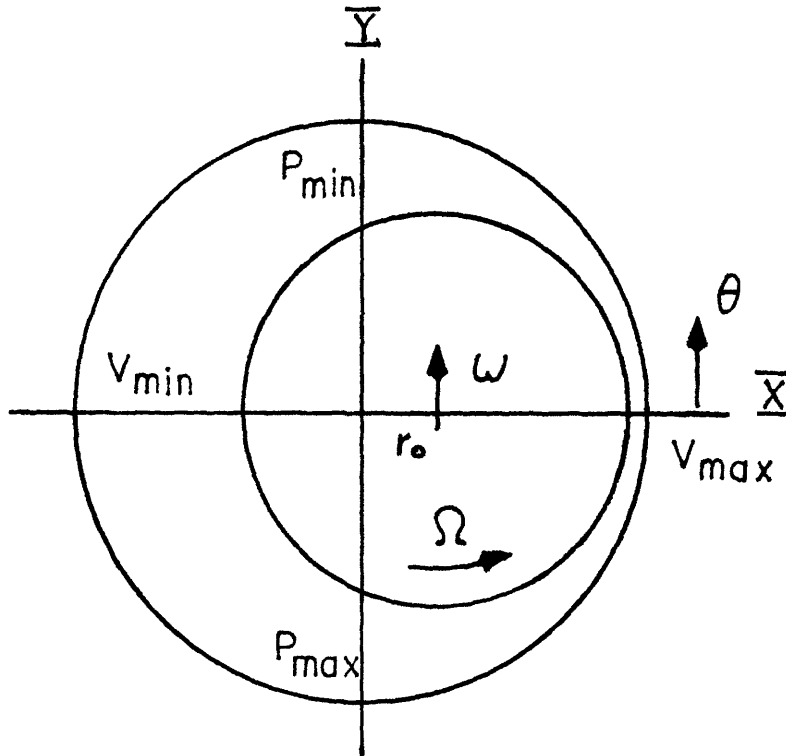
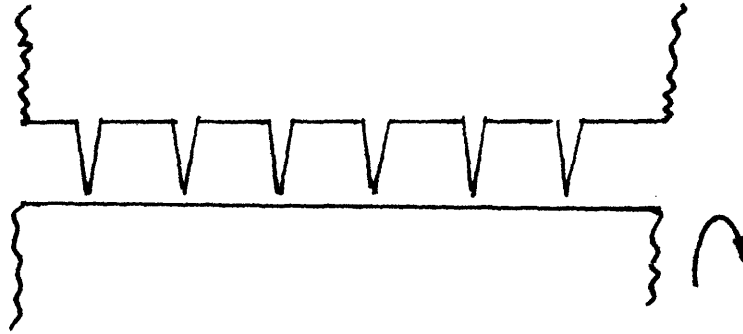


FIGURE 23 Schematic of pressure and velocity distribution for a very long, multichamber seal.

The momentum equation in its complete form is

$$\begin{aligned} \frac{\partial}{\partial t} (\rho_i c_i f_i) + \frac{\partial}{\partial x} (\rho_i c_i^2 f_i) + f_i \frac{\partial}{\partial x} P_i \\ + \tau_{Si} S_{Si} - \tau_{Ri} S_{Ri} + q_{i+1} c_i - q_i c_{i-1} = 0. \end{aligned} \quad (75)$$

This can be simplified to the following:

$$\bar{f}_i \frac{\partial P_i}{\partial x} + \tau_{Si} S_{Si} - \tau_{Ri} S_{Ri} = 0. \quad (76)$$

The terms which contribute to forces in-phase with the rotor eccentricity were neglected. The simplifications will be justified by comparing the percentage change in the out-of-phase force as calculated by the complete theory with those from the simplified expressions.

The simplified expressions for pressure and tangential velocity are

$$P_i = \bar{P}_i - P_{mi} \sin \left(\frac{x}{R} - \omega t \right) \quad (77)$$

and

$$c_i = \bar{c}_i + c_{mi} \cos \left(\frac{x}{R} - \omega t \right). \quad (78)$$

By combining equations (15), (16), (30), (31), (74) and (76) with (77) and (78), the following relationships for pressure and tangential velocity result:

$$P_i = \bar{P}_i - \frac{1}{f^2} \rho R^3 \left[\lambda_S S_S \frac{\bar{c}_i}{R} + \lambda_R S_R \left(\frac{u - \bar{c}_i}{R} \right) \right] \left(\frac{\bar{c}_i}{R} - \omega \right) r_0 \sin \left(\frac{x}{R} - \omega t \right) \quad (79)$$

and

$$c_i = \bar{c}_i + \left(\frac{\bar{c}_i}{R} - \omega \right) \frac{R \ell}{f} r_0 \cos \left(\frac{x}{R} - \omega t \right) . \quad (80)$$

Integrating the pressure distribution around the *i*th chamber and summing all chambers gives the following stiffness and damping expressions:

$$K_{12} = \sum \frac{M}{R} \frac{\bar{c}_i}{R} \ell^2 \frac{\rho_i R^4}{f^2} \pi \left(\lambda_{Si} S_{Si} \frac{\bar{c}_i}{R} + \lambda_R S_R \frac{u - \bar{c}_i}{R} \right) \quad (81)$$

and

$$C_{11} = \sum \frac{M}{f^2} \frac{\ell^2 \rho_i R^4 \pi}{f^2} \left(\lambda_{Si} S_S \frac{\bar{c}_i}{R} + \lambda_R S_R \frac{u - \bar{c}_i}{R} \right) . \quad (82)$$

Since the tangential velocity is at its equilibrium value and if each chamber has identical geometry, then only the density changes significantly in the summation. The equilibrium velocity is found from equation (76) by letting $c_i = c_{i-1}$

and equating the surface drag forces on both stationary and rotating surfaces. The resulting tangential velocity is

$$c_{eq} = \frac{u}{1 + \frac{\sqrt{\lambda_s S_s}}{\lambda_R S_R}} \quad (83)$$

To understand how the seal forces act on the rotor, the shaft will be displaced and whirled in a circular orbit. (See Figure 17.) At the initial point, $t = 0$, the out-of-phase force on the rotor is

$$\underline{F}_Y = - (k_{21} + \omega C_{11}) r_o \quad (84)$$

Substituting equation (81) and (82) into the above expression gives

$$\underline{F}_Y = - \frac{l^2 R^4 \pi}{f^2} \left(\lambda_s S_s \frac{\bar{c}_{eq}}{R} + \lambda_R S_R \frac{u - \bar{c}_{eq}}{R} \right) \cdot$$

$$\int^M \rho_i \left(\omega - \frac{c_{eq}}{R} \right) r_o \quad (85)$$

From the symmetry of the system, equation (85) is the out-of-phase force at all circumferential locations. The stabilizing or destabilizing effect of the out-of-phase force on the rotor is determined by the relative magnitudes of the damped natural frequency and the angular velocity of the chamber fluid, c_{eq}/R . When the rotor is orbiting in the same sense and faster than the fluid is moving tangentially, the net

out-of-phase force opposes the motion of the shaft. It acts to stabilize the system. When c_{eq}/R is greater than ω , the shaft is dragged by the fluid. This tends to push the rotor in a forward whirl direction and reduces the overall stability. When the two angular velocities are equal, no out-of-phase force is experienced by the rotor. Since the value of c_{eq} is a function of the rotor speed, the cross-over point occurs when

$$\frac{\Omega_{\text{cross-over}}}{\omega} = 1 + \sqrt{\frac{\lambda_S S_S}{\lambda_R S_R}} \quad (86)$$

For typical labyrinth seal designs, this ratio is between 2.0 for full labyrinths and 2.8 for half labyrinth designs. This ratio provides a rough rule of thumb to determine the speed above which seal related instabilities may be experienced. For this to apply, there must not be an appreciable difference between the inlet preswirl velocity and the equilibrium tangential velocity.

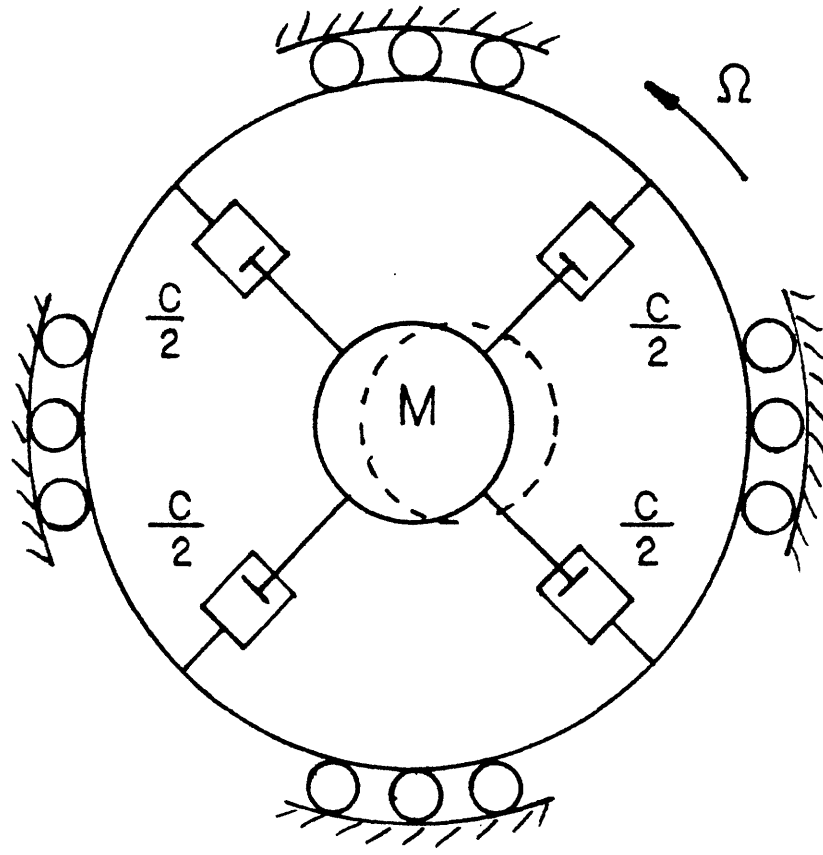
S. H. Crandall presented, in references 9 and 10, a clear, physical explanation on the destabilizing force from damping in rotating parts. His model, shown in Figure 24, consisted of a point mass surrounded by a circularly uniform rotating dash-pot system in a circular orbit. He demonstrated that for a system rotating subcritically, $\Omega < \omega$, the damping force opposes the motion of the mass for both forward and backward whirls. For supercritical rotation, $\Omega > \omega$, the damping force

pushes the point mass in the direction of forward whirl. This has a destabilizing effect. The rotating dashpots do work on the rotor because for counterclockwise whirl, the relative motion of the mass is backward at a rate $\Omega - \omega$. The force acting in the direction of motion is $cr_0 (\Omega - \omega)$ and tends to drag the rotor in forward whirl.

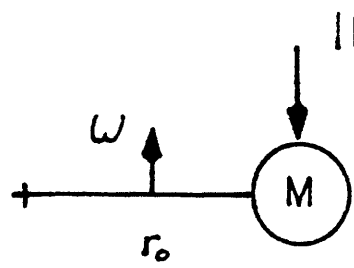
Crandall extended the argument to the case of oil whip in lightly loaded, cylindrical bearings. Here, the dashpots are replaced by a traveling oil film pressure wave generated by the rotor moving in a small orbit. The fluid is pumped by the rotating shaft and produces frictional drag forces on the contacting surfaces. Since a linear velocity distribution was assumed, the mean velocity of the film is one-half the rotation speed. The traveling pressure wave argument was applied giving a stabilizing/destabilizing cross-over point to be

$$\left(\frac{\Omega \text{ cross-over}}{\omega} \right)_{\text{oil whip}} = 2.$$

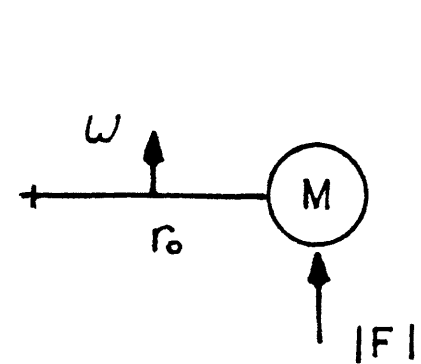
This is the same value predicted by equation (86) for a full labyrinth seal. In this regard, the concept of a traveling pressure wave provides the physical insight to the destabilizing force and its relative strength as a function of rotational speed. By simply knowing the mean angular velocity of a fluid and comparing it to the natural frequency of the system, a judgment can be made on its effect on system stability.



CIRCULAR ORBIT OF FREQUENCY ω AND RADIUS r_0



Subcritical Rotation



Supercritical Rotation

FIGURE 24 Demonstration of destabilizing force with rotating damping model.

As the number of chambers in the seal model is reduced, the role of friction changes. As will be shown, the out-of-phase force is no longer dominated by frictional drag, but by the change in tangential velocity from friction as the gas passes through the seal.

To demonstrate this, consider a seal with only one chamber as shown in Figure 25. The chamber flow is again allowed to have a variation in pressure and tangential velocity similar in form to that used in long seals. Again, based on the 3 chamber seal example, the point of maximum tangential velocity is assumed to be 90° away from the maximum pressure location. Unlike the seal strips in very long, multichamber seals, both teeth in the single chamber seal see a pressure variation in the chamber and constant, uniform pressure on the outside. This variation in pressure has the effect of locally passing flow either into or out of the chamber. This is shown in Figure 26. Qualitatively, where the pressure is locally high relative to the mean, more leakage flow will pass out of the chamber than will enter. At the minimum chamber pressure, the opposite is true.

This variation in net flow acts as a gradient on the tangential chamber velocity. The tangential velocity will tend to increase in the half where the local pressure is below the mean chamber value. The velocity will reach a maximum at a point 90° from the maximum pressure point and on the side of increasing chamber pressure. The tangential velocity is also influ-

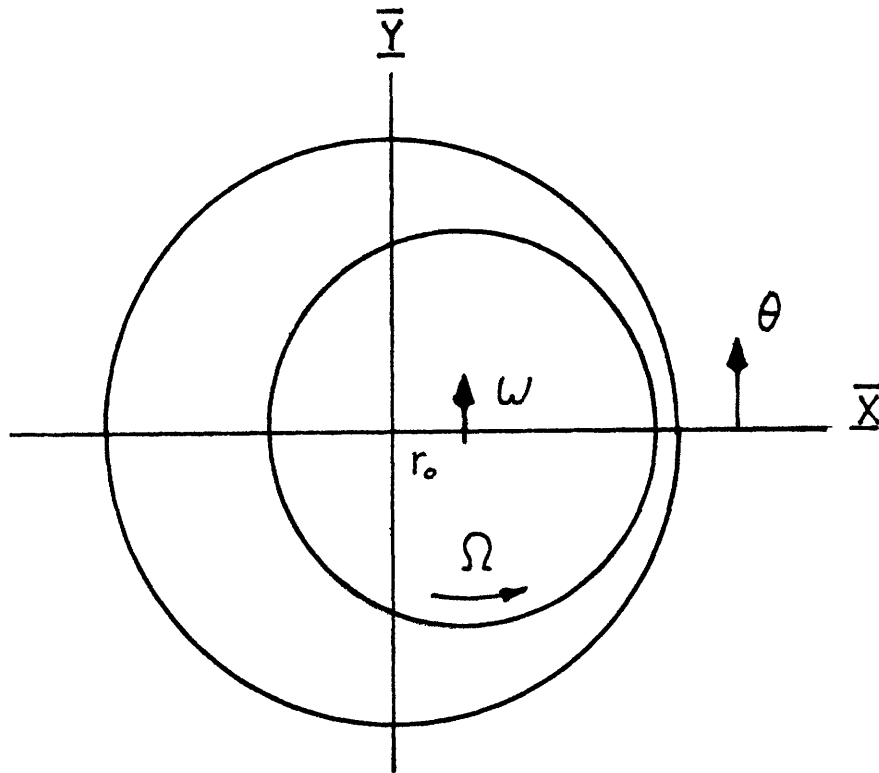
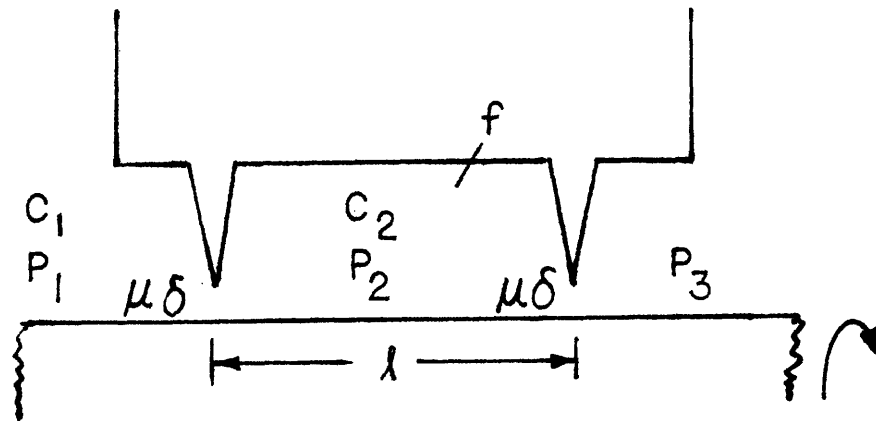


FIGURE 25 Configuration for single chamber seal with shaft whirl.

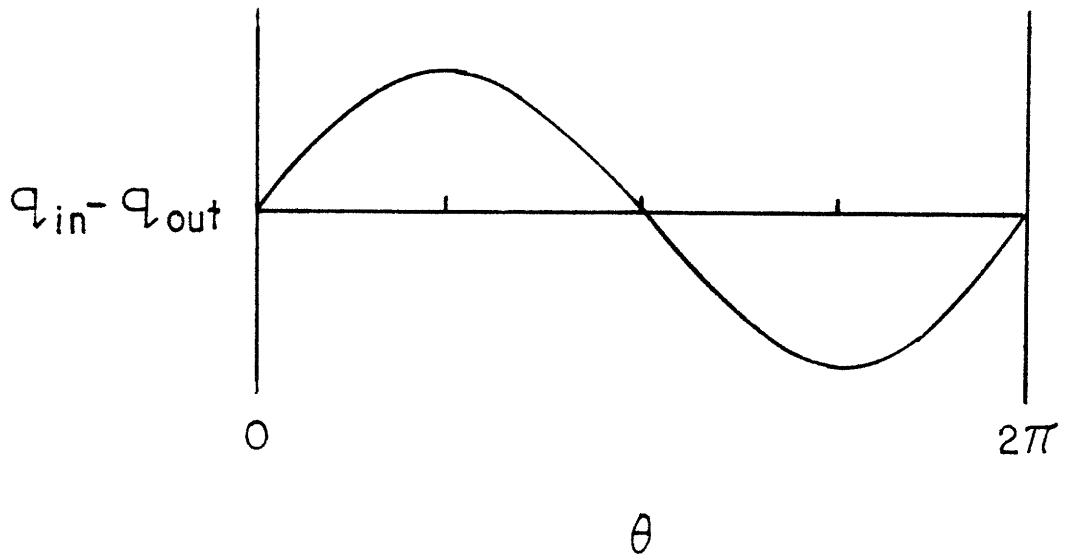
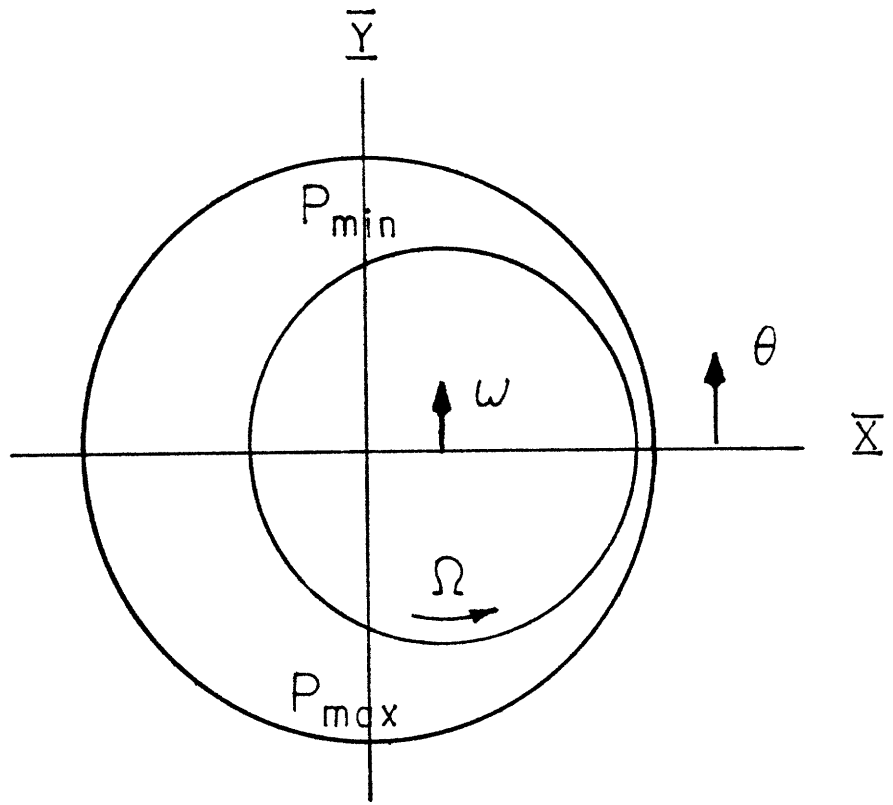


FIGURE 26 Pressure and leakage flow variation for a single chamber seal.

enced by the change in chamber area. If the maximum pressure occurs at a point lagging the rotor center by 90°, then the two effects on velocity oppose each other. (See Figure 27). For the initial comparison made with the Benckert and Wachter data, Figure 11, the influence of leakage flow dominates the factors in establishing the velocity distribution. The cross-coupling force is dependent on the momentum change in the swirl velocity through the seal. This part of the momentum change comes from local variation in tangential velocity. Since the local velocity is now dependent on local leakage flow, it would be expected that clearance has a major influence on the out-of-phase force. This was not a factor in long seals because the phase relationships for pressure on either side of a seal strip are very close to each other. Therefore, very little variation of local net flow into each chamber existed.

To arrive at closed form expressions for chamber pressure in the single chamber seal, both equations for continuity and momentum must again be simplified. The same assumptions are used again except that locally net flow into or out of the chamber is permitted. The differential equation for continuity becomes

$$\frac{\dot{f}}{c f} + \frac{c'}{c} + \frac{f'}{f} + \frac{\hat{q}_3 - \hat{q}_2}{\rho c f} = 0. \quad (87)$$

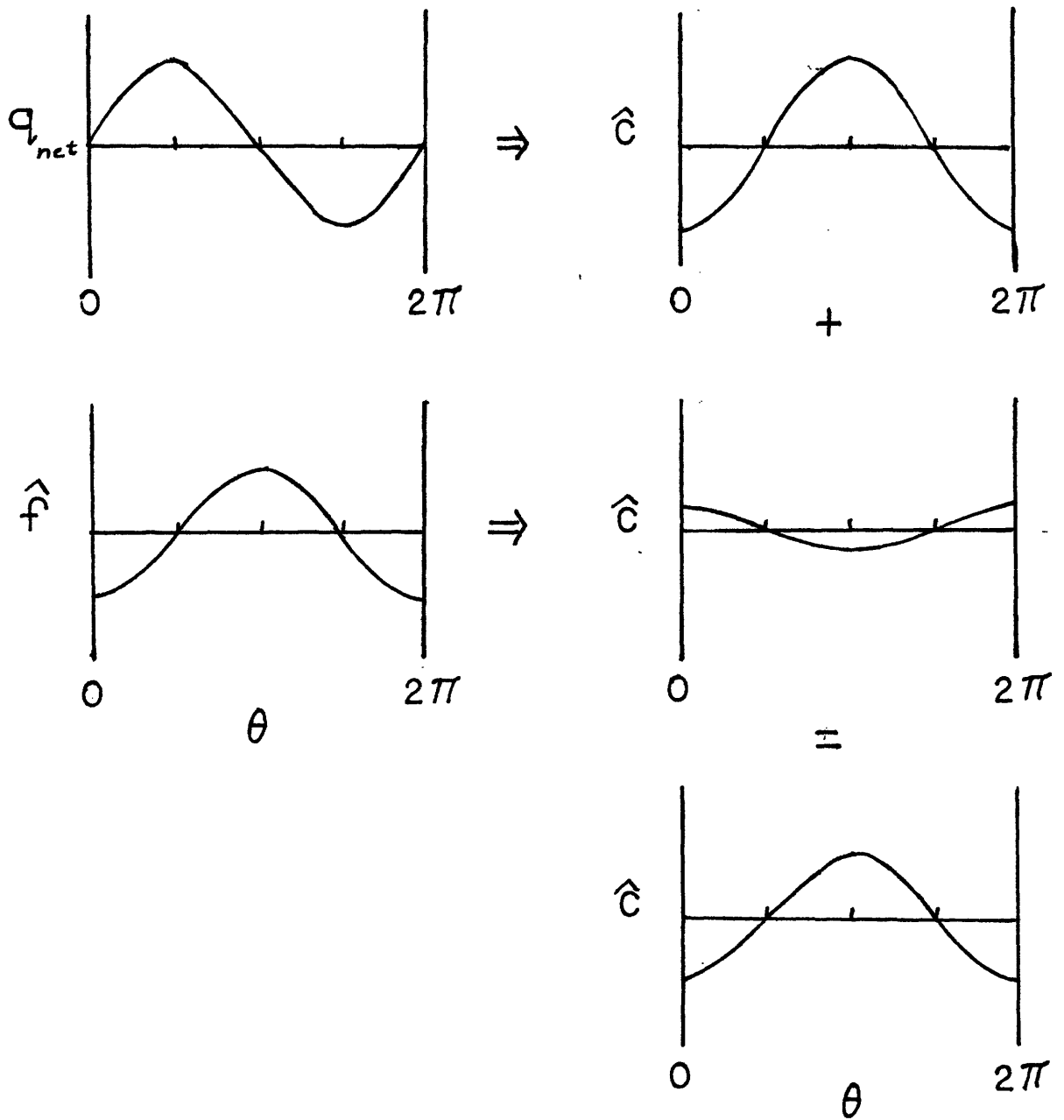


FIGURE 27 Tangential velocity distribution in a single chamber seal.

Since the tangential velocity is expected to change as the flow passes through the seal, the momentum and flux terms must be retained. Assuming the maximum pressure occurs 90° away from the rotor center, the momentum equation can be simplified to

$$\bar{f} P_2' + \beta_{qf} \hat{c}_2 = \bar{q} (c_1 - c_2) \frac{\hat{\delta}}{\delta} \quad (88)$$

where

$$\beta_{qf} = q + \rho \lambda_S S_S \bar{c}_2 + \rho \lambda_R S_R (u - \bar{c}_2)$$

Using the same simplified expressions for pressure, (77), and tangential velocity, (78), the zero to peak pressure variation can be expressed as

$$P_{m2} = \frac{\frac{r_o l}{f} \left(1 - \frac{\omega R}{c_2} \right) + \frac{q}{c_2} (\bar{c}_1 - \bar{c}_2) \frac{r_o}{\delta}}{\frac{q R P_r}{\rho_2 \bar{c}_2 \bar{f}_2 \bar{P}_2} + \frac{\bar{f}}{c_2 R \beta_{qf}}} \quad (89)$$

where

$$P_r = \frac{1}{\left(\frac{P_1}{P_2} \right)^2 - 1} + \frac{1}{1 - \left(\frac{P_2}{P_3} \right)^2}$$

By integrating the chamber pressure around the seal, the net force experienced by the rotor for a circular orbit is

$$\begin{aligned}
F \bar{Y} &= -(K_{21} + \omega C_{22}) r_o \\
&= \frac{\ell R \pi \bar{P}_2}{\frac{\bar{q} R P_r}{\rho_2 \bar{c}_2 \bar{f}} + \frac{\bar{P}_2 \bar{f}}{\beta_{qf} \bar{c}_2 R}} \cdot \left[\frac{\bar{q}}{\beta_{qf}} \left(\frac{\bar{c}_1}{\bar{c}_2} - 1 \right) \frac{1}{\delta} \right. \\
&\quad \left. + \frac{\ell}{\bar{f}} \left(1 - \frac{R \omega}{\bar{c}_2} \right) \right] . \tag{90}
\end{aligned}$$

The direction of the out-of-phase force on the rotor is influenced by the change in tangential velocity of the leakage flow and, as with long seals, by the ratio of tangential angular velocity to precession angular velocity. If the incoming tangential velocity is very large, the change in tangential momentum dominates the forces created by chamber area variations. For this condition, the destabilizing force can be in a direction to excite either the forward whirl, $c_1 \gg c_2$, or the backward whirl, $c_1 \ll c_2$. If the leakage flow enters at the equilibrium value c_{eq} , then the crossover point between a stabilizing force and a destabilizing one follows equation (86). For other values of c_1 , the crossover point occurs when the numerator of (90) goes to zero. It is a function of clearance, pressure, friction factors and seal geometry as well as precession angular velocity.

Actual labyrinth designs must fall somewhere between the extreme case of a very long, multichamber seal and that of a single chamber seal. The trends for both cases must be present

to a greater or lesser degree in all designs. By studying the closed form approximations of the two limiting cases, a designer can determine what parameters are of importance and qualitatively how much they must be changed to achieve a desired seal force level. For example, from equation (85), the cross-coupling force for long, multichamber seals is proportional to the following parameters:

1. Inversely proportional to the square of the average chamber height, $(f/l)^2$.
2. Number of seal chambers.
3. Fluid density.
4. Friction factor of the chamber surface.
5. Seal radius to the fourth power.
6. The difference between the angular velocity of the chamber fluid and the natural frequency of the rotor system excited.

The expression for the single chamber seal, (90), is still sufficiently complicated to prevent describing simple relationships between force and the parameters. If it is assumed that

the force is dominated by the contribution from the change in tangential velocity,

$$\left(c_1 - c_2 \right) \frac{1}{\delta} \gg \frac{l}{f} \left(c_2 - R \omega \right),$$

then depending on the geometry and flow conditions the following can be said:

1. As the clearance decreases, cross-coupling force increases.
2. The out-of-phase force will generally increase as the shaft radius increases.
3. Large increases in the average chamber height, f/l , will decrease the cross-coupling force. Small changes can either increase or decrease the force depending on other parameters.
4. The greater the incoming swirl velocity, the greater the destabilizing force will be in the direction of positive whirl. If the tangential velocity increases substantially while passing through the seal, the force is destabilizing in a negative whirl direction.

How the out-of-phase force changes with parameter changes is dependent on the actual seal geometry and flow conditions. This might explain why many investigators arrive at different

conclusions on the importance of seal geometry and leakage flow conditions. Most experimental investigations were made with seal geometries that combine the effects of both long and short seals. The results from scaled tests are then extrapolated to actual turbomachinery conditions. The predicted results may not always be achieved. This is particularly true in the case of Wright who attempted to extrapolate tests on a single chamber seal to all turbomachinery seals. The same is true of closed form expressions that have been published and are used for all geometries and flow conditions encountered in actual designs. For the conditions assumed, the expression may adequately predict the seal force but may fail miserably at other conditions. The two closed form expressions do identify how changes in seal geometry will change the magnitude of the out-of-phase force for specific conditions. The accuracy of the predicted change will vary depending on how well a particular design matches the two extreme cases. This can easily be seen by comparing the expected changes in coefficients as predicted by equations (85) and (90) with the values given in Tables 4 and 5.

IV. IMPACT ON TURBOMACHINERY DESIGN AND OPERATION ON STABILITY

So far, the discussion has centered on the prediction of forces generated by an eccentric rotor in a labyrinth seal. The goal of this analysis is to incorporate the seal effect into the total rotor system and more accurately predict changes in rotor stability at all anticipated speeds and loads on the machine. The incentive for this is quite high. For example, many turbomachines are used in the production of petrochemicals and fertilizers. These machines are typically high speed, high pressure steam turbines which drive compressors. The first cost of these units is approximately 1 to 2 million dollars. In relation to the total cost of the plant the cost of the turbines and compressors is only a small fraction. Reliable operation of the turbomachinery is key to the plant supplying product as required. When these machines shut down from high, asynchronous vibration under load, no product is produced. Petrochemical plants may lose up to \$250,000 per day when this occurs. The cost of opening a machine, once the problem has been identified, can cost between \$35,000 and \$50,000. This does not include the cost for time lost in production. The total time lost can be from 6 to 14 days. If no alternative methods are available to make product, the losses can be as high as \$3.5 million dollars. There is no guarantee that the problem was correctly diagnosed. Typical fixes involve some change with respect to the journal bearings to get more damping into the system. An implemented fix may only partially work if the destabilizing forces are very high. The machinery may still not achieve the desired load condition. In such an event, plant

operators are faced with the dilemma of continued operation at a reduced output rate or attempting another solution and incurring more lost time. The manufacturer of the equipment also suffers losses in both prestige and possible future orders on similar types of equipment.

A thorough understanding of changes in machinery stability under load is clearly required. To accomplish this, knowledge of several things are necessary. The first requirement is being able to predict the response of the rotor system under no load. This can be accomplished by comparing the response of the machinery to unbalance as a function of speed. The once-per-revolution response of the rotor is generally measured with two eddy current probes spaced 90° apart near each bearing. A known unbalance is placed either at the rotor midspan location or at the coupling end depending on the shape of the mode to be excited. Such testing locates the critical speeds of the rotor and provides an indication of the amount of damping present in each response peak. The test information is then compared to calculated forced response vibration of the probe locations. Differences between the two sets of values are then resolved by improving the model of the system. These improvements are generally in the area of bearing stiffness and damping coefficients and bearing support stiffness, mass and damping values. Good agreement on the location of criticals and their amplification factors are required if the corresponding stability analysis is to be accurate.

The aero-elastic force gradients are then added to the analysis to predict changes in stability at various speeds and loads. Generally, manufacturers of turbomachinery rely on calculations to predict these changes. Full load factory testing, generally, is not feasible because of facility limitations and expense. Section 3 demonstrated that aero-elastic forces in test seals could be accurately predicted. The test conditions were precisely known for these cases. While temperatures and pressures can be predicted for different operating points, the preswirl velocity entering the seal is in doubt. As previously shown, the preswirl velocity has a significant effect on the destabilizing force generated. The common assumption of the preswirl value equal to one-half the rotor surface velocity is not always a good one. As will be seen, the preswirl entering a seal is affected by the performance of the machine at various design conditions, gas path geometry and surface friction.

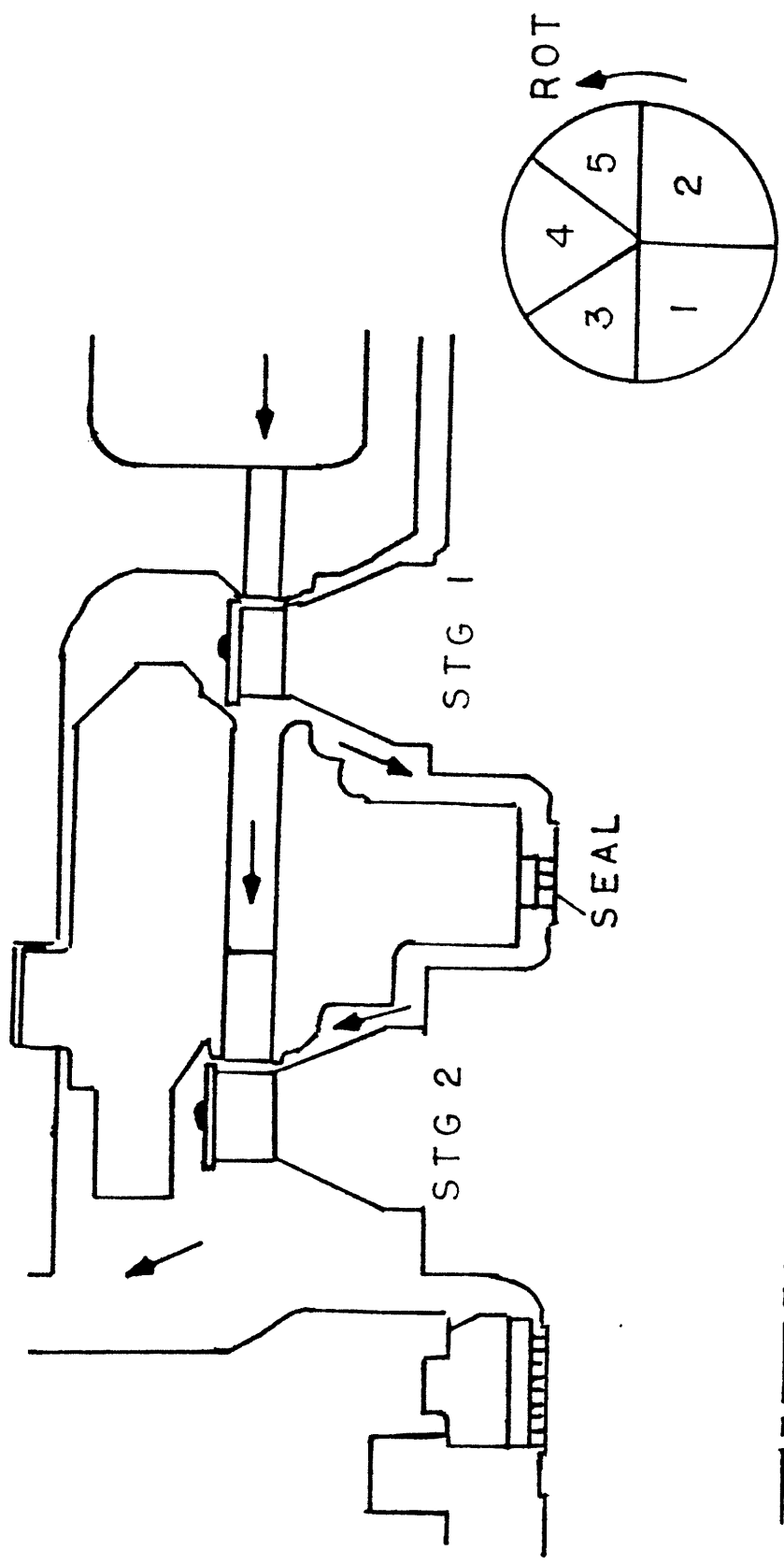
With each of the components of the rotor system analytically defined, the stability of the rotor system can be evaluated. For the conditions of interest, the logarithmic decrement is calculated for each mode of concern. The minimum log decrement value can be plotted in the form of a contour map. The two ordinates can be speed and shaft output. By displaying the log decrement values in this form, the design engineer quickly gets a feel of how the stability of the system will change for different operating conditions. This approach will be demonstrated on a simple high speed rotor. It will also be shown how to enlarge the stable operating

region and reduce the leakage losses with relatively minor changes in the seal design.

4.1 Operation at Variable Design Conditions

To demonstrate how the performance of a machine can influence the destabilizing forces from seals, a specific steam turbine design will be used. This two stage turbine, shown in Figure 29, is designed to operate between 8000 and 12,000 RPM and generates 8500 horsepower. It is used to drive a compressor at the design point of 10,500 RPM. The inlet temperature is 950°F and the inlet and exhaust pressures are 1450 and 560 PSIG respectively.

For improved part load efficiency, each of the five valves feeds a separate section of the total first stage nozzle plate. As shown in Figure 28, the first valve feeds the lower left quadrant of the nozzle plate. With the second valve sequentially opened, the entire lower half is fed. With all valves opened, the entire nozzle plate is fed with steam. A 3 chamber straight labyrinth seal controls the leakage between the first and second stages. The seal configuration is that shown in Figure 22 except for the radial tooth clearance. For this case a clearance of .020 inches will be used. The stiffness and damping coefficients for this seal will be calculated to demonstrate the influence of different operating conditions on the destabilizing force gradient.



ORDER OF
VALVE OPENING

FIGURE 28 Steam path and first stage steam admission for high speed compressor drive turbine.

From thermodynamic calculations the state of the steam and flow conditions are known for each valve point. For discussion purposes, the turbine will operate at a reduced efficiency off-design speed point of 12,000 RPM. The load of machine will be varied at this constant speed. This requires different valve settings to pass the required flow. Figure 29 shows how both upstream seal pressure and steam flow increase as the inlet valves are opened sequentially. The downstream seal pressure is held constant at 575 PSIA.

The effect of variable speed off-design operation is the swirl induced in the steam leaving the blades. This can be seen from the velocity diagram shown in Figure 30. The steam leaves the nozzle with a velocity V_1 at an angle α_N . The blade is traveling with a tangential velocity WB . Therefore, the blade sees the steam entering with a relative velocity of V_{1R} . For this impulse type design, the relative leaving velocity, V_{2R} , is slightly lower in magnitude than V_{1R} . By adding in the blade speed, the absolute velocity of the steam leaving the blade is V_2 . For maximum efficiency, V_2 should have no tangential component. Figure 31 shows the velocity diagrams for the 3rd and 5th valve points. As the number of valves open increases, the blade becomes less efficient and more swirl is given to the steam leaving the blade.

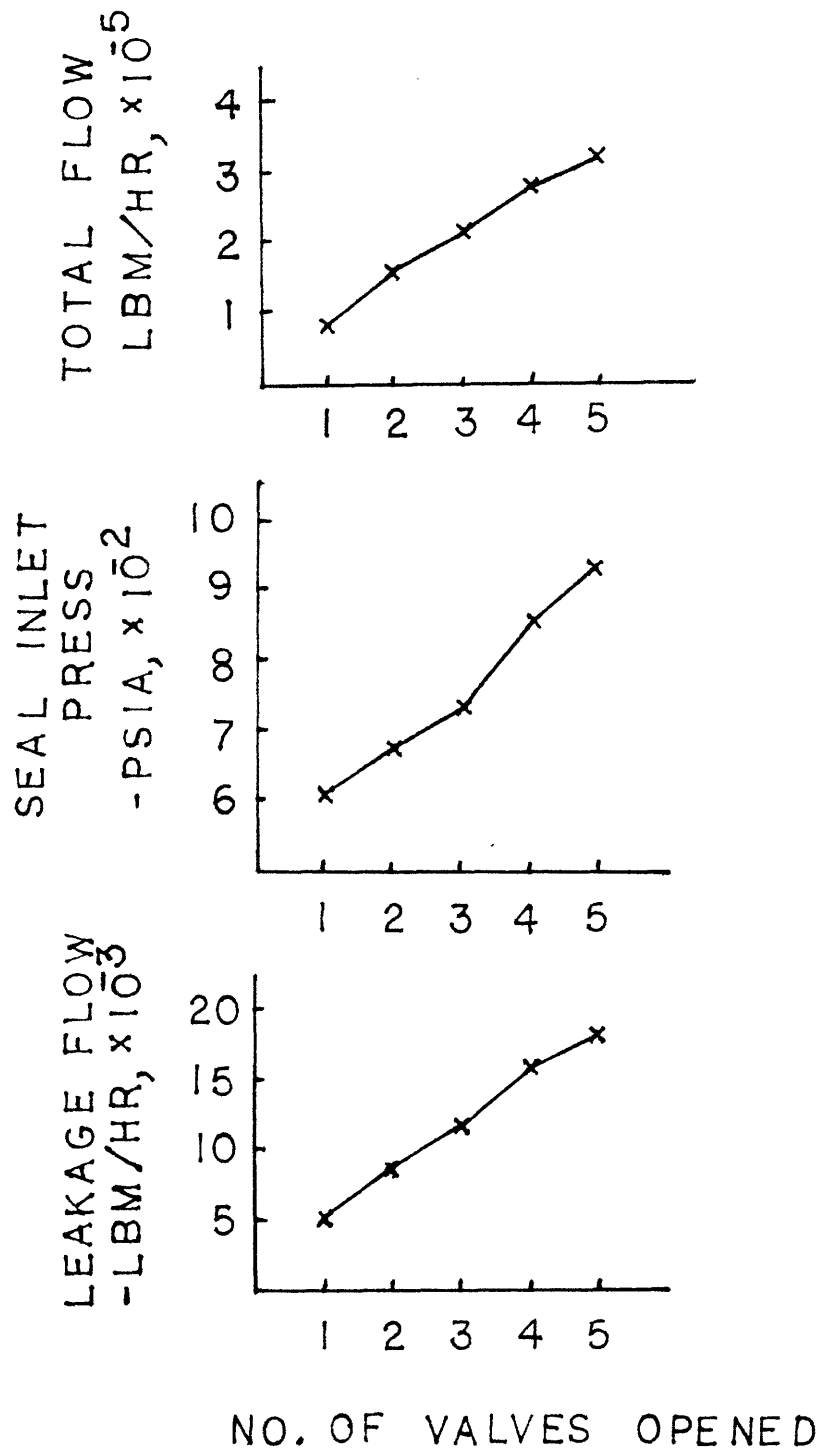
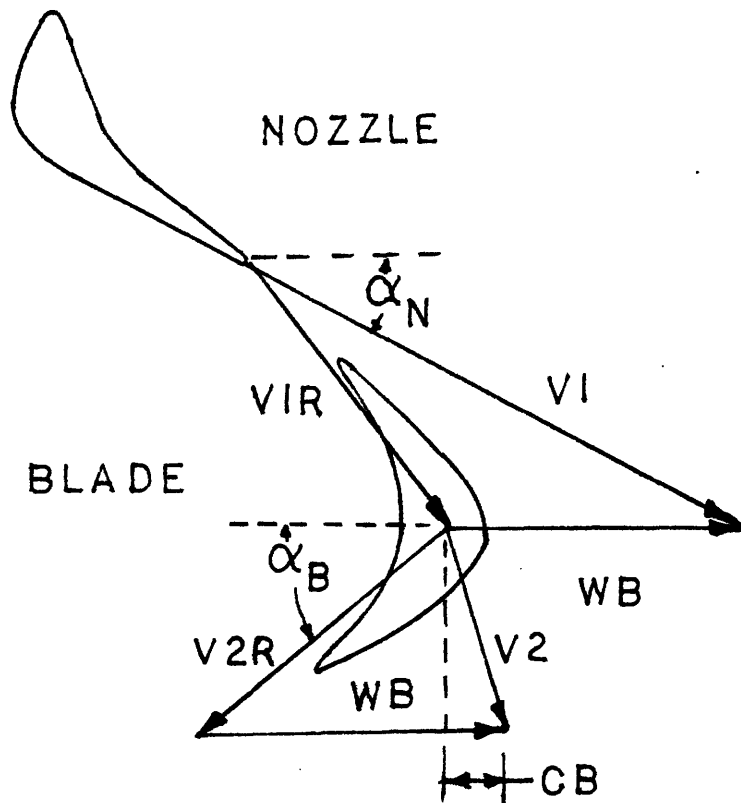


FIGURE 29 Steam flow and first stage shell pressure for compressor drive turbine.



- α_N - Nozzle Exit Angle
- α_B - Blade Exit Angle
- V_1 - Absolute Velocity Leaving Nozzle
- V_{1R} - Steam Velocity Relative to Blade
- WB - Blade Tangential Velocity
- V_{2R} - Relative Steam Velocity Leaving Blade
- V_2 - Absolute Steam Velocity Leaving Blade
- CB - Swirl Velocity of Steam Leaving Blade

FIGURE 30 Schematic diagram of steam velocities entering and leaving turbine blade.

Part of this flow is leaked through the seal between first and second stages. If the leakage flow followed purely potential principles, then at the seal entrance the preswirl velocity would be

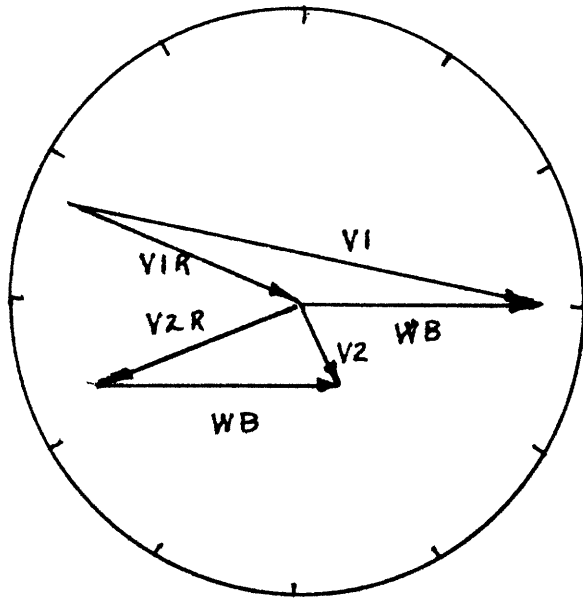
$$c_1 = CB \cdot \frac{r_{\text{Blade}}}{R} \quad (91)$$

The preswirl would increase by the ratio of the radii and would be in the same direction induced from the upstream blades.

If frictional effects are included then a more accurate preswirl value for the seal is obtained. The technique to arrive at the preswirl value is to divide the space between the stationary and rotating surfaces into increments. (See Figure 33.) The principle of conservation of angular momentum is applied to each increment. The resulting equation predicts the tangential velocity at the adjacent station and can be written as

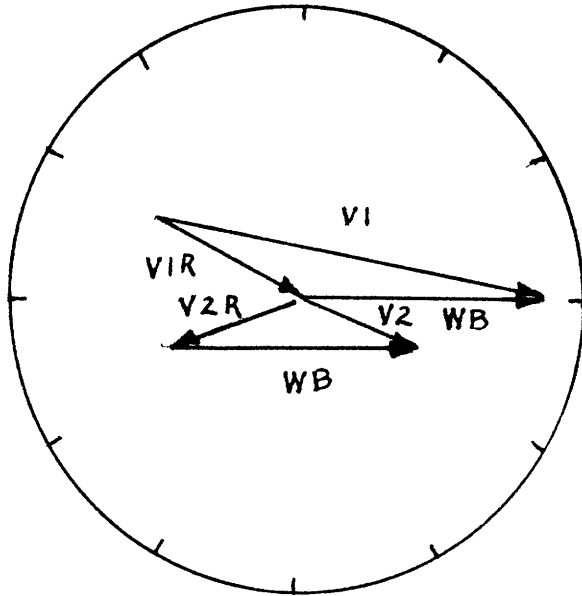
$$c_{i-1} r_i - c_i r_{i+1} - \frac{2\pi}{Q} \rho r_i^2 \cdot \left[\frac{1}{2} \lambda_R (c_i - \Omega r_i)^2 S_{Ri} + \frac{1}{2} \lambda_S c_i^2 S_{Si} \right] \quad (92)$$

where S_{1i} and S_{2i} are the wetted perimeters of the rotating and stationary surfaces. The friction factor, λ , can be calculated using equations from Section 2. Equation (92) predicts nearly potential flow for high leakage flow rates. For



3rd Valve

V1	= 1806 ft/sec
V1R	= 917
V2	= 349
V2R	= 845
WB	= 931
CB	= 137



5th Valve

V1	= 1488 ft/sec
V1R	= 606
V2	= 463
V2R	= 559
WB	= 931
CB	= 403

FIGURE 31 Velocity diagrams of steam flow for 3rd and 5th valve points.

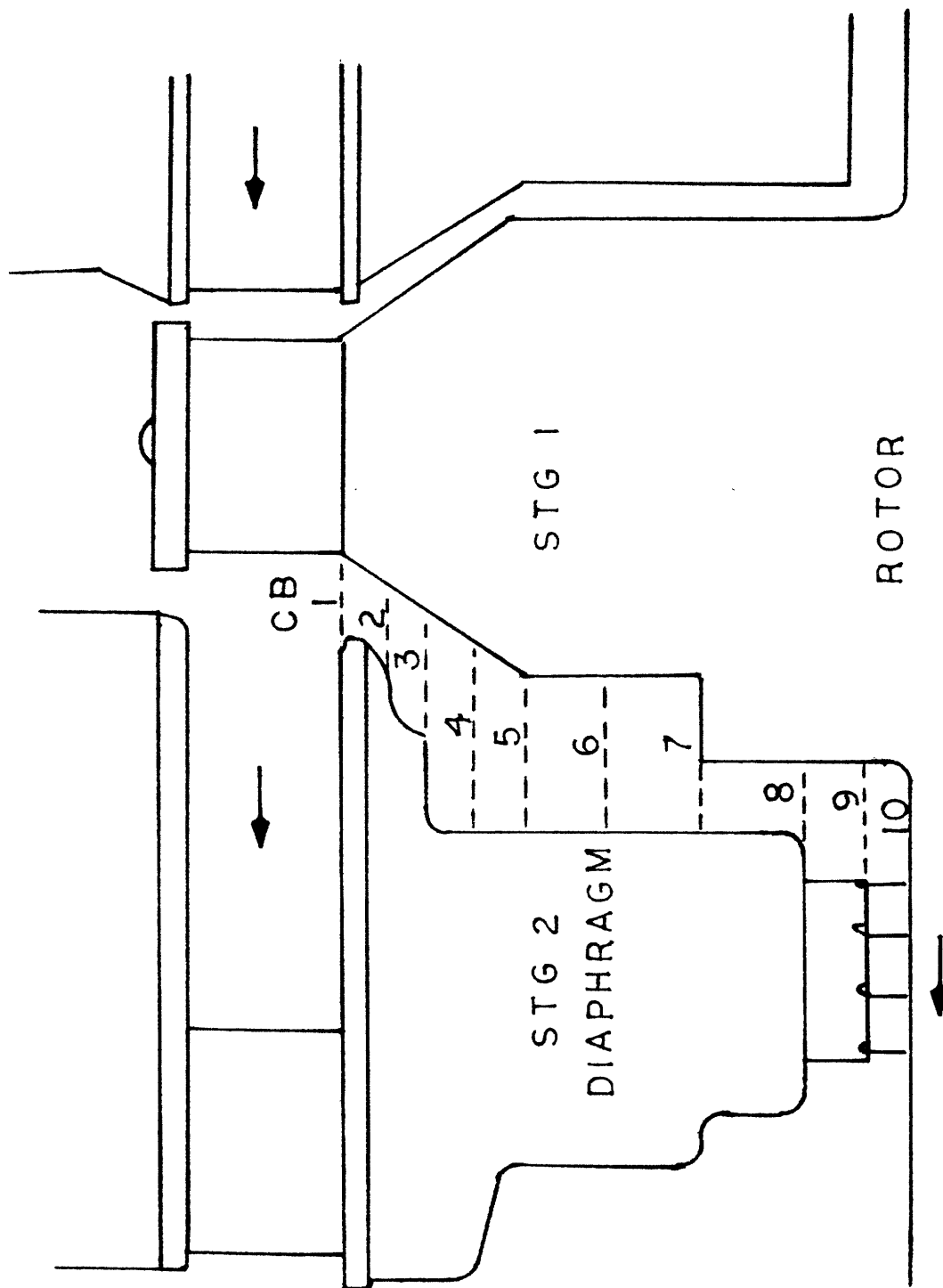


FIGURE 32 Modeling of leakage flow path for determination of seal preswirl value.

very low leakage rates, the frictional forces dominate and the preswirl velocity nearly one-half the rotor surface velocity. The distributions of tangential velocities are shown in Table 9 as each valve is opened. Also shown are the preswirl values as predicted by potential flow principles. The values at the last station are the preswirl velocities of the seal and are very much different from either of the two simpler approaches.

The more accurate preswirl values are used to predict the out-of-phase force generated by the seal. The destabilizing force gradient is shown in Figure 33 for each valve point. Also plotted are the destabilizing force gradients for a preswirl value equal to one-half the surface velocity. The force gradients differ by more than 2 to 1 for the 4th and 5th valve points. This clearly demonstrates the significance of including blade induced swirl and steam path geometry when establishing the preswirl values for a seal force analysis.

4.2 Stability Contour Mapping

The stiffness and damping characteristics of a labyrinth seal must be applied to a specific rotor system to determine the actual impact on stability. Labyrinth seals are not always destabilizing. In Section 3, it was shown that depending on the design of the seal, the conditions at which it operates and the proximity of the system's natural frequency, the force in the seal can increase the stability of the rotor system. The

TABLE 9

TANGENTIAL VELOCITY DISTRIBUTIONS
FOR DIFFERENT VALVE POINTS

Station No.	Tangential Velocities - ft/sec				
	1st Valve	2nd Valve	3rd Valve	4th Valve	5th Valve
1	-52	93	142	300	416
2	108	176	206	333	431
3	211	236	255	358	433
4	277	281	291	377	451
5	320	313	319	392	458
6	348	337	340	404	463
7	375	365	367	427	482
8	381	375	378	432	484
9	384	383	386	437	485
10	385	388	393	442	488
Total Leakage lb/hr	4893	8724	11262	15545	18086
1/2 Surface Velocity - 308 ft/sec					
Preswirl Velocity by Eq (104) (Potential Flow)	-74	132	201	425	589

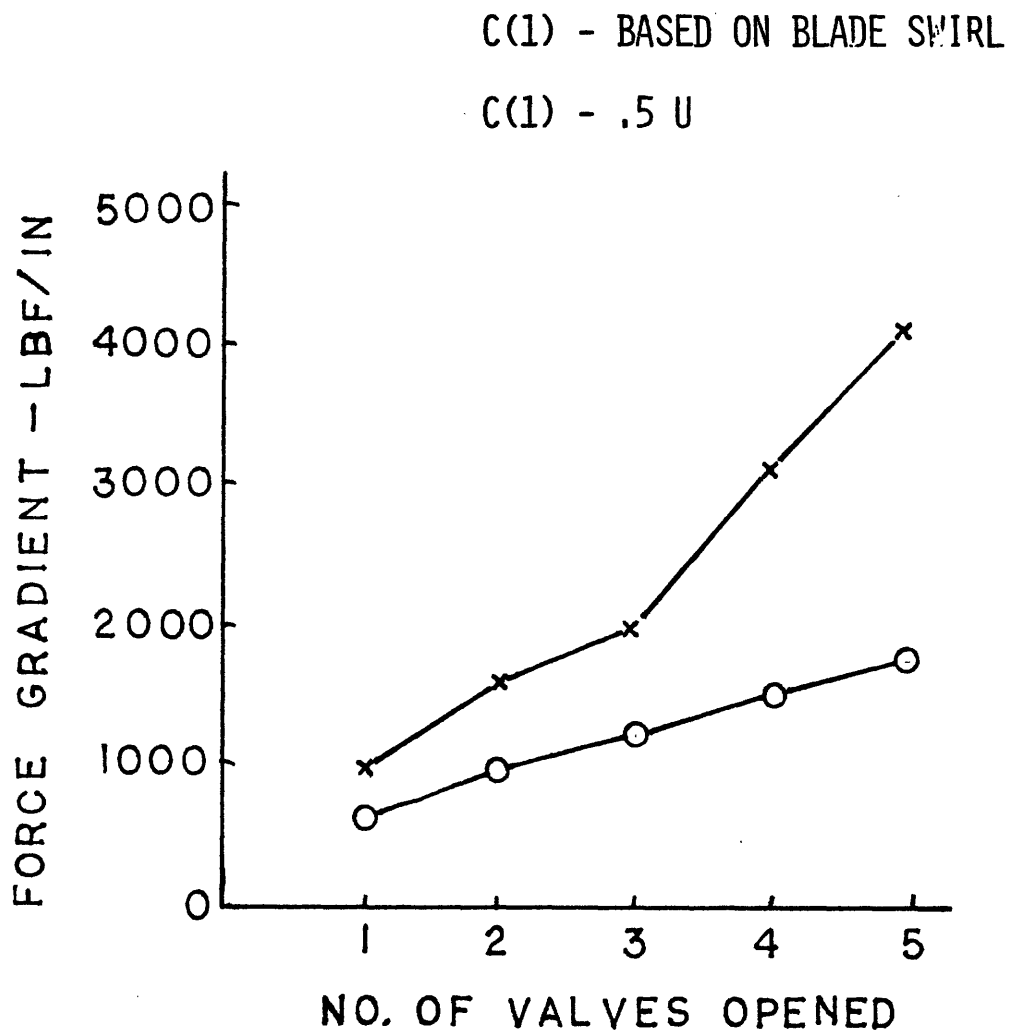


FIGURE 33 Comparison of destabilizing force gradient for stage (2) seal. Preswirls from equation (92) and one-half rotor surface velocity.

magnitude of the out-of-phase force is influenced by the state of pressure in the seal. The previous example demonstrated that as machine output increased, so did internal pressures. In general, the destabilizing force from the seals will also increase. The designer must be concerned with both speed and load in a stability evaluation.

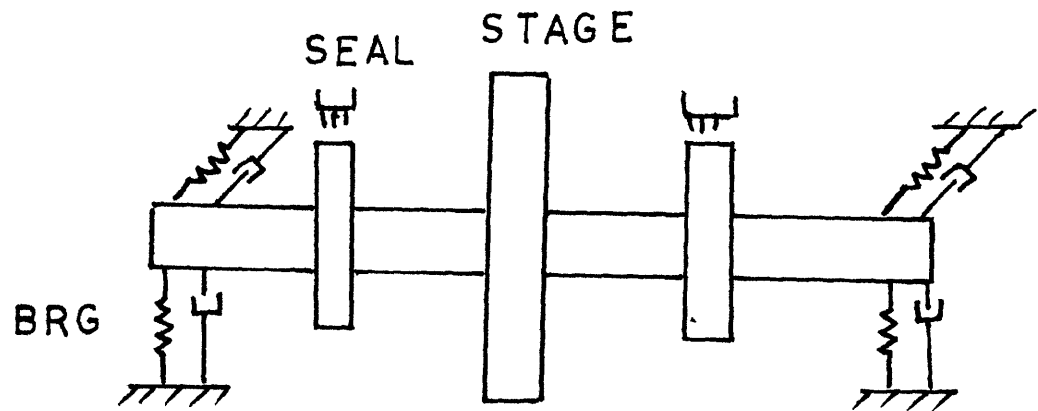
In addition to the system's stability, the efficiency of the machine, in some cases, may be just as important. Concerns over leakage rate can take the form of either minimizing the loss of energy associated with leakage or preventing the leakage rate from getting larger than what a leakage control system can handle. Many times the gas being compressed is toxic and must be contained. If during the operation of a machine, load related instabilities arise from labyrinth seals, then design changes must also consider the effect on overall efficiency and flow limitations on existing leakage control systems.

To demonstrate how the various operational aspects mentioned can be reconciled to achieve satisfactory operation, the following case will be analyzed. A variable speed steam turbine with cylindrical journal bearings is shown in Figure 34. This simple model which consists of a 60" long shaft with a diameter of 5" has three point masses. The middle one represents the turbine stages and the outer two are areas of increased diameter where the labyrinth seals are applied. The cylindrical journal bearings are loaded to 350 PSI based on projected bear-

ing area. This level is required to suppress oil whip. The bearing support is assumed to be rigid in both horizontal and vertical directions. For this configuration, the rotor system has damped natural frequencies shown in Figure 35. Of the modes shown, the fundamental vertical mode is the least stable. As shown in Figure 36 this mode will theoretically go unstable at 9000 RPM based on journal bearing properties at no load. The stiffness and damping coefficients shown in Figure 37 are obtained from a linearized analysis. At 9000 RPM the amplitude of the vertical mode does not become infinitely large but reaches a finite value due to nonlinear effects of the oil film. Generally, some asynchronous vibration can be tolerated with no harm to the machinery. Much above 9000 RPM, considerable subsynchronous vibration exists. The machine would run rough and possibly damage the bearings and seals from excessive vibration.

Load on the machine is now simulated by prescribing pressure levels on each side to the two seals. The geometry of the seals is given in Figure 16 for the 31 tooth case. The radial clearance is a uniform .020 inches. One side of each seal will be maintained at 290 PSIA. The other side increases with load up to 2500 PSIA. The operating speed range is from 5000 to 9000 RPM. The procedure will be to calculate the stiffness and damping coefficients of the seals at each speed and pressure point and combine them with the rotor-bearing system. The logarithmic decrement for the fundamental mode will be calculated

EXAMPLE



Rotor

Span 60"
Dia 5"
Wgt 1500#

Brg

Plain Cyl
D - 2"
L - 1"
Clearance Ratio - .002
Loading - 350 PSI

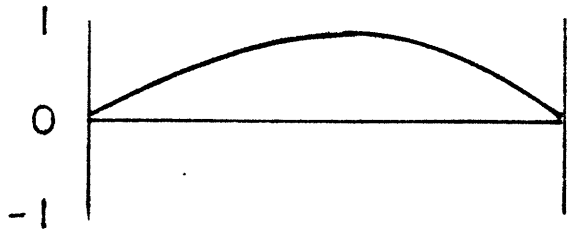
Seals

31 Teeth
Straight
Pin 500 to 2500 PSIA
Pex 290 PSIA

FIGURE 34 Single stage rotor model with two labyrinth seals.

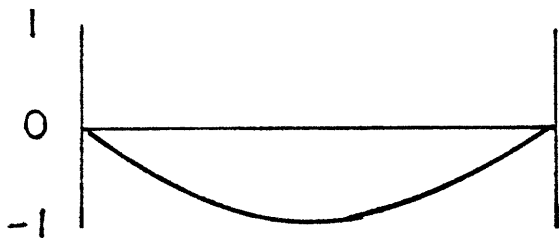
Planar Mode Shape

Damped Critical Speed



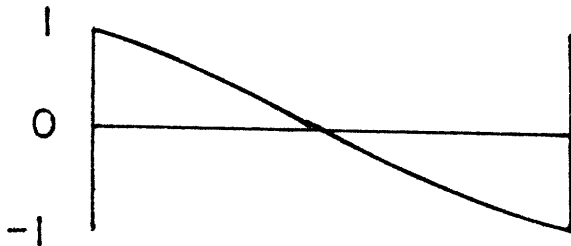
Horizontal

2389 RPM



Vertical

2647 RPM



Horizontal

5253 RPM

FIGURE 35 Damped critical speeds and mode shapes below 12,000 RPM for Figure 34. Rotor speed 9000 RPM.

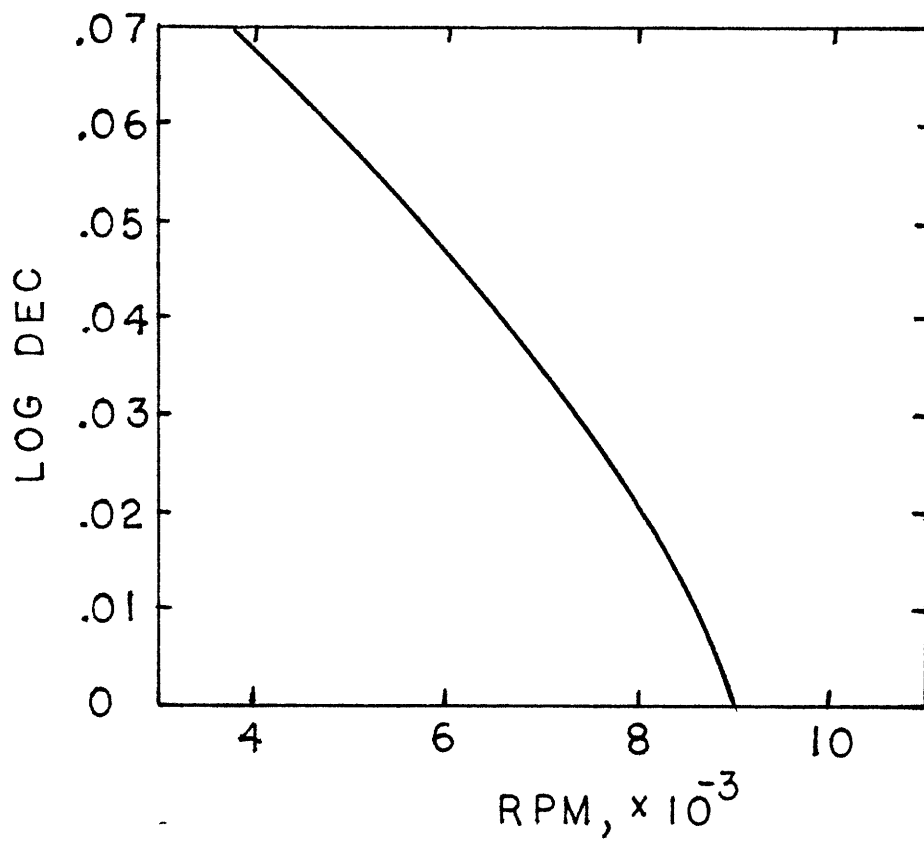


FIGURE 36 Log decrement for single stage rotors model without seal forces.

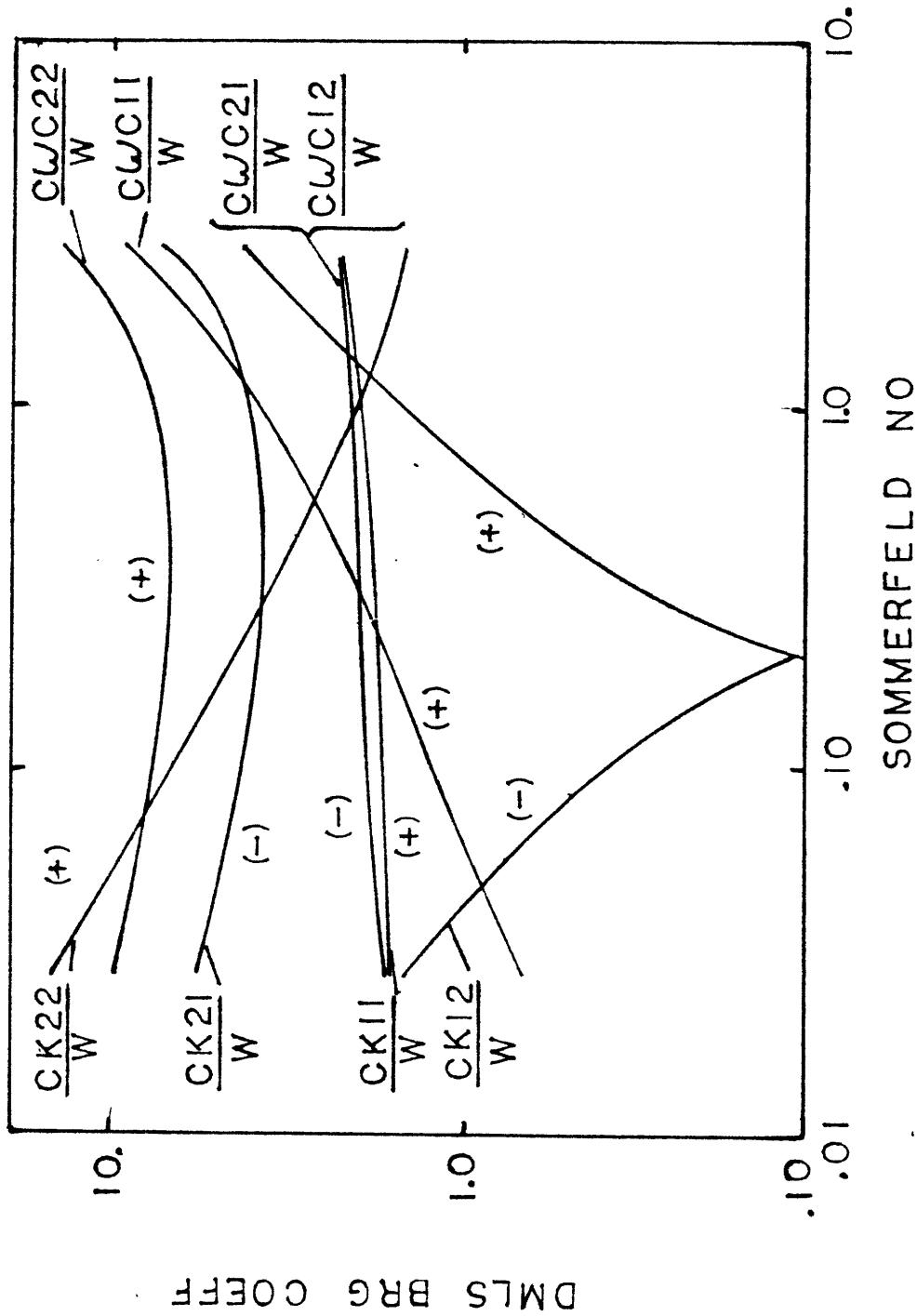


FIGURE 37 Dimensionless bearing coefficients versus Sommerfeld number for plain cylindrical bearing.

at each point using Lund's⁽¹⁶⁾ transfer matrix technique. Within the range of operating speeds and seal pressures a sufficient number of points are calculated to establish a stability surface. For the model described, the values are given in Table 10 and plotted in Figure 38.

There are several aspects of the stability contour that should be noted. First is that for modest increases in seal pressure the speed at which instability occurs is increased. For this example a maximum of 12,000 RPM can be reached with a seal inlet pressure of 500 PSIA. As the inlet pressure is increased, the speed where instability occurs decreases. The increase in the instability threshold speed at low pressure is due to the asymmetric journal bearing properties. This effect from asymmetry is more thoroughly discussed by Smith⁽¹⁹⁾. At 5000 RPM and below, increases in seal pressure increases the stability of the system. This cross-over point can be determined by taking the ratio of K_{12}/C_{11} of seal coefficients. When the value is less than the natural frequency of the first critical, the seal tends to destabilize the system. For this case the speed at which the ratio equals the first critical speed is 4800 RPM.

Once the region of stable operation has been defined by the contour map, an evaluation can be made as to how the turbine can be operated. It is a simple matter to access which speeds and pressures are safe from instability. The design engineer

TABLE 10

FIRST CRITICAL LOG DECREMENTS
FOR ROTOR WITH ORIGINAL AND DEEP CHAMBER SEALS

Speed Press. /	<u>Original Seal</u>				
	5000	7000	9000	11000	13000
0	.059 2674	.037 2362	.0001 2389	-.005 2410	-.041 2431
500	.089 2658	.105 2632	.096 2422	.056 2487	-.161 2510
1000	.111 2643	.128 2599	.007 2514	-.155 2512	-.305 2524
1500	.128 2626	.108 2556	-.109 2519	-.260 2519	-.417 2535
2000	.139 2607	.030 2534	-.182 2522	-.342 2625	-.521 2549
	<u>Deep Seal</u>				
	5000	7000	9000	11000	13000
0	.059 2674	.037 2362	.0001 2389	-.005 2410	-.041 2431
500	.074 2664	.083 2363	.061 2399	.072 2420	-.041 2494
1000	.0855 2655	.099 2627	.113 2585	.031 2515	-.253 2522
1500	.096 2645	.107 2587	.070 2537	-.101 2516	-.324 2528
2000	.105 2635	.106 2587	-.029 2525	-.175 2519	-.386 2534

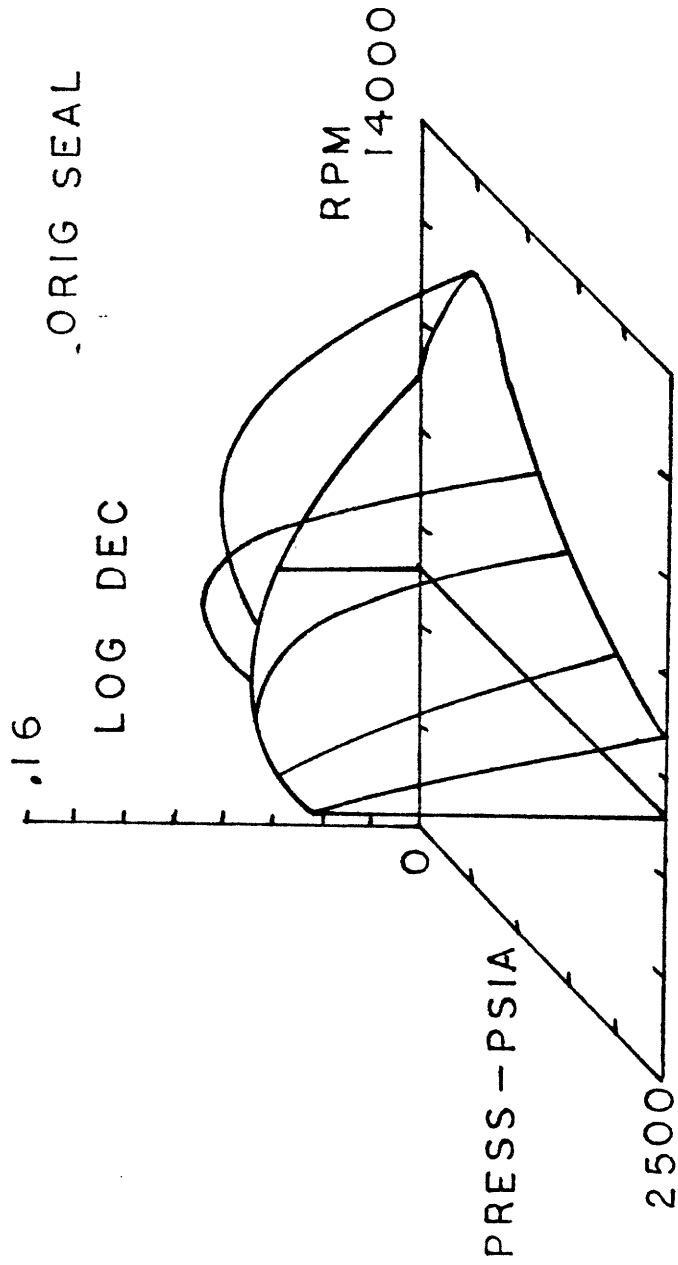


FIGURE 38 Stability contour map for single stage rotor with original seal design.

has a feel for how sensitive the machine will be to changes in speed and internal pressure or load. In the steep portions of the contour, small changes in speed or pressure can make dramatic changes in the level of subsynchronous vibration experienced. Prudent design practice and operation would be to avoid such areas.

From the base contour, parameters can be varied to determine the effect on rotor stability. The design engineer can effectively compromise between various aspects to reach an acceptable design. To demonstrate how the stability contour can be reshaped, consider the following example. It is desired to operate the turbine just analyzed at 9000 RPM and at a load which corresponds to a seal inlet pressure of 1700 PSIA. Presently, the turbine is limited to 1200 PSIA at that speed. (See Figure 38.) At the higher pressure there is also a concern of overloading an existing leakage control system. The operation would also like to decrease leakage by installing reduce clearance seals.

For this example, both goals are achievable by relatively minor changes to the seal design. Extension of the stable region from its present position can be accomplished by reducing the force generated by the seal. One of the stronger parameters influencing the seal forces is the average chamber height. From equation (85) by doubling the tooth height, the destabilizing force is reduced by a factor of four. Also from

this equation it was shown that the force in long seals is not significantly affected by changes in seal clearances. Two changes are made to the design of the seal. First, the average chamber height will be increased by 50 percent from .236 to .334 inches. Also, the radial clearance will be reduced from .020 to .010 inches. The resulting stability contour is shown in Figure 39. At 9000 RPM the turbine can now operate up to a pressure of 1750 PSIA before starting to become unstable. A comparison of the leakage flow rates for both designs is shown in Figure 40. The total leakage rate is 30% lower at 1750 PSIA than it was at 1200 PSIA. A similar procedure would be followed to investigate stability contour reshaping from varying other parameters. For this case all the goals were achieved; however, this may not always be the case when the effects of partial arc forces and blade induced swirl are considered.

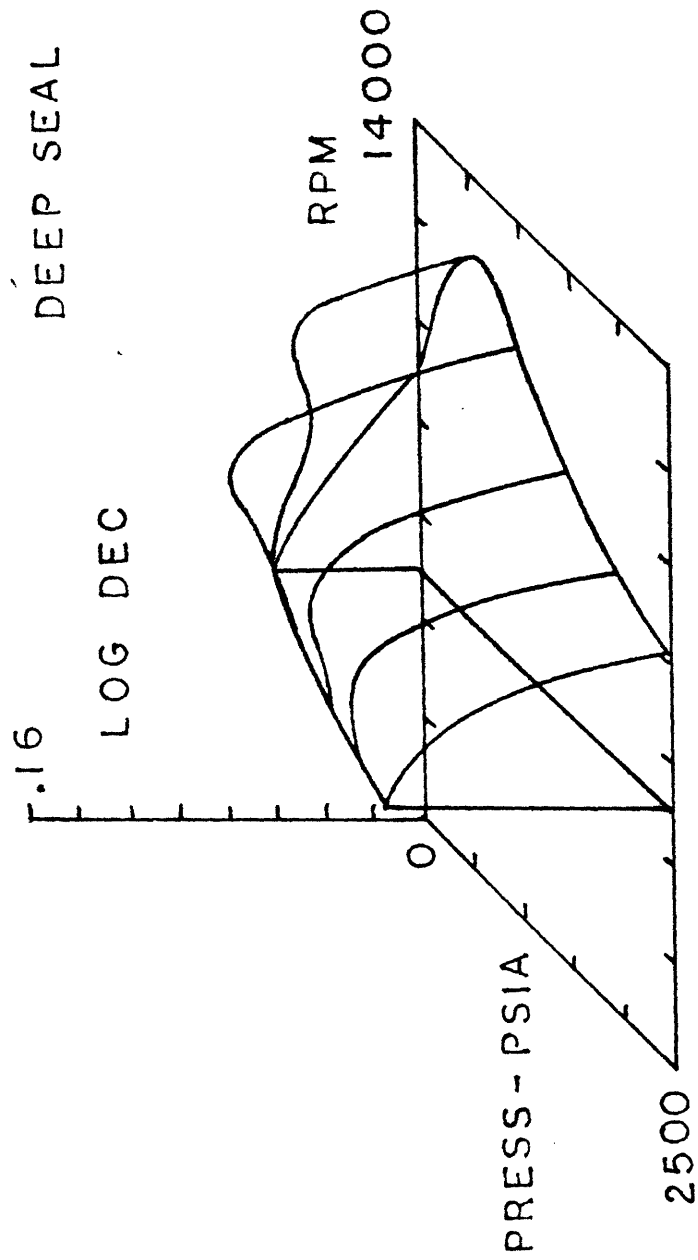


FIGURE 39 Stability contour map for single stage rotor with deep chamber, reduced clearance design.

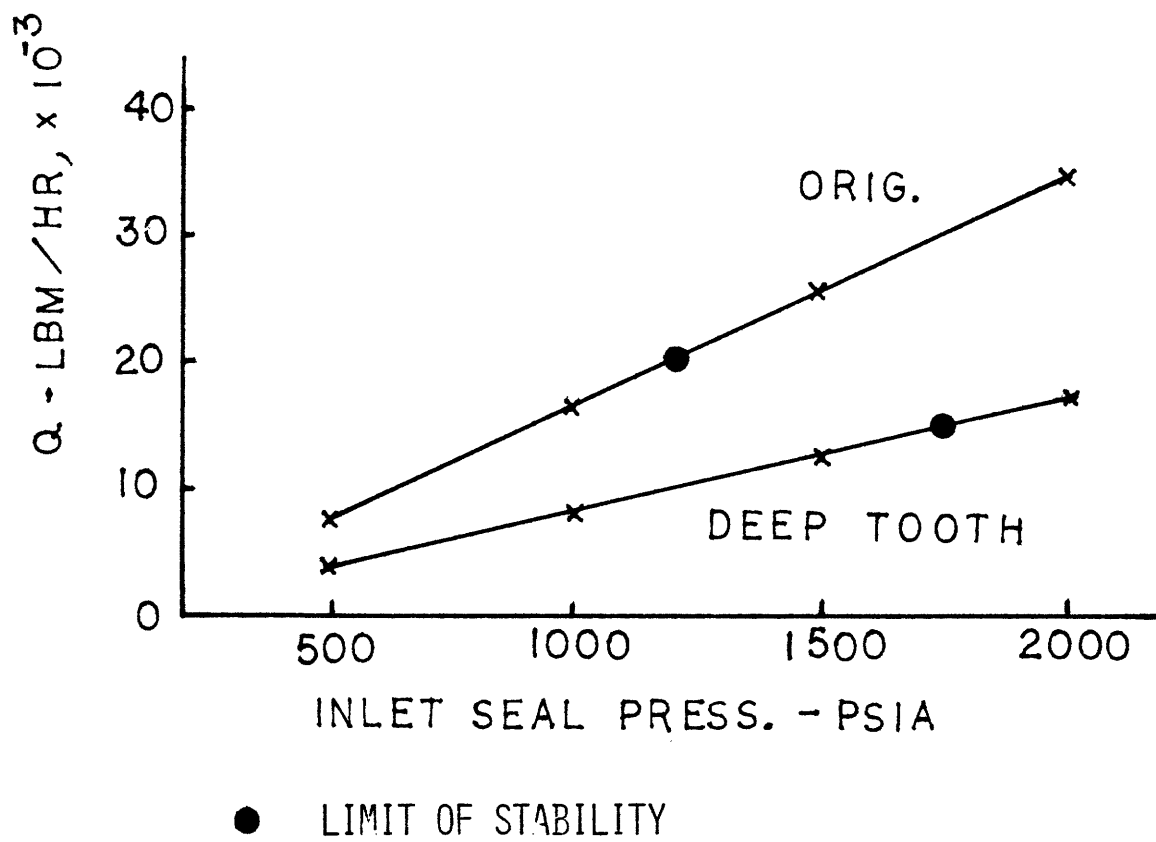


FIGURE 40 Comparison of leakage flow rates for original and reduced clearance seal designs.

V. CONCLUSIONS

1. The amplitude and phase of the pressure variation in each chamber of a labyrinth seal are determined for a rotor shaft orbiting in a parallel fashion. The distributions are based on a one-dimensional analysis for arbitrary seal geometry and are used to predict stiffness and damping coefficients for stability analysis.
2. The stiffness and damping coefficients predict both stabilizing and destabilizing forces for constant clearance labyrinth seals. The magnitude and the direction of the out-of-phase force change as rotor speed, rotor natural frequency and leakage flow preswirl are changed.
3. Converging clearance and diverging clearance seals can be either stabilizing or destabilizing. As the clearance is made more converging, the out-of-phase force tends to increase in the direction of forward whirl. Increasing the divergence of a seal's clearance tends to increase the out-of-phase force in the negative whirl direction.
4. Excellent agreement is obtained when the cross-coupling stiffnesses measured by Benckert and Wachter are compared to predicted values. This comparison includes both straight and full labyrinth seals. More error exists between the calculated and

measured direct stiffness. The differences can be resolved by accounting for flow coefficient differences in the seal strips.

5. The fluid preswirl has a significant effect on the magnitude and direction of the out-of-phase seal force. A procedure is developed to calculate the preswirl velocity entering the seal for turbines. The method estimates the preswirl induced by turbine blades and predicts how the leakage tangential velocity changes in moving towards the seal from friction and gas path geometry. Substantial errors can result if the preswirl is assumed to be one-half the rotor surface velocity.
6. The influence of labyrinth seals can most accurately be judged when combined with an actual rotor system. Plotting the log decrement of the least stable mode as a function of load and speed graphically displays unstable areas of operation. For each speed and load combination, the effects of changes in bearing characteristics, blade efficiency and internal temperature and pressure must be accounted for. The stability contour maps can be used to evaluate changes in seal geometry with respect to stability and improve the stable range of operation in marginally stable machines.
7. Asymmetrical rotor support systems can have increased stability for seal forces that would be destabilizing in symmetrical rotor systems. As the magnitude of the seal force is increased the asymmetrical rotor system will become less stable.

VI. REFERENCES

1. H.M. Martin, "Steam Leakage in Dummies of the Ljungstrom Type", Engineering, Jan. 3, 1919.
2. G. Vermes, "A Fluid Mechanics Approach to the Labyrinth Seal Leakage Problem", Journal of Engineering for Power, April 1961.
3. C.A. Meyer and J.A. Lowrie, "The Leakage Thru Straight and Start Labyrinths and Honeycomb Seals", Journal of Engineering for Power, Oct. 1975.
4. J.S. Alford, "Protection Turbomachinery from Self-Excited Rotor Whirl", Journal of Engineering for Power, Oct. 1963.
5. F. Ehrich, "Aeroelastic Instability in Labyrinth Seals", Journal of Engineering for Power, Oct. 1968.
6. B.T. Murphy and J.M. Vance, "Labyrinth Seal Effects on Rotor Whirl Instability", Proceedings, Institution of Mechanical Engineers, 1980.
7. A.G. Kostyuk, "A Theoretical Analysis of the Aerodynamic Forces in Labyrinth Glands of Turbomachines", Teploenergetika, 1972.
8. T. Iwatsubo, "Evaluation of Instability Forces of Labyrinth Seals in Turbines or Compressors", Rotordynamic Instability Problems in High-Performance Turbomachinery NASA C.P. 2133, 1980.
9. S.H. Crandall, "Physical Explanations of the Destabilizing Effect of Damping in Rotating Parts", Rotordynamic Instability Problems in High Performance Turbomachinery NASA C.P. 2133, 1980.
10. S.H. Crandall, "A Heuristic Explanation of Journal Bearing Instability", Massachusetts Institute of Technology, Cambridge, MA, Unpublished.
11. H. Benckert and J. Wachter, "Flow Induced Spring Constants of Labyrinth Seals", Proceedings, Institution of Mechanical Engineers, 1980.
12. H. Benckert and J. Wachter, "Flow Induced Spring Coefficients of Labyrinth Seals for Application in Rotor Dynamics", Rotordynamic Instability Problems in High-Performance Turbomachinery, NASA C.P. 2133, 1980.
13. R. Jenny, "Labyrinth as a Cause of Self-Excited Rotor Oscillations in Centrifugal Compressors", Sulzer Technical Review 4, 1980.
14. M. Kurohashi, Y. Inoue, T. Abe, and T. Fujikawa, "Spring and Damping Coefficients of Labyrinth Seals", Proceedings, Institution of Mechanical Engineers, 1980.
15. H. Schlichting, "Boundary Layer Theory", 6th Edition, McGraw-Hill Book Co., NY, 1968.

16. J.W. Lund, "Stability and Damped Critical Speeds of a Flexible Rotor in Fluid-Film Bearings", Journal of Engineering for Industry, Trans. ASME Paper No. 73-DET-103.
17. R.G. Deissler, Trans. ASME, 77:7 (Nov. 1955).
18. S. Kline and A.H. Shapiro, Nat. Advisory Comm., Aeronaut. Tech Note 3048, 1953.
19. D.M. Smith, "The Motion of a Rotor Carried by a Flexible Shaft in Flexible Bearings", Proc. Roy. Soc. (London) A 142, 1933.
20. J.H. Spurk and R. Keiper, "Selbsterregte Schwingungen bei Turbomachinen Infolge der Labyrinth-Stromung", Ingenieur-Archiv, 1974.
21. D.V. Wright, "Air Model Tests of Labyrinth Seal Forces on a Whirling Rotor", Journal of Engineering for Power, Oct. 1978.
22. S. Whitaker, "Introduction to Fluid Mechanics", Prentice-Hall, Inc., Englewood Cliffs, NJ 1968.
23. W. Rohsenow and H. Choi, "Heat, Mass and Momentum Transfer", Prentice-Hall, Inc., Englewood Cliffs, NJ 1961.
24. J.P. DenHartog, "Mechanical Vibrations", 4th Edition, McGraw-Hill Book Co., NY 1956.

VII. APPENDIX

Determination of Chamber Pressure Variation

Two different methods can be used to determine the pressure variation in equation (46) and (49) for either direction of whirl. The first method involves solving for the magnitude and phase of the pressure and velocity perturbations simultaneously in all chambers of the seal. This can be done by noting that equations (46) and (49) must be true for all time and spatial positions.

For convenience, equation (46) and (49) can be written as

$$\begin{aligned}
 & D1 \frac{P_{mi-1}}{P_{i-1}} \cos \phi_{P_{l-1}} + D2 \frac{P_{mi}}{P_i} \sin \phi_{P_i} \\
 & + D3 \frac{P_{mi}}{P_i} \cos \phi_{P_i} + D4 \frac{P_{mi+1}}{P_{i+1}} \cos \phi_{P_{i+1}} \\
 & + D5 \frac{C_{mi}}{u} \sin \phi_{C_i} = \\
 & E1 \sin \frac{x}{R} - \omega t + E2 \cos \frac{x}{R} - \omega t \qquad (A.1)
 \end{aligned}$$

and

$$D6 \frac{P_{mi-1}}{P_{i-1}} \cos \phi_{P_{l-1}} + D7 \frac{P_{mi}}{P_i} \sin \phi_{P_i}$$

$$\begin{aligned}
& + D8 \frac{P_{mi}}{P_i} \cos \phi_{P_i} + D9 \frac{P_{mi}}{P_{i+1}} \cos \phi_{P_{i+1}} \\
& + D10 \frac{C_{mi}}{u} \sin \phi_{C_i} + D11 \frac{C_{mi+1}}{u} \cos \phi_{C_i} \\
& + D12 \frac{C_{mi-1}}{u} \cos \phi_{C_{i-1}} =
\end{aligned}$$

$$E3 \sin \frac{x}{R} = \omega t + E4 \cos \frac{x}{R} - \omega t \quad (A.2)$$

Each set of values for D1 to D12 and E1 to E4 are dependent on the steady state conditions and geometry for each chamber. By letting ωt equal 0 and $-\pi/2$, four linearly independent equations result for each chamber. These describe the magnitude and phase of both pressure and velocity variations. For this equilibrium problem the following boundary conditions are imposed:

1. Uniform pressure and tangential velocity entering the seal.
2. The pressure at the exit of the seal is circularly uniform.

Sufficient information now exists to solve the $4(N-1)$ set of equations for a seal with N seal strips. The general form of the simultaneous equations can be written as

$$\left[\begin{array}{c} \bar{D} \end{array} \right] \left[\begin{array}{c} P_{mi} \sin \phi \\ \vdots \\ C_{mi} \cos \phi \end{array} \right] = \left[\begin{array}{c} \bar{E} \end{array} \right] \quad (A.3)$$

To demonstrate how both D and E matrices are constructed, a specific example is shown in Figure A.1 for a four tooth seal. For this example a 12 x 12 matrix results. The values for magnitude and phase are found by standard matrix operation.

The above method is an acceptable approach when the number of chambers is small. The size of the D matrix grows rapidly as more teeth are added. For certain applications, the total number of sealing strips may be as many as 50. The size of the matrix now prohibits use of the above method. Large, high speed computers are practically limited to solving seals with at most 25 teeth with this method before becoming cost prohibitive.

An alternate approach can be found by examining the mass and momentum equations. By starting in the first chamber and assuming values for $P_{m2} \sin \phi$ and $P_{m2} \cos \phi$, four equations can be written to evaluate $P_{m3} \sin \phi$, $P_{m3} \cos \phi$, $c_{m2} \sin \phi$ and $c_{m2} \cos \phi$. The procedure now continues to each succeeding chamber. The four equations take the general form

$$\begin{aligned}
 P_{mi+1} \sin \phi_{P_{i+1}} &= f_1 \left(P_{mi}, \phi_{P_i}, P_{mi-1}, \phi_{P_{i-1}}, c_{mi-1}, \phi_{c_{i-1}} \right) \\
 P_{mi+1} \cos \phi_{P_{i+1}} &= f_2 \left(P_{mi}, \phi_{P_i}, P_{mi-1}, \phi_{P_{i-1}}, c_{mi-1}, \phi_{c_{i-1}} \right) \\
 c_{mi+1} \sin \phi_{c_{i+1}} &= f_3 \left(P_{mi}, \phi_{P_i}, P_{mi-1}, \phi_{P_{i-1}}, c_{mi-1}, \phi_{c_{i-1}} \right) \\
 c_{mi+1} \cos \phi_{c_{i+1}} &= f_3 \left(P_{mi}, \phi_{P_i}, P_{mi-1}, \phi_{P_{i-1}}, c_{mi-1}, \phi_{c_{i-1}} \right) \quad (A.4)
 \end{aligned}$$

If the proper values for pressure amplitude and phase were initially chosen, then after the last seal strip the values for $P_{mn+1} \sin\phi$ and $P_{mn+1} \cos\phi$ are both zero. This satisfies the end boundary condition. The exit boundary condition can be stated as

$$P_{m_{n+1}} \sin\phi_{P_{n+1}} = F(\psi_1, \psi_2) = 0 \quad (\text{A.5})$$

$$P_{m_{n+1}} \cos\phi_{P_{n+1}} = G(\psi_1, \psi_2) = 0 \quad (\text{A.6})$$

where

$$\psi_1 = P_{m_2} \sin\phi_{P_2}$$

and

$$\psi_2 = P_{m_2} \cos\phi_{P_2}.$$

To find the proper initial values for the pressure variation, a trial and error technique is required. One iteration method that converges quickly is the Newton-Raphson technique. An initial guess is made for $(\psi_1)_0$ and $(\psi_2)_0$. Next, an attempt is made to find values for h and k such that

$$F[(\psi_1)_0 + h, (\psi_2)_0 + k] = 0 \quad (\text{A.7})$$

and

$$G[(\psi_1)_0 + h, (\psi_2)_0 + k] = 0. \quad (\text{A.8})$$

By expanding equations (A.7) and (A.8) in a Taylor series about the initial guess and retaining the linear terms, the equations become

$$F_0 + h \frac{\partial F_0}{\partial \psi_1} + k \frac{\partial F_0}{\partial \psi_2} = 0 \quad (\text{A.9})$$

$$G_0 + h \frac{\partial G_0}{\partial \psi_1} + k \frac{\partial G_0}{\partial \psi_2} = 0 \quad (\text{A.10})$$

or

$$h = - \frac{\begin{vmatrix} F_0 & \frac{\partial F_0}{\partial \psi_2} \\ G_0 & \frac{\partial G_0}{\partial \psi_2} \end{vmatrix}}{\begin{vmatrix} \frac{\partial (F, G)_0}{\partial (\psi_1, \psi_2)} \end{vmatrix}} \quad (\text{A.11})$$

and

$$k = - \frac{\begin{vmatrix} \frac{\partial F_0}{\partial \psi_1} & F_0 \\ \frac{\partial G_0}{\partial \psi_1} & G_0 \end{vmatrix}}{\begin{vmatrix} \frac{\partial (F, G)_0}{\partial (\psi_1, \psi_2)} \end{vmatrix}} \quad (\text{A.12})$$

To determine the partial derivatives of F and G, an approximation is made by separately changing $(\psi_1)_0$ and $(\psi_2)_0$ a small amount. That is

$$\frac{\partial F}{\partial \psi_1} = \frac{F(\psi_1 + \epsilon_1, \psi_2) - F(\psi_1, \psi_2)}{\epsilon_1} \quad (\text{A.13})$$

where ϵ_1 is a small increment compared to ψ_1 . The other three partial derivatives are evaluated in a similar fashion. Once a set of values has been either assumed or calculated for Pm_2

$\sin\phi_{p2}$ and $Pm_2 \cos\phi_{p2}$, three calculations are required to establish F_0 and G_0 and the partial derivative approximations before a new set of $Pm_2 \sin\phi_{p2}$ and $Pm_2 \cos\phi_{p2}$ are determined. The iteration procedure continues until the exit boundary conditions are satisfied. The total number of calculations is greatly reduced from the previous method for seals with many teeth.